

**DEVELOPMENT AND CHARACTERIZATION OF LASER-  
ACTIVATED PERFLUOROCARBON NANODROPLETS AS  
THERANOSTIC AGENTS**

A Dissertation  
Presented to  
The Academic Faculty

by

Andrew Zhao

In Partial Fulfillment  
of the Requirements for the Degree  
Doctor of Philosophy in the  
Wallace H. Coulter Department of Biomedical Engineering

Georgia Institute of Technology & Emory University  
December 2023

**COPYRIGHT © 2023 BY ANDREW ZHAO**

**DEVELOPMENT AND CHARACTERIZATION OF LASER-  
ACTIVATED PERFLUOROCARBON NANODROPLETS AS  
THERANOSTIC AGENTS**

Approved by:

Dr. Stanislav Emelianov, Advisor  
School of Electrical Engineering and  
Computer Engineering, Wallace H. Coulter  
Department of Biomedical Engineering  
*Georgia Institute of Technology and Emory  
University School of Medicine*

Dr. Mark Prausnitz  
School of Chemical and Biomolecular  
Engineering  
*Georgia Institute of Technology*

Dr. Ravi Kane  
School of Chemical and Biomolecular  
Engineering  
*Georgia Institute of Technology*

Dr. Costas Arvanitis  
School of Mechanical Engineering,  
Wallace H. Coulter Department of  
Biomedical Engineering  
*Georgia Institute of Technology and  
Emory University School of Medicine*

Dr. John McDonald  
School of Biological Sciences  
*Georgia Institute of Technology*

Date Approved: Sept 19, 2023

*To my parents for their unconditional support and encouragement*

## ACKNOWLEDGEMENTS

I would like to thank a whole host of people who have been pivotal for the completion of this work. Starting from the top, my advisor Dr. Stanislav Emelianov for having so much patience and allowing me to be “the soldier and the general.” I would also like to thank the lab members both former and current: Ayoung Choe, Anamik Jhunjunwala, Andrei Karpiouk, Anthony Yu, Daniela Santiesteban, David Qin, Diego Dumani, Don VanderLaan, Eleanor Barber, Euisuk Chung, Heechul Yoon, Jeungyoon Lee, Jeehyun Lee, Jingfei Liu, Jinhwan Kim, Julian Rose, Kelsey Kubelick, Kristina Hallam, Melissa Cadena, Myeongsoo Kim, Rob Nikolai, Samuel Morais, Steve Yarmoska, Tim Sowers, Xing Long, Xinyue Huang, and Yiying Zhu. All these members have contributed in their own way to my development both as a scientist as well as a person. I would especially like to thank Kristina and Yiying for their help on getting me started with Aim 1. Without their support the project would have taken substantially longer to mature. Additionally, I would like to thank Jinhwan Kim for being instrumental in putting the ideas and directions for my project together. I will miss our random conversations about food and life in general. I would also like to acknowledge the substantial support from Euisuk Chung. It would almost be without exaggeration that without his contribution much of this dissertation would be incomplete.

I would also like to thank the friends that I met along the way during graduate school: Vic Pan, Chris Tung, Quoc Mac, Kim Le, and Ryan Akman. One final thank you to my family and friends for supporting me through this journey.

# TABLE OF CONTENTS

<b>ACKNOWLEDGEMENTS</b>	<b>iv</b>
<b>LIST OF TABLES</b>	<b>viii</b>
<b>LIST OF FIGURES</b>	<b>ix</b>
<b>LIST OF SYMBOLS AND ABBREVIATIONS</b>	<b>xvi</b>
<b>SUMMARY</b>	<b>xix</b>
<b>CHAPTER 1. Introduction</b>	<b>1</b>
<b>1.1 Ultrasound Imaging</b>	<b>1</b>
<b>1.2 Photoacoustic Imaging</b>	<b>2</b>
<b>1.3 Contrast Enhanced US</b>	<b>3</b>
1.3.1 Microbubbles	3
1.3.2 Perfluorocarbon Nanodroplets (PFCnDs)	4
<b>1.4 Thermodynamics of PFCnDs</b>	<b>5</b>
1.4.1 Laplace Pressure	5
1.4.2 Nucleation Theory	6
<b>1.5 ODV Nanodroplets and Their Applications</b>	<b>6</b>
<b>CHAPTER 2. Specific Aims</b>	<b>8</b>
<b>2.1 Aim 1: Enhance Understanding of Optical Droplet Vaporization (ODV)</b>	<b>8</b>
<b>2.2 Aim 2: Explore the Impact of ODV On Intracellular Delivery</b>	<b>8</b>
<b>2.3 Aim 3: Expand The Capabilities of PFCnDs For Drug Delivery</b>	<b>9</b>
<b>CHAPTER 3. Optical Vaporization Threshold and Longitudinal Performance Of Perfluorocarbon Nanodroplets</b>	<b>10</b>
<b>3.1 Introduction</b>	<b>10</b>
<b>3.2 Materials And Methods</b>	<b>12</b>
3.2.1 Nanodroplet Synthesis and Characterization	12
3.2.2 Cryo-Transmission Electron Microscopy Sample Preparation and Data Acquisition	15
3.2.3 Phantom Preparation and Imaging Setup	15
3.2.4 Data Processing	19
3.2.5 Surface Wave Elastography	20
3.2.6 Photobleaching of Epolight 3072	21
<b>3.3 Results and Discussion</b>	<b>21</b>
3.3.1 Preconditioning	21
3.3.2 PRF Variation	24
3.3.3 Shell Variation	26
3.3.4 Environmental Variation	31
3.3.5 Core Variation	35
<b>3.4 Conclusions</b>	<b>37</b>

<b>3.5</b>	<b>Acknowledgements</b>	<b>38</b>
<b>CHAPTER 4. Laser Induced Sonoporation Using PFCnDs</b>		<b>39</b>
<b>4.1</b>	<b>Introduction</b>	<b>39</b>
<b>4.2</b>	<b>Materials and Methods</b>	<b>40</b>
4.2.1	PFHnD Synthesis and Characterization	40
4.2.2	Cell Culture	40
4.2.3	Sonoporation and Data Processing	41
4.2.4	Size Variation	42
4.2.5	MTT Assay	42
<b>4.3</b>	<b>Results</b>	<b>43</b>
4.3.1	Dye	44
4.3.2	Concentration	46
4.3.3	Pulse Number	48
4.3.4	Fluence	50
4.3.5	Size Dependence of Therapeutic Delivery	52
4.3.6	Cell Variation	54
4.3.7	Long Term Viability	55
<b>4.4</b>	<b>Discussion</b>	<b>57</b>
<b>4.5</b>	<b>Conclusion</b>	<b>62</b>
<b>4.6</b>	<b>Acknowledgments</b>	<b>62</b>
<b>CHAPTER 5. Double Emulsion PFCnDs for Hydrophilic Drug Delivery</b>		<b>63</b>
<b>5.1</b>	<b>Introduction</b>	<b>63</b>
<b>5.2</b>	<b>Materials and Methods</b>	<b>64</b>
5.2.1	dePFHnD Synthesis and Characterization	64
5.2.2	Lasing and Heating	66
5.2.3	Focused Ultrasound Parameter Optimization	67
5.2.4	Agarose Gel Electrophoresis	68
5.2.5	Ultrasound/Photoacoustic Imaging of Phantom and Vaporization Threshold	69
5.2.6	Poly(I:C) dePFHnD Griess Assay	71
5.2.7	MTT	72
<b>5.3</b>	<b>Results and Discussion</b>	<b>73</b>
5.3.1	Formulation Optimization	73
5.3.2	Release Quantification	76
5.3.3	Delivery of Poly I:C	81
5.3.4	PA Trackability	85
<b>5.4</b>	<b>Conclusion</b>	<b>86</b>
<b>CHAPTER 6. Future Works</b>		<b>88</b>
<b>6.1</b>	<b>Repeated Optical Nanodroplet Vaporization</b>	<b>88</b>
6.1.1	High Fluence Suppression	88
6.1.2	Vaporization Thresholds of Very High Boiling Point PFC and Differential Dye Loading	90
6.1.3	Preconditioning for Multiplexing	91
6.1.4	Condensation Synthesis of High Boiling Point Perfluorocarbon Nanodroplets	92
6.1.5	Vaporization Threshold Tuning Through Shell Engineering	93

<b>6.2</b>	<b>Laser Induced Sonoporation</b>	<b>94</b>
6.2.1	Formulation Variation	94
6.2.2	Impact of Proximity of the Particle on Sonoporation	94
<b>6.3</b>	<b>Double Emulsion Nanodroplets</b>	<b>95</b>
6.3.1	Improving Release	95
6.3.2	Develop More Biocompatible and Optimized Fluorosurfactant	95
6.3.3	Synthesis Utilizing Microfluidics	96
<b>APPENDIX A. Supplementary Information for Chapter 3: Optical Vaporization</b>		
	<b>Threshold Characterization</b>	<b>98</b>
<b>A.1</b>	<b>Dye Standard for Quantifying Concentration within the Nanodroplets</b>	<b>98</b>
<b>A.2</b>	<b>Nanoparticle Size and Material Properties PFC</b>	<b>98</b>
<b>A.3</b>	<b>Preconditioning Comparison</b>	<b>99</b>
<b>APPENDIX B. Supplementary Information for Chapter 4: Sonoporation</b>		<b>101</b>
<b>A.1</b>	<b>Stitched Images Comparing PFHnDs Formulated with Different Dyes</b>	<b>102</b>
<b>A.2</b>	<b>Stitched Images of Fluorescent Dextran Bead Delivery</b>	<b>104</b>
<b>APPENDIX C. Supplementary Information for Chapter 5: Double Emulsion</b>		
	<b>Characterization</b>	<b>105</b>
<b>A.1</b>	<b>Concentration Standards</b>	<b>105</b>
<b>A.2</b>	<b>FSL dePFHnD Characterization</b>	<b>106</b>
<b>A.3</b>	<b>Confocal Validation of the Double Emulsion</b>	<b>108</b>
	<b>REFERENCES</b>	<b>111</b>

## LIST OF TABLES

Table 1	Conditions used for each experiment in Chapter 3.	18
Table 2	Size and Composition of the Nanodroplets	99
Table 3	Critical Temperature of Cores Used in Nanodroplets	99

## LIST OF FIGURES

- Figure 1 – The schematic illustrates the different shell components and different perfluorocarbons (PFC) used in this study, along with cryo-TEM (cryogenic transmission electron microscopy) images taken of each shell formulation with perfluorohexane (PFH). The scale bar represents 100 nm. 13
- Figure 2 – An illustration of the different phantoms with the corresponding ultrasound and photoacoustic images produced from each setup. Within the tube phantom, nanodroplets were suspended in water within the tubular void, while in the polyacrylamide phantom, the nanodroplets were embedded throughout the phantom. 16
- Figure 3 – (A) Differential US and PA images of lipid, PFH, and nanodroplets within the tube phantom at different pulse numbers. (B) The normalized integrated US intensity of the same nanodroplets over the course of 100 pulses at  $75 \text{ mJ/cm}^2$ . (C) Mean size and concentration taken by the NTA over the course of the 100 pulses. Error bars represent standard errors. 22
- Figure 4 – The vaporization threshold of lipid, PFH, nanodroplets ( $n = 6$ ) embedded in a polyacrylamide phantom at different laser pulse repetition frequencies (PRF; 10 Hz, 6 Hz, 3 Hz, and 1 Hz). The different PRFs did exhibit a statistical difference (repeated measures ANOVA;  $F(3, 20) = 4.146$ ,  $p = 0.0194$ ), with differences detected between 10 Hz and 3 Hz/1 Hz ( $p = 0.0014$  and  $p = 0.0029$ ) and 6 Hz and 3 Hz/1 Hz ( $p = 0.0005$  and  $p = 0.0012$ ). However, the mean differences were small ( $\sim 0.8 \text{ mJ/cm}^2$ ). 25
- Figure 5 – (A) The vaporization threshold of the different formulations of the nanodroplets ( $n = 6$ ) after exposure to varying numbers of laser pulses ( $75 \text{ mJ/cm}^2$ ). Significant differences in the vaporization threshold were observed among the different shells ( $F(2, 15) = 172.3$ ,  $p < 0.0001$ ). Tukey's comparison test indicated significant differences between all shells ( $p < 0.0001$ ). (B) Dye content per formulation ( $n = 3$ ). Error bars represent the standard deviation. (C) The decay behavior of the normalized integrated US intensity for each formulation ( $n = 6$ ) after repeated lasing at  $75 \text{ mJ/cm}^2$ . The half-life for each formulation was determined by fitting each curve with an exponential decay. 28

Figure 6	– UV-vis spectra comparison of Epolight 3072 in DMSO before and after being lased at 1064 nm at 90 mJ/cm <sup>2</sup> for 0, 200, and 400 pulses.	30
Figure 7	– (A) The vaporization threshold of lipid, PFH, nanodroplets (n = 6) embedded in a polyacrylamide phantom compared to those within the tube phantom over repeated lasing at 75 mJ/cm <sup>2</sup> . The environments exhibited a statistically significant difference (paired <i>t</i> -test, <i>p</i> < 0.0001). (B) The decay behavior of the normalized integrated US intensity for each environment (n = 6) after repeated lasing (75 mJ/cm <sup>2</sup> ).	32
Figure 8	– A) Ultrasound image of the interface between the phantom and the water along with the push location. B) The interface overlaid with multiple frames of the calculated axial displacement, depicting the propagation of surface waves over time. C) A schematic illustrating the push locations and the direction of wave speed measurement from each push. D) Wave speeds were calculated by a linear fit of the distance traveled by the peak of the wave over time. The surface wave speed in the polyacrylamide phantom was determined to be 5.51 ± 0.09 m/s and the Young's modulus was calculated to be 100.26 ± 3.11 kPa.	34
Figure 9	– (A) The vaporization thresholds of lipid nanodroplets with different cores embedded in a polyacrylamide phantom that has been cooled to 0 °C. (B) The averaged vaporization thresholds for each core are plotted against 90% of the critical temperature for each core and fitted with a linear fit with an x-intercept set to 0 °C. Error bars represent the standard deviation of n = 6 replicates.	36
Figure 10	– Schematic illustrating the process in which sonoporation is studied. PFHnD are added to cells with calcein (green) acting as a model drug and then the cells are lased. The excess calcein and droplets are washed out and the cells are stained with a nuclei stain (Hoechst 33342) and a live stain (calcein red-orange AM).	43
Figure 11	– A) The absorbance spectrum of Epolight 3072 and IR1048. B) The DLS size measurement of the resulting PFHnDs synthesized with different dyes averaged from n = 3 measurements. Z-average of Epolight 3072 and IR1048 were 333.5 ± 4.8 nm and 335.7 ± 1.4 nm respectively. C) The sonoporation rate and the mean fluorescence intensity of successfully sonoporated cells for each formulation of PFHnD lased at 100 pulses at 60 mJ/cm <sup>2</sup> . The sonoporation rates of	45

IR1048 and Epolight 3072 exhibit statistically significant differences (un-paired t-test,  $p=0.025 < 0.05$ ). D) The viability assessed through fluorescence of calcein red-orange of the cell population in the ROI and specifically the sonoporated cells as a function of concentration. C) and D) are the summation of  $n = 3$  replicates with approximately 3000-8000 cells within the ROI. E) Representative images of the lased cells.

- Figure 12 – A) The sonoporation rate and the mean fluorescence intensity of successfully sonoporated cells as a function of the PFHnD concentration lased at 100 pulses at  $60 \text{ mJ/cm}^2$ . B) The viability assessed through fluorescence of calcein red-orange of the cell population in the ROI and specifically the sonoporated cells as a function of concentration. C) Representative images of the lased cells. A) and B) are the summation of  $n = 3$  separate replicates with approximately 3000- 8000 cells within the ROI. 48
- Figure 13 – A) The sonoporation rate and the mean fluorescence intensity of successfully sonoporated cells as a function of the pulses ( $60 \text{ mJ/cm}^2$ ) the PFHnDs and HADMSCs were lased. B) The viability assessed through fluorescence of calcein red-orange of the cell population in the ROI and specifically the sonoporated cells as a function of number of pulses. C) Representative images of the lased cells. A) and B) are the summation of  $n = 3$  separate replicates with approximately 3000- 8000 cells within the ROI. 49
- Figure 14 – A) The sonoporation rate and the mean fluorescence intensity of successfully sonoporated cells as a function of the fluence at which the PFHnDs and HADMSCs were lased (100 pulses). B) The viability assessed through fluorescence of calcein red-orange of the cell population in the ROI and specifically the sonoporated cells as a function of fluence. C) Representative images of the lased cells. A) and B) are the summation of  $n = 3$  separate replicates with approximately 3000- 8000 cells within the ROI. 51
- Figure 15 – A) The sonoporation rate of dextran beads (mw: 3000-5000 Da) labeled with fluorescein isothiocyanate (FITC) into HADMSCs that were lased ( $60 \text{ mJ/cm}^2$  with 300 pulses) with PFHnDs ( $3 \times 10^{10}$  particles/mL). B) The viability assessed through fluorescence of calcein red-orange of the cell population in the ROI and specifically the sonoporated cells as a function of fluence. C) Representative images of the lased cells. A) and B) are the summation of  $n = 3$  separate replicates with approximately 3000- 8000 cells within the ROI. 53

Figure 16	– Representative images of sonoporation in different cell types: A) 4T1 B) Hek293T, and C) Neonatal Rat Ventricular Myocytes (NRVM). Scale bars represent 1 mm.	54
Figure 17	– MTT assay performed on HADMSCs seeded in a 96 well plate. The PFHnDs were added at concentrations equivalent to $3 \times 10^{10}$ droplets per mL and select wells were lased at different fluences for 100 pulses. The bars represent the mean of $n = 5$ replicates with error bars representing the standard deviation.	56
Figure 18	– Schematic illustrating the overall structure of the double emulsion along with cryo-TEM images taken of droplets synthesized using only a single emulsion and those with a double emulsion.	73
Figure 19	– A) The loading efficiency of calcein within dePFHnDs as a function of RAN concentration used during the formulation with $n = 3$ replicates. Differences in the means of the conditions were found to be statistically significant (one-way anova ( $F(3, 8) = 123.0, p < 0.0001$ ) with significant differences found between 0 mg/mL of RAN and all other concentrations through Tukey’s multiple comparison test ( $p < 0.0001$ ). B) The size distribution of the resulting dePFHnDs measured by DLS. The size distributions and z-averages are an average of three measurements. C) MTT assay performed to assess the viability of RAW 264.7 cells that were incubated with various concentrations of dePFH synthesized with RAN (50 mg/mL). Error bars represent the standard deviation of $n = 8$ replicates.	75
Figure 20	– The release profile for the dePFHnDs at A) varying number of pulses at $70 \text{ mJ/cm}^2$ and B) at 100 pulses at varying fluences. Bar plots represent mean while the error bars indicate the standard deviation of $n = 3$ replicates.	77
Figure 21	– The release efficiency of RAN dePFHnDs as a function of A) peak negative pressure (PNP), B) pulse repetition interval (PRI), C) duty cycle, and D) duration at different PNPs. All experiments were conducted under the following conditions, with the exception for the condition being tested: PNP: 1.44 MPa, duty cycle: 50%, PRI: 300 ms, and duration 120 s. Each point represents the mean while the error bars indicate the standard deviation of $n = 3$ replicates.	78
Figure 22	– The release profile of RAN dePFHnD at various temperatures. Each point represents the mean of $n = 3$ replicates with error bars representing the standard deviation.	80

Figure 23	– A) The change in z-average size over the course of several days as taken by DLS. B) The release of calcein measured as a percentage of the total encapsulated amount over the course of 8 days. Each measurement is an average of n = 3 replicates with the error bars representing standard deviation.	81
Figure 24	– A) Agarose gel electrophoresis of poly I:C loaded into dePFHnDs and subjected to HIFU (PNP: 2.16 MPa, PRI: 15ms, duration 5 minute) in comparison to unprocessed poly I:C. The released poly I:C shows no signs of degradation. B) The activity of poly I:C remains unchanged after the two probe sonication steps needed to produce dePFHnDs, as indicated in the Griess assay. Bar plots represent the mean, while the error bars represent the standard deviation of n = 3 replicates. N.S. represents not significant (one-way ANOVA $F(2, 6) = 4.242$ , $p = 0.0711 > 0.05$ ).	82
Figure 25	– Griess assay of dePFHnD exposed to HIFU (PNP: 2.16 MPa, PRI: 15 ms, duration: 5 minutes) and incubated with RAW 264.7 macrophages (N = 8) at different concentrations of the dePFHnD. Statistically significant differences in the mean were detected (one-way ANOVA, $p < 0.0001$ ) with significant differences detected between 1:100 dePFHnD and PBS (Tukey's multiple comparison, $p < 0.0001$ ).	83
Figure 26	– A) Image of the setup utilized to hold a film bottom 24 well plate to allow for FUS exposure from the bottom in a water bath held at 37°C. B) Nitrite generated from the RAW 264.7 macrophages that were incubated with poly I:C alone (0.1mg/mL), dePFHnDs, dePFHnDs and exposed to FUS (PNP: 1.08 MPa, PRI: 15 ms, duration: 5 minutes), PBS, and PBS with FUS exposure with n = 8 replicates. Differences in the mean were observed (one-way ANOVA, $F(4, 35) = 94.69$ , $P < 0.0001$ ) with significant differences detected between dePFHnD + FUS and all other groups (Tukey's multiple comparison, $p < 0.0001$ represented by ***).	84
Figure 27	– A) US and PA images of dePFHnDs after exposure to HIFU of varying conditions and the resulting release percentages at each point. B) Integrated PA intensity of the dePFHnDs at different release points. C) Integrated US intensity at different release points.	86
Figure 28	– The normalized absorbance spectrum of near-IR dyes dissolved in chloroform that exhibit peak absorptions around 775 nm and 1064 nm. These could be candidates for dyes that	92

could be used in nanodroplet formulations that would allow for multiplexing.

- Figure 29 – A) The UV-vis spectra of Epolight 3072 dissolved in chloroform at different concentrations and B) the resulting standard for the absorbance at 1060 nm relative to the concentration of the dye. 98
- Figure 30 – The preconditioning behavior of PFHnDs based upon the different dye. The droplets were embedded in a polyacrylamide and lased for multiple pulses at 75 mJ/cm<sup>2</sup>. 100
- Figure 31 – An example of the data process is shown. The ROI is defined by the size of the laser beam (diameter: 7 mm). Live cells are defined by having calcein red-orange fluorescence intensity greater than 1.5x the background and sonoporated cells are defined by having fluorescence intensity that is 1.5x the background. The image on the right shows the classification of all cells identified by Hoechst 33342 in yellow. The subpopulation of live sonoporated cells is shown in pink. 101
- Figure 32 – Brightfield image showing the accumulation of microbubbles after repeated lasing for 600 pulses. 102
- Figure 33 – All samples analyzed to compare the different dyes (Epolight 3072 and IR1048) used in this study. Conditions are as follows: PFH concentration: 3x10<sup>10</sup> particles/mL, laser fluence: 60 mJ/cm<sup>2</sup>, 100 pulses. 104
- Figure 34 – All HADMSC cells incubated with FITC-tagged dextran beads (3-5kDa). From left to right: Hoechst, Calcein, Calcein Red-Orange am, merge. Laser settings are as follows: 60 mJ/cm<sup>2</sup>; 300 pulses. 104
- Figure 35 – Calcein standard utilized to convert fluorescence intensity to concentration of calcein. 105
- Figure 36 – The nitrite standard that was used to determine the amount of nitrite that was generated during the griess assay. 106
- Figure 37 – The viability of RAW 264.7 cells incubated with different concentrations of dePFHnDs formulated with FSL. Each bar represents the mean of n=6 replicates with the error bars representing standard deviation. 107

Figure 38	– The release efficiency of dePFHnDs formulated with FSL after A) repeated lasing at 70 mJ/cm <sup>2</sup> and B) after lasing at various fluences.	107
Figure 39	– The release efficiency of FSL dePFHnDs as a function of A) peak negative pressure (PNP), B) pulse repetition interval (PRI), C) duty cycle, and D) duration at different PNPs. All experiments were conducted under the following conditions, except for the condition being tested: PNP: 1.44 MPa, duty cycle: 50%, PRI: 300 ms, and duration 120 s. Each point represents the mean while the error bars indicate the standard deviation of n = 3 replicates.	108
Figure 40	– A) The averaged DLS size measurement (n = 3) of the FSL dePFHnD with Cy3 without and with a PEI coating. The z-average size of the dePFHnD was found to be 392.1. After coating with PEI, the size increased modestly to 502.9. B) Representative zeta potential measurements of the FSL dePFHnD with Cy3 with and without a PEI coating. The average zeta potential over three measurements for the uncoated FSL dePFHnD was -39.93 and 41.5 for the coated FSL dePFHnD.	109
Figure 41	– Confocal images of PEI coated FSL dePFHnDs loaded with calcein and cy3 that were incubated with HeLa cells, which are stained with Celltracker blue. The images show the hydrophobic cy3 (top left), hydrophilic calcein (top right), celltracker blue (bottom left), and a merged image (bottom right). The scale bars are 100 μm.	110

## LIST OF SYMBOLS AND ABBREVIATIONS

ADV	Acoustic Droplet Vaporization
Cryo-TEM	Cryogenic Tunneling Electron Microscopy
Cy3	Cyanine 3
dePFHnD	Double Emulsion Perfluorohexane Nanodroplet
DLS	Dynamic Light Scattering
DMEM	Dulbecco's Modified Eagle Medium
DOPE	1,2-dioleoyl-sn-glycero-3-phosphoethanolamine
DOTAP	1,2-Dioleoyl-3-trimethylammonium propane
DSPC	1,2-distearoyl-sn-glycero-3-phosphocholine
DSPE-PEG2k	1,2-distearoyl-sn-glycero-3-phosphoethanolamine-N-[methoxy(polyethylene glycol)-2000]
EDTA	Ethylenediaminetetraacetic acid
EPR	Enhanced Permeability and Retention
F-68	Polyoxyethylene-polyoxypropylene block copolymer (Pluronic F-68)
FBS	Fetal Bovine Serum
FITC	Fluorescein Isothiocyanate
FSH	Krytox 157 FSH
FSL	Krytox 157 FSL
FUS	Focused Ultrasound
HADMSC	Human Adipose-Derived Mesenchymal Stem Cells
HBSS	Hank's Balanced Salt Solution
HIFU	High Intensity Focused Ultrasound
MEM	Minimum Essential Medium

MTT	3-(4,5-dimethylthiazol-2-yl)-2,5-diphenyltetrazolium bromide
Nd:YAG	Neodymium-doped yttrium aluminum garnet
NTA	Nanoparticle Tracking Assay
ODV	Optical Droplet Vaporization
P/S	Penicillin-Streptomycin
PA	Photoacoustic
PBS	Phosphate Buffered Saline
PEG	Polyethylene Glycol
PFC	Perfluorocarbon
PFCnD	Perfluorocarbon nanodroplet
PFD	Perfluorodecaline
PFH	Perfluorohexane
PFHept	Perfluoroheptane
PFHnD	Perfluorohexane Nanodroplet
PFO	Perfluorooctane
PFP	Perfluoropentane
Poly I:C	Polyinosinic:polycytidylic acid
PRF	Pulse Repetition Frequency
RAN	008-fluorosurfactant
RCF	Relative Centrifugal Force
ROI	Region of Interest
RPMI 1640	Roswell Park Memorial Institute 1640 Medium
TAE	Tris-acetate-EDTA
TEMED	tetramethylethylenediamine
TLR3	Toll-like receptor 3

$T_m$  Melting temperature

US Ultrasound

USPA Ultrasound Photoacoustics

## SUMMARY

Perfluorocarbon nanodroplets have been primarily explored as a next-generation contrast agent for ultrasound imaging, providing significant advantages over microbubbles in terms of circulation time and size, which enables them to extravasate and reach extravascular targets. Furthermore, these nanoparticles can be triggered acoustically or optically to form microbubbles in situ. While acoustic droplet vaporization has been extensively studied, optical droplet vaporization holds promise as an alternative approach. It allows for the incorporation of photoacoustic imaging to visualize vaporization and can be used to vaporize high boiling point cores safely and repeatedly.

In this dissertation, optically triggerable PFCnDs are further developed as theranostic agents. The formulation of PFCnDs is varied to gain a better understanding of optical droplet vaporization and to improve the particle's imaging performance. The therapeutic applications are explored from two angles: impact of the vaporization and release of encapsulated drugs.

In CHAPTER 3, the performance of optically activatable PFCnDs are examined, considering factors such as shell and core materials, laser parameters, and environmental conditions. Novel longitudinal behaviors of the nanodroplets are described that can allow for more effective detection in the body and provide insights into how the formulation impacts the vaporization threshold. These findings provide a better foundation for advancing our understanding of optical droplet vaporization.

In CHAPTER 4, the effect of lasing the nanodroplets in close proximity to the cells are explored. The nanodroplets exhibit a similar behavior to sonoporation, creating pores in the cell membrane that enable extracellular molecules to enter the cytoplasm. The different conditions required to optimize this behavior and viability are explored in detail

such as the concentration of the PFCnDs, laser fluence, pulse number, and size of the molecules that can enter.

In CHAPTER 5, double emulsion perfluorohexane nanodroplets (dePFHnDs) are developed by modifying the formulation of PFCnDs to encapsulate hydrophilic molecules. This new class of PFCnDs can be tracked photoacoustically and triggered to release drugs acoustically. Photoacoustic monitoring can be performed without releasing the encapsulated drug, allowing for estimations of release based upon signal reduction.

In summary, this dissertation represents an advancement of PFCnDs as a theranostic agent. Our understanding of optical droplet vaporization is improved, allowing for better diagnostic applications, and expand the therapeutic capabilities of these nanodroplets in drug delivery. These developments contribute to making PFCnDs a more effective drug delivery agent.

# CHAPTER 1. INTRODUCTION

## 1.1 Ultrasound Imaging

Ultrasound (US) imaging provides an attractive balance between cost, depth penetration, and safety, making it one of the most ubiquitous clinical imaging modalities. Although its commonly associated with imaging of fetuses, medical ultrasound has found uses for a variety of procedures including echocardiography for heart visualization, doppler ultrasound to assess blood flow, and guided needle placement and biopsies, to mention a few. Medical US imaging operates by transmitting a sound wave, typically above 1 MHz in frequency, into the target and receiving backscattered sound waves to form an image. Due to the frequency chosen, ultrasound imaging has limited attenuation, which allows for excellent depth penetration in real-time.

The backscattering occurs when the initial sound wave hits a boundary of different density, and a fraction is reflected back to the transducer. The reflection coefficient,  $R$ , is the ratio of reflected pressure to incident pressure and is defined by:

$$R = \frac{Z_2 - Z_1}{Z_2 + Z_1} \quad (1)$$

where  $Z_1$  and  $Z_2$  are the acoustic impedance of the two materials that make up boundary.<sup>1</sup> Acoustic impedance,  $Z$ , is a function of both the density of the material and the speed of sound within the material. It can be thought of as a materials resistance to sound propagation. As the speed of sound is assumed to be 1540 m/s in most tissues, US imaging

is functionally based upon the scattering of sound waves based upon differences in density, where the intensities of the resulting backscatter are proportional to the difference.

However, too drastic of a difference between the mediums can result in either no reflection or complete reflection. This limits the application of medical US to primarily soft tissues, generally avoiding bones and the lungs.

## 1.2 Photoacoustic Imaging

Photoacoustics (PA) operates similarly to US imaging in that the read out is US, allowing it to use much of the same hardware as US. However, PA utilizes light excitation as the input to locally heat the target. Under the proper conditions, this produces a thermal expansion generating a pressure wave, which can be detected by the US transducer.<sup>2</sup> This allows for imaging based upon light absorption at a particular wavelength. The generated pressure wave intensity can be described by:

$$p_0 = F \times \mu_a \times \Gamma \quad (2)$$

where  $F$  is the local light fluence,  $\mu_a$  is the absorbance coefficient of the target, and  $\Gamma$  is the Grüneisen parameter, which is a temperature dependent variable that describes the conversion efficiency from energy to pressure based upon the speed of sound, specific heat of the material, and thermal expansion.<sup>3</sup>

As PA is highly dependent on the use of light, the scattering of tissue along with the absorption of endogeneous chromophores must be considered. This typically limits the wavelengths to near infrared (650 – 950 nm, 1000– 1350 nm), in which there is minimal

absorbance and scattering from tissues.<sup>4</sup> PA imaging of endogenous contrast agents can be used to provide functional information such as estimating the blood oxygen saturation based upon the ratio of deoxygenated and oxygenated hemoglobin.<sup>5</sup>

While there are numerous endogenous contrast agents that can be imaged, PA can also benefit from the addition of exogenous contrast agents such as dyes or metallic nanoparticles.<sup>6</sup> This can allow for molecular based imaging.

### **1.3 Contrast Enhanced US**

Ultrasound, while useful for delineating clear anatomical boundaries, often suffers from a lack of contrast between soft tissues within the body that can result in missed identification of lesions.<sup>7,8</sup> This has led to the development of contrast enhanced US, which utilizes exogenous contrast agents that can be used to highlight microvasculature<sup>9</sup> and differentiate soft tissue.<sup>7</sup>

#### *1.3.1 Microbubbles*

Exogenous contrast agents in the form of microbubbles – gas bubbles stabilized by a surfactant from proteins, lipids or polymers – are the only class of FDA approved US contrast agent.<sup>10,11</sup> Microbubbles provide an excellent form of contrast due to the large acoustic impedance mismatch from tissue.

Originally, microbubbles were identified when ultrasound contrast was detected after an injection of indocyanine green into the bloodstream due to the co-administration of air bubbles during the injection.<sup>12</sup> These early microbubbles had poor size control,

exhibited limited contrast and had a limited half-life as the internal core was air, being composed primarily of low molecular weight gasses such as nitrogen and oxygen.

Advancements were made to allow for longer half-lives by utilizing higher molecular weight gasses such as perfluorobutane (PFB), which were less susceptible to diffusion and less soluble in water.<sup>13</sup> Surfactants were added that both enhanced the stability, size control, and contrast from the microbubble.<sup>14</sup>

Furthermore, other work takes advantage of the microbubbles unique resonance and capability to be influenced by ultrasound for other biological therapeutics. One example is the stimulating microbubbles to undergo stable cavitation, leading to the creation of pores in the cell membrane, which facilitates the delivery of genes and drugs, in a process commonly referred to as sonoporation.<sup>15,16</sup> The effects can also be observed on a more macro level with microbubbles in tandem with focused ultrasound (FUS) being capable of opening the blood brain barrier.<sup>17</sup> However, one of the major limitations of microbubbles is their large size, which prevents them from exiting the vasculature.

### *1.3.2 Perfluorocarbon Nanodroplets (PFCnDs)*

Nanodroplets were developed in direct response to the limitations of microbubbles. They can be thought of as a “condensed” microbubble as they build upon many of the key advancements made by microbubbles. Much like their microbubble counterparts, nanodroplets have been formulated out of similar shell materials such as BSA, lipids, and various polymers, and instead of gas, nanodroplets have a perfluorocarbon liquid core that allows them to be synthesized at sub-micron sizes and triggered in situ through acoustic or optical means, resulting in a five-fold expansion in diameter, to form a microbubble. To

enable proper manipulation of this behavior in vivo, it is necessary to understand the underlying thermodynamics of the vaporization process.

## 1.4 Thermodynamics of PFCnDs

### 1.4.1 Laplace Pressure

Early formulations of perfluorocarbon nanodroplets utilized perfluoropentane as the core that demonstrated surprising stability at 37°C despite its low boiling point of 29°C. This behavior has extended to even lower boiling point perfluorocarbons such as perfluorobutane (-1.7°C) and octafluoropropane (-36.7°C).<sup>18</sup> Initial explanations focused on Laplace pressure as the key reason for this stability at high temperatures. Laplace pressure describes the increase in pressure experienced due to the curvature and surface tension at an interface, and is described by the following:

$$\Delta P = P_{inside} - P_{outside} = \gamma \left( \frac{1}{R_1} + \frac{1}{R_2} \right) \quad (3)$$

Where  $\Delta P$  is the increased pressure due to the Laplace pressure,  $P_{inside}$  is the pressure experienced inside the curved surface,  $P_{outside}$  is the pressure outside of the surface (typically atmospheric pressure),  $R_1$  and  $R_2$  are the principal radii of curvature, and  $\gamma$  is the surface tension. For spherical perfluorocarbon nanodroplets, Laplace pressure simplifies down to (Equation 4):

$$\Delta P = \frac{2\gamma}{R} \quad (4)$$

With the fundamental take away being that as the nanodroplet size decreases, the Laplace pressure increases. This increase in pressure shifts the phase diagram such that the nanodroplets experience stability at higher temperatures. While seemingly plausible, this explanation does appear to fall apart when considering experimental results and consequences of this high pressure.

Surface tension measurements of phospholipids, which are the most commonly used shell material, indicate that below their  $T_m$  or melting temperature, lipid shells are insoluble and have surface tensions of almost 0 N/m.<sup>19</sup> Such tensions would yield in little to no stabilizing Laplace pressure, resulting in vaporization of the nanodroplets.

#### *1.4.2 Nucleation Theory*

Recently, the surprising stability has been explained through other means. Acoustic droplet vaporization when modeled through the lens of homogeneous nucleation theory suggests that vaporization does not occur until the temperature reaches 90% of the critical temperature.<sup>20</sup> This has been further supported by observations of a reduction in vaporization temperature of PFCnDs after the addition of nucleation sites using nanoparticles in the nanodroplet core. Homogeneous nucleation theory provides more accurate predictions of vaporization thresholds of super-heated perfluorocarbons, but there are some discrepancies, suggesting that there is interplay between both homogeneous nucleation and Laplace pressure.<sup>20</sup>

### **1.5 ODV Nanodroplets and Their Applications**

To optically stimulate these nanodroplets, a photoabsorber, such as a dye or nanoparticle, is incorporated into the nanodroplet.<sup>21</sup> Optical stimulation allows for simultaneous monitoring of the vaporization without any acoustic interference. This permits the detection of photoacoustic contrast and can be combined with high frame rate ultrasound imaging to visualize the vaporization and recondensation of PFCnDs formulated with perfluorocarbons that have boiling points higher than physiological temperature.<sup>22</sup> This combination can allow for super-resolution,<sup>23</sup> background-free imaging,<sup>24</sup> multiplexing through the use of multiple dyes,<sup>25</sup> enhancement of vaporization dynamics through ultrasound,<sup>26</sup> and image-guided drug delivery.<sup>27</sup> However, the ODV fluence threshold of sub-micrometer droplets have not been well characterized due to the use of a variety of different absorbers and synthesis methods. It remains unclear what factors influence the laser fluence required for vaporization.

## CHAPTER 2. SPECIFIC AIMS

Optically triggered perfluorocarbon nanodroplets hold significant promise as a theranostic agent, due to their compatibility with photoacoustics and ultrasound imaging. However, their current state reveals several shortcomings: there is a lack of understanding of the fundamental properties of ODV, limited knowledge regarding the therapeutic implications of ODV, and a fundamental limitation in terms of the drugs that could be encapsulated.

To address these limitations the following aims were devised:

### **2.1 Aim 1: Enhance Understanding of Optical Droplet Vaporization (ODV)**

To gain more insight on ODV from a theoretical and a practical perspective, PFCnDs will be characterized with different formulations and under diverse conditions to identify the impact on the long-term behavior of the PFCnDs. Specifically, we will investigate the roles of surface tension and core critical temperature on the vaporization threshold over repeated vaporization. These investigations will further provide insights into factors that may affect vaporization of the nanodroplets within the body, potentially guiding the development of strategies to enhance detection. Consequently, these findings will lay a more robust foundation for advancing our understanding of optical droplet vaporization.

### **2.2 Aim 2: Explore the Impact of ODV On Intracellular Delivery**

Microbubbles have been utilized for intracellular therapeutic delivery via a technique known as sonoporation. Recent studies have shown that ADV can also be utilized to for this purpose, suggesting that ODV may be capable of sonoporation. To assess this potential, a range of conditions such as PFCnD concentration, laser fluence, number

of pulses will be explored to identify those which result in the highest delivery and greatest viability. Efforts will be taken to characterize any limitations of this approach concerning cell types and molecular size.

### **2.3 Aim 3: Expand The Capabilities of PFCnDs For Drug Delivery**

Current drug delivery approaches using PFCnDs are limited to hydrophilic drugs and cannot be monitored without releasing the payload. In this aim, modifications to the PFCnDs formulations are made to allow for the development of double emulsion perfluorohexane nanodroplets (dePFHnDs). Using a high boiling point perfluorocarbon, this will allow for repeated vaporization without impacting release of the encapsulated hydrophilic cargo, and the photoacoustic signal can be utilized to estimate drug release.

The accomplishment of these aims would represent an advancement of PFCnDs as a theranostic agent. By improving both the diagnostic and therapeutic aspects of PFCnDs, this research contributes to the development of PFCnDs as a more effective drug delivery agent.

# CHAPTER 3. OPTICAL VAPORIZATION THRESHOLD AND LONGITUDINAL PERFORMANCE OF PERFLUOROCARBON NANODROPLETS

This chapter has been adapted from the following publication: Zhao, A. X.; Zhu, Y. I.; Chung, E.; Lee, J.; Morais, S.; Yoon, H.; Emelianov, S. Factors Influencing the Repeated Transient Optical Droplet Vaporization Threshold and Lifetimes of Phase Change, Perfluorocarbon Nanodroplets. *Nanomaterials* 2023.<sup>28</sup>

## 3.1 Introduction

Perfluorocarbon nanodroplets (PFCnDs) were developed as an alternative ultrasound contrast agent to microbubbles. These particles are synthesized at small sizes to allow them to extravasate and reach extravascular targets that are beyond the reach of conventional microbubbles.<sup>18,29–32</sup> Upon reaching the targeted location, these nanodroplets can then be stimulated acoustically or optically to form a microbubble in situ. This ability to extravasate and be remotely stimulated allows for the nanodroplets to be used for extravascular applications such as examining lymph node trafficking and cancer treatment through drug delivery and tissue occlusion.<sup>25,29,33</sup> Furthermore, the nanodroplet vaporization itself can be utilized for other applications such as blood-brain barrier opening and cell sonoporation.<sup>34–37</sup>

To optically stimulate these nanodroplets, a photoabsorber, such as a dye or nanoparticle, is incorporated into the nanodroplet.<sup>21</sup> Optical stimulation allows for simultaneous monitoring of the vaporization without any acoustic interference. This

permits the detection of photoacoustic contrast and can be combined with high-frame-rate ultrasound imaging to visualize the vaporization and recondensation of PFCnDs formulated with perfluorocarbons that have boiling points higher than physiological temperatures.<sup>22</sup> This combination can allow for super-resolution,<sup>23</sup> background-free imaging,<sup>24</sup> multiplexing through the use of multiple dyes,<sup>25</sup> enhancement of vaporization dynamics through ultrasound,<sup>26</sup> and image-guided drug delivery.<sup>27</sup> However, the ODV fluence threshold of sub-micrometer droplets has not been well characterized due to the use of a variety of different absorbers and synthesis methods. It remains unclear what factors influence the laser fluence required for vaporization.

In contrast, acoustic droplet vaporization (ADV) has been extensively characterized. Various factors related to the droplets, such as droplet size, surface tension, droplet concentration, and core boiling temperature, along with ultrasound activation parameters, including frequency, pulse repetition frequency, number of cycles, and pressure, have been found to impact the ADV threshold.<sup>38–41</sup> Some studies have shown similar dependencies in ODV thresholds. For instance, ODV thresholds depend on the boiling temperature of the PFC core, where droplets containing octafluoropropane (boiling point:  $-36.7$  °C) possess a ninefold lower vaporization threshold than PFP (boiling point:  $28$  °C).<sup>31</sup> However, it is unclear how similar ODV is to ADV.

Most relevant ODV work has examined larger droplets ( $\sim 1$   $\mu\text{m}$  diameter) to characterize the underlying dynamics and physics of vaporization and utilized optical methods to observe the vaporization.<sup>32,42–44</sup> Although studying larger droplets can provide insights into the vaporization phenomenon, these droplets are not within the clinically relevant size range capable of extravasation, and the observed behaviors may not translate

to smaller sizes. Thus, it is important to characterize the vaporization thresholds of smaller droplets (~300 nm in diameter) to properly engineer their properties.

Furthermore, previous works have primarily characterized the vaporization thresholds optically. This approach is unable to visualize transient vaporization behavior at the sub-micron scale, as the phenomenon occurs on the order of micro- to milliseconds and may not have any relevance for imaging within the body.<sup>26,42</sup> In this chapter, we take advantage of high frame rate ultrasound to visualize optically triggered vaporization and characterize which factors, such as shell material, environment, laser pulse repetition frequency (PRF), and nanodroplet core, influence the vaporization threshold of clinically relevant-sized nanodroplets.

## **3.2 Materials And Methods**

### *3.2.1 Nanodroplet Synthesis and Characterization*

Nanodroplets with different shells were synthesized using probe sonication with the same settings among all the different formulations (Figure 1).

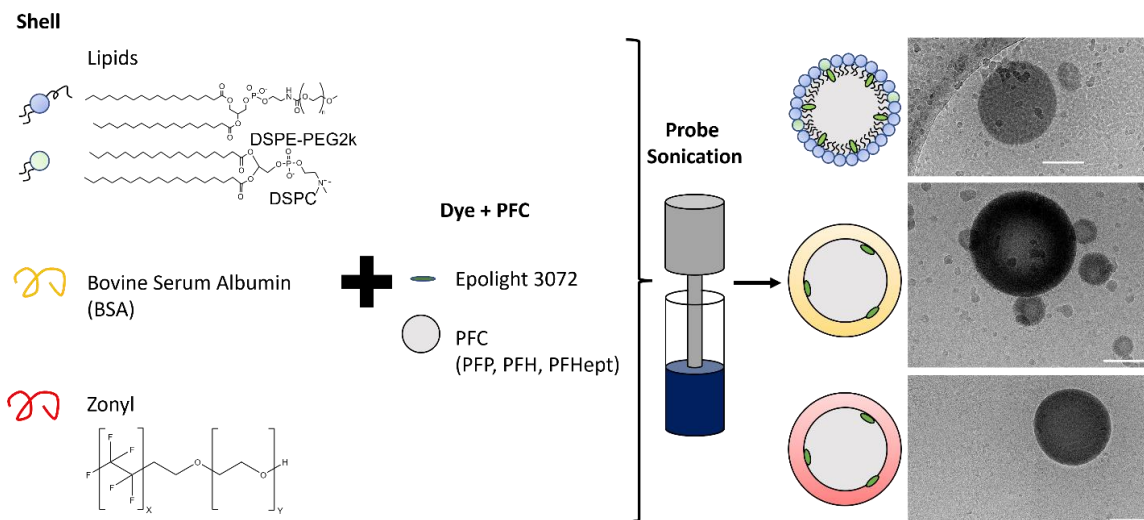


**Figure 1 – The schematic illustrates the different shell components and different perfluorocarbons (PFC) used in this study, along with cryo-TEM (cryogenic transmission electron microscopy) images taken of each shell formulation with perfluorohexane (PFH). The scale bar represents 100 nm.**

Lipid droplets were synthesized following methods previously described<sup>45</sup>. Briefly, DSPE-PEG 2000 (1,2-distearoyl-sn-glycero-3-phosphoethanolamine-N-[methoxy(polyethylene glycol)-2000]; Avanti Polar Lipids, Inc., Alabaster, AL, USA) and 18:0 PC (DSPC) (1,2-distearoyl-sn-glycero-3-phosphocholine; Avanti Polar Lipids, Inc., Alabaster, AL, USA) (9 DSPE-PEG 2000:1 DSPC by mass) in chloroform were mixed with 1 mg of dye Epolight 3072 (Epolin, Newark, NJ, USA). The chloroform was then evaporated using a rotary evaporator to form a lipid cake. Phosphate buffered saline (PBS, 2 mL) was added to the flask and bath sonicated to resuspend the lipid and dye. The solution was then transferred to an 8 mL glass vial, and perfluorocarbon liquid (100  $\mu$ L of perfluoropentane (PFP) and perfluorohexane (PFH) from FluoroMed (Round Rock, TX, USA) and perfluoroheptane (PFHept) from Sigma-Adlrich, St. Louis, MO, USA) was then added, and then probe sonicated (Q700, QSONICA, Newtown, CT, USA) in an ice bath at an amplitude of 1 (30 watts/cm<sup>2</sup>) for a processing time (total on time as defined by the

manufacturer) of 20 s with a pulse-ON time of 1 s and a pulse-OFF time of 5 s followed by a second sonication sequence at an amplitude of 50 (94 watts/cm<sup>2</sup>) for a processing time of 5 s with a pulse-ON time of 1 s and a pulse-OFF time of 10 s.

The nanodroplet solution was then centrifuged at 300 RCF for 2 min to separate out the sub-micron droplets from the larger droplets and unincorporated dye. The supernatant was then centrifuged at 3000 RCF to pellet all the nanodroplets and separate them from unincorporated lipids. The nanodroplets were then resuspended in 2 mL of PBS.

Zonyl droplets were synthesized by adapting methods described elsewhere <sup>34</sup>. Essentially, Epolight 3072 (1 mg, Epolin, Newark, NJ, USA) was mixed with 2 mL of 0.25% zonyl solution (Sigma-Aldrich, St. Louis, MO, USA). The solution was bath sonicated to ensure uniform distribution of the dye. Then, PFH (100  $\mu$ L) was added, and the solution was probe-sonicated in an ice bath using previously described settings. After sonication, the solution was centrifuged at 300 RCF for two minutes to remove unincorporated dye and large droplets, and then centrifuged at 3000 RCF to remove unincorporated surfactant and dye. Bovine serum albumin (BSA, Sigma-Adlrich, St. Louis, MO, USA) droplets were synthesized using similar methods, except the zonyl solution was replaced with a BSA solution (2 mL, 2 mg/mL) and 1 mg of Epolight 3072 <sup>46</sup>. The remaining protocol was the same as described above. Dynamic light scattering (DLS, Zetasizer Nano ZS, Malvern Panalytical, Malvern, UK) and nanoparticle tracking analysis (NTA, Nanosight NS300, Malvern Panalytical, Malvern, UK) were used to determine the size and concentration measurements. Nanodroplets were diluted based on concentration measurements to concentrations of  $5 \times 10^9$  nanodroplets/mL.

In order to characterize the nanodroplet size and concentration change over the laser pulse, the lipid, PFH, nanodroplets were diluted 200-fold and placed in a 96-well plate. Using a custom-built well plate lasing system, the nanodroplets were lased at  $75 \text{ mJ/cm}^2$  for various numbers of pulses. The samples were then diluted appropriately and characterized using nanoparticle tracking analysis.

The dye content for each different shell was characterized by freezing each sample overnight in a  $-80 \text{ }^\circ\text{C}$  freezer, followed by lyophilization (Labconco, Kansas City, MO, USA) for a day. The resulting powder was then resuspended in 1 mL of chloroform and bath sonicated for 5 min. The resulting solution was centrifuged at 3000 RCF for 5 min. The dye concentration in the supernatant was then quantified through UV-Vis spectroscopy (Evolution 220, ThermoFisher, Waltham, MA, USA) based on a standard.

### *3.2.2 Cryo-Transmission Electron Microscopy Sample Preparation and Data Acquisition*

Nanoparticle preparations were plunge frozen onto glow-discharged, 200 mesh copper Quantifoil grids (Quantifoil, Germany) in liquid ethane using a Vitrobot Mark IV (ThermoFisher, Hillsboro, OR, USA). Cryo-transmission electron microscopy (cryo-TEM) images were acquired in a 200 kV JEOL JEM-2200FS field emission TEM (JEOL Ltd., Tokyo, Japan) with a DE20 direct electron detector (Direct Electron LP, San Diego, CA, USA). Images were acquired with defoci of  $-4 \text{ } \mu\text{M}$  (40 kx magnification) and  $-2 \text{ } \mu\text{M}$  (20 kx magnification). The total dose per image ranged between 20 and 40 electrons/ $\text{\AA}^2$  at magnifications of 20 k (pixel size of  $2.852 \text{ } \text{\AA}/\text{pixel}$ ) and 40 k (pixel size of  $1.304 \text{ } \text{\AA}/\text{pixel}$ ).

### *3.2.3 Phantom Preparation and Imaging Setup*

Two polyacrylamide phantoms were constructed: one with a hollow tubular void (4.5 mm in diameter) and another with droplets embedded throughout (Figure 2). The tube phantom allowed for the nanodroplets to be suspended within water, while the polyacrylamide phantom had the nanodroplets within the polyacrylamide itself.

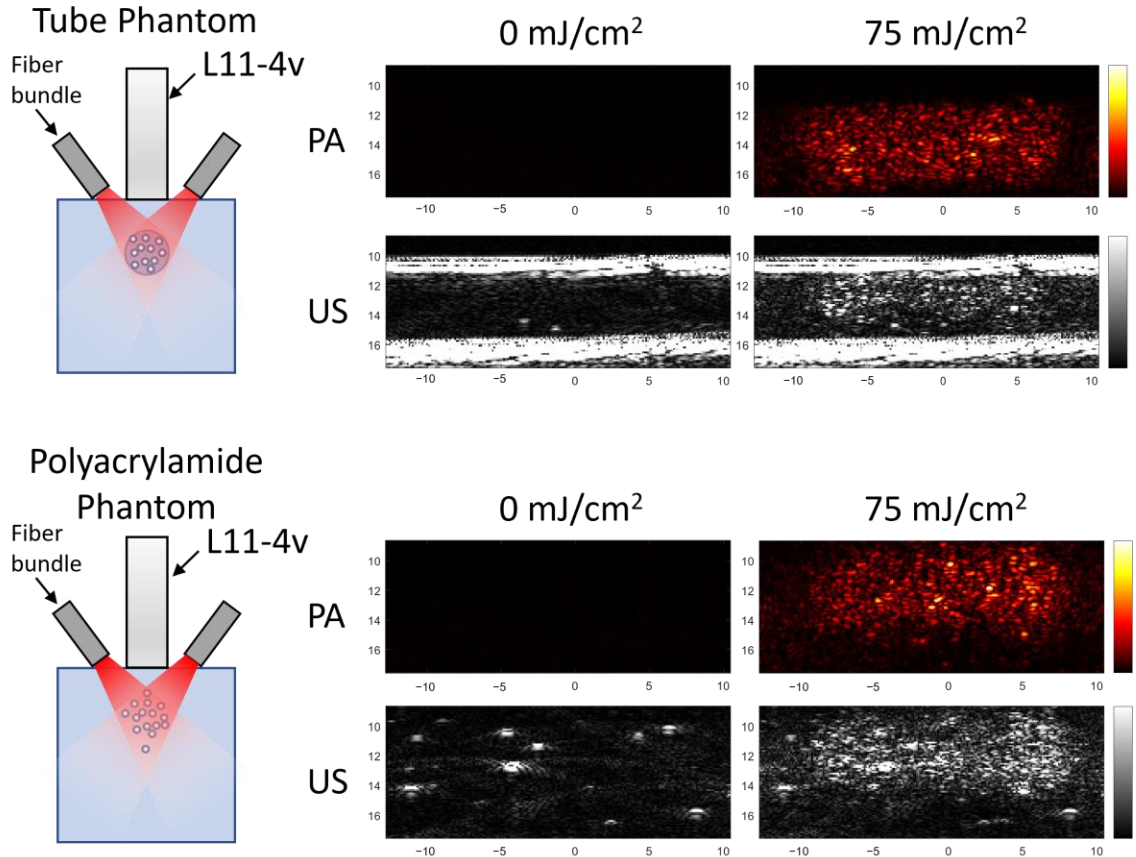


**Figure 2 – An illustration of the different phantoms with the corresponding ultrasound and photoacoustic images produced from each setup. Within the tube phantom, nanodroplets were suspended in water within the tubular void, while in the polyacrylamide phantom, the nanodroplets were embedded throughout the phantom.**

The transparent tissue-mimicking gel phantoms were synthesized by mixing 40% acrylamide (50 mL, Thermo Fisher Scientific, Waltham, MA, USA) with degassed water (150 mL). For the phantom with embedded droplets, nanodroplets were added to create a

final concentration of  $5 \times 10^9$  nanodroplets per mL. Afterwards, 10% (w/v) ammonium persulfate solution (2 mL, Sigma-Aldrich, St. Louis, MO, USA) and 250  $\mu$ L of TEMED (N,N,N',N'-Tetramethylethylenediamine, Sigma-Aldrich, St. Louis, MO, USA) were added to crosslink the acrylamide. The solution was then poured into a rectangular  $58 \times 58 \times 78$  mm mold and allowed to polymerize for 30 min. To create the hollow tubular void, a plastic transfer pipette was inserted into the polymerizing solution approximately 10 mm from the top. After polymerization, the pipette was removed. Nanodroplets were diluted and placed into the tube with ultrasound gel to seal up the ends.

The phantoms were imaged from the top using an ultrasound linear array transducer L11-4v (Verasonics Inc., Kirkland, WA, USA) integrated with a 3-D printed optical fiber bundle as described previously<sup>47</sup>. The ultrasound transducer was driven at a center frequency of 7 MHz using a programmable research ultrasound imaging system (Vantage 128<sup>TM</sup>, Verasonics, Kirkland, WA, USA). The transducer was acoustically coupled to the phantom with ultrasound gel, and the optical fiber bundle was connected to a pulsed laser system (Tempest 30, New Wave Research) operating at 1064 nm. The phantom was irradiated with 5 ns laser pulses at a pulse repetition frequency between 10 – 1 Hz, depending on the experiment. The output fluence was calculated based on energy measurements taken at the output of the fiber bundles using a laser power meter (Nova II, Ophir-Spiricon, North Logan, UT, USA). The nanodroplets were subjected to a pulse sequence of 10 pulses at  $75 \text{ mJ/cm}^2$  followed by a ramp-up in fluence, which was used to determine the threshold. The ramp-up set included one sham pulse ( $0 \text{ mJ/cm}^2$ ) followed by 3 pulses at each fluence, starting at  $10 \text{ mJ/cm}^2$  and ending at  $75 \text{ mJ/cm}^2$ , at intervals of approximately  $10 \text{ mJ/cm}^2$ . This sequence was repeated a total of 10 times. The initial 10

pulses were designed to “precondition” the nanodroplets for the first cycle and were later used to simulate imaging to determine if the threshold would change over the course of imaging. The ramp-up was utilized to determine the threshold. During this process, each laser pulse was followed by 1 photoacoustic frame, followed by 100 ultrasound image frames at a 2 kHz frame rate, of which the first 5 and last 5 were saved. Each measurement was performed on six separate planes, or samples, for each condition. To determine the decay behavior, the samples were lased for 300 pulses at  $75 \text{ mJ/cm}^2$ . Afterwards, the preconditioning pulses were removed, and the remaining points were fitted to an exponential decay function, from which the half-lives were determined. The phantoms were maintained at  $37 \text{ }^\circ\text{C}$  in a water bath, except for the shell experiments, which were conducted at room temperature, and the core experiments, which were performed at  $0 \text{ }^\circ\text{C}$ . This difference in temperature was due to the longer recondensation times of zonyl nanodroplets at physiological temperature as well as the non-recondensing behavior of PFP nanodroplets at room temperature. The temperature was decreased by surrounding the polyacrylamide phantom with ice for 15 min before imaging. For clarity purposes, the conditions for each experiment are described in Table 1.

**Table 1 Conditions used for each experiment in Chapter 3.**

<b>Experiment</b>	<b>Phantom Type</b>	<b>Core</b>	<b>Shell</b>	<b>Temperature (<math>^\circ\text{C}</math>)</b>	<b>Laser PRF (Hz)</b>
Preconditioning (Figure 2)	Tube	PFH	Lipid	37	10
PRF Variation (Figure 3)	Polyacrylamide	PFH	Lipid	37	1, 3, 6, 10

**Table 1 continued**

<b>Experiment</b>	<b>Phantom Type</b>	<b>Core</b>	<b>Shell</b>	<b>Temperature (°C)</b>	<b>Laser PRF (Hz)</b>
Shell Variation (Figure 4)	Tube	PFH	Lipid, BSA, Zonyl	RT <sup>1</sup>	10
Environment Variation (Figure 7)	Tube and Polyacrylamide	PFH	Lipid	37	10
Core Variation (Figure 9)	Polyacrylamide	PFP, PFH, PFHept	Lipid	0 <sup>2</sup>	10

<sup>1</sup> Shell variation was performed at room temperature because a significant portion of zonyl droplets did not recondense at physiological temperature. <sup>2</sup> Core variation was performed at 0 °C to allow for PFP to recondense.

### 3.2.4 Data Processing

Vaporization was confirmed based on ultrasound images collected after each laser pulse. Nanodroplets are generally recondensed before the fourth ultrasound frame. Differential ultrasound imaging was used to suppress the background signal and was performed by subtracting the last US frame from the first US frame after the laser pulse. Ultrasound intensity was determined by integrating over the region of interest. The vaporization threshold was determined by fitting the ultrasound intensity over the laser fluence plot with a sigmoid. Using the midpoint of the sigmoid and the slope at that point, a line was drawn, and the threshold was defined as the intersection of that line with the x axis. All data processing were performed with MATLAB. GraphPad Prism 8 (GraphPad, Boston, MA, USA) was used for plotting the figures and statistical analysis;  $p < 0.05$  was considered significant.

### 3.2.5 Surface Wave Elastography

In ultrasound elastography, shear modulus ( $G$ ) can be estimated from the measured shear wave speed ( $c_{sh}$ ) as:

$$G = c_{sh}^2 \rho \quad (5)$$

where  $\rho$  is the density of the tissue, and the relationship between Young's modulus ( $E$ ) and shear modulus is as follows:

$$E = 2G(1 + \sigma) \quad (6)$$

Poisson's ratios ( $\sigma$ ) for polyacrylamide was found to be 0.5,<sup>48</sup> therefore the equation can be simplified and combined with equation 1 to:

$$E = 3G = 3c_{sh}^2 \rho \quad (7)$$

Furthermore, as the polyacrylamide phantom lacks acoustic scattering, the propagation speed of surface Rayleigh waves ( $c_{sf}$ ) were utilized to measure the tissue elasticity. The ratio of shear wave speed to surface wave speed ( $c_{sh}/c_{sf}$ ) for viscoelastic materials with  $\sigma$  between 0.45 and 0.499 has been shown to be  $c_{sh}/c_{sf} = 1.05$ .<sup>49</sup> As a result, surface wave speed can be related to the Young's modulus by:

$$E = 3(1.05 c_{sh})^2 \rho \quad (8)$$

In this study, surface wave elastography was implemented using a Vantage 128 (Verasonics, Inc.) ultrasound imaging system equipped with a L22-14vLF linear array

transducer. Waves were excited at the surface of the phantom (Figure 8 A) by an acoustic radiation force impulse (15 MHz, 1500 cycles), and ultrafast plane wave imaging (15 MHz center frequency, 15.8 kHz frame rate, 3 compounding angles) was used for data acquisition. Axial displacement was estimated from the IQ data using the Loupas 2-D autocorrelator.<sup>50</sup> Surface waves were excited at 5 different pushing locations (Figure 8 C) and wave speeds determined based on a time-to-peak detection.

### 3.2.6 Photobleaching of Epolight 3072

Epolight 3072 was dissolved in DMSO at an OD of ~1 at 1064 nm. DMSO was chosen due to the fact that it is a non-volatile organic solvent to prevent changes in the absorption spectrum due to solvent evaporation. The solution (1 mL) was placed in a glass cuvette and lased at 90 mJ/cm<sup>2</sup> at a PRF of 10 Hz (Vibrant, Oportek) for 400 pulses. UV-vis spectroscopy was performed at 100 pulse intervals to characterize the changes in the absorption. The spectra were processed by applying a moving average filter with a window size of three to minimize noise. Epolight 3072 appears to be resilient to photobleaching up to at least 400 pulses at 90 mJ/cm<sup>2</sup>.

## 3.3 Results and Discussion

### 3.3.1 Preconditioning

During the course of this study, nanodroplets were observed to exhibit an initial quiescent phase during lasing in which limited US contrast was generated. After a few pulses, the nanodroplets would begin to vaporize regularly. To demonstrate this behavior, lipid, and PFH nanodroplets in water were imaged in the tube phantom and lased repeatedly

at  $75 \text{ mJ/cm}^2$ . The initial pulse exhibits some ultrasound contrast, which increases in subsequent pulses (Figure 3 A).

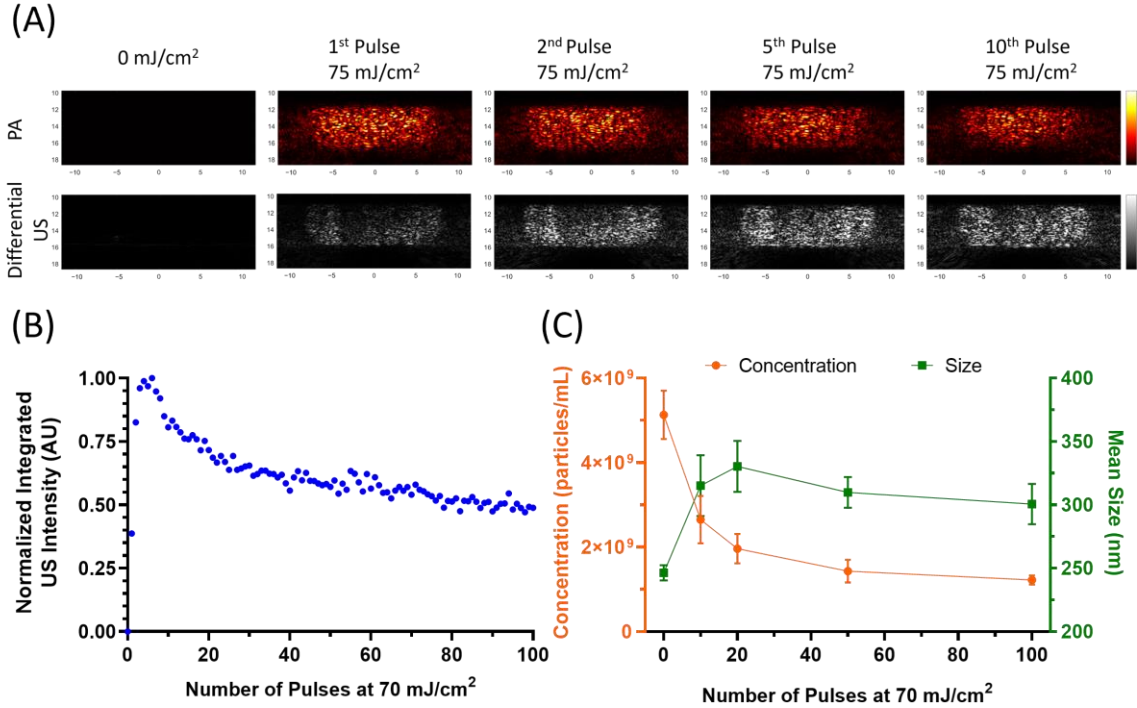


**Figure 3 – (A) Differential US and PA images of lipid, PFH, and nanodroplets within the tube phantom at different pulse numbers. (B) The normalized integrated US intensity of the same nanodroplets over the course of 100 pulses at  $75 \text{ mJ/cm}^2$ . (C) Mean size and concentration taken by the NTA over the course of the 100 pulses. Error bars represent standard errors.**

The increasing US contrast behavior is only observed within the first few pulses, and afterwards the nanodroplets exhibit a decrease in the integrated US intensity (Figure 3 B). Size measurements taken by NTA of the nanodroplets after exposure to varying numbers of laser pulses indicate an increase in the mean size and decrease in concentration after 10 pulses, which corresponds to the approximate end of the preconditioning phase and the start of the decay phase (Figure 3 C). This suggests that the initial lasing results in the destruction of smaller nanodroplets that may coalesce to form larger nanodroplets. Similar behavior has been observed optically in ADV studies on larger droplets, where the

resulting microbubble would increase in diameter after repeated cycles.<sup>39</sup> Such an occurrence would explain the sudden increase in US contrast within the initial pulses as the nanodroplets coalesce from laser perturbation. The subsequent decay is likely due to the more gradual destruction of the nanodroplets without as much coalescence, as evidenced by the decrease in concentration without a substantial change in the mean size.

This process could explain the absence of “preconditioning” behavior observed in a study by Namen et al., which utilized ADV for repeated vaporization of PFH nanodroplets<sup>51</sup>. In their study, a 10 cycle ultrasound pulse at 1.1 MHz was used to trigger the transient phase change. Nanodroplet coalescence most likely occurred during the initial cycles. Since the resulting microbubbles were only imaged after the activation pulse, no “preconditioning” behavior was observed. Moreover, it is important to note that in ADV, energy is deposited over a longer period of time. In the study by Namen et al., the pulse duration was nine microseconds, while this investigation employed the use of a five nanosecond pulsed laser. We theorize that the longer duration of the high intensity focused ultrasound (HIFU) exposure, along with its mechanical impact, facilitates the coalescence of the nanodroplets during the initial activation pulse. In the case of ODV, heat is deposited in a shorter period, likely requiring more pulses to achieve “preconditioning”.

Although this behavior may impose some limitations on imaging these particles in the body, there are straightforward methods to overcome them. One approach is to “precondition” the nanodroplets with several pulses prior to injection, ensuring ideal behavior in situ. However, this may change the size distribution and impact on trafficking of the nanodroplets. Alternatively, additional pulses can be incorporated into the imaging sequence that can allow for “preconditioning” in vivo without altering nanodroplet size

prior to injection. On a side note, this unique behavior could be leveraged to enhance nanodroplet identification in situ.

### 3.3.2 *PRF Variation*

Another possible contributor to the “preconditioning” behavior could be the buildup of heat over lasing. This could be explored by altering the laser PRF. By increasing the time between each laser pulse, there would be more time for heat to diffuse.

Previous work has shown that acquisition settings such as imaging pulse polarity can influence nanodroplet behavior, and HIFU along with laser irradiation can reduce the vaporization threshold<sup>26,52</sup>. To our knowledge, no studies have examined the impact of the laser itself. To test the impact of the laser PRF on the nanodroplet performance, PFH and lipid nanodroplets were embedded in a polyacrylamide phantom. This prevents the nanodroplets from diffusing in and out of the lasing plane, ensuring consistent exposure to the same population of nanodroplets. The impact of the polyacrylamide phantom is further discussed in a later section. In order to determine the vaporization threshold, a ramp cycle composed of three pulses at each fluence ranging from 0 to 75 mJ/cm<sup>2</sup> at intervals of approximately 10 mJ/cm<sup>2</sup> was used. These cycles were interleaved between sequences of 10 pulses at 75 mJ/cm<sup>2</sup>. This was done to initially precondition the nanodroplets and further simulate imaging of the nanodroplets to determine how the threshold changes over repeated lasing. Nanodroplets were lased at a variety of PRFs (1 Hz, 3 Hz, 6 Hz, and 10 Hz) and found to have a small impact on the vaporization threshold (Figure 4).

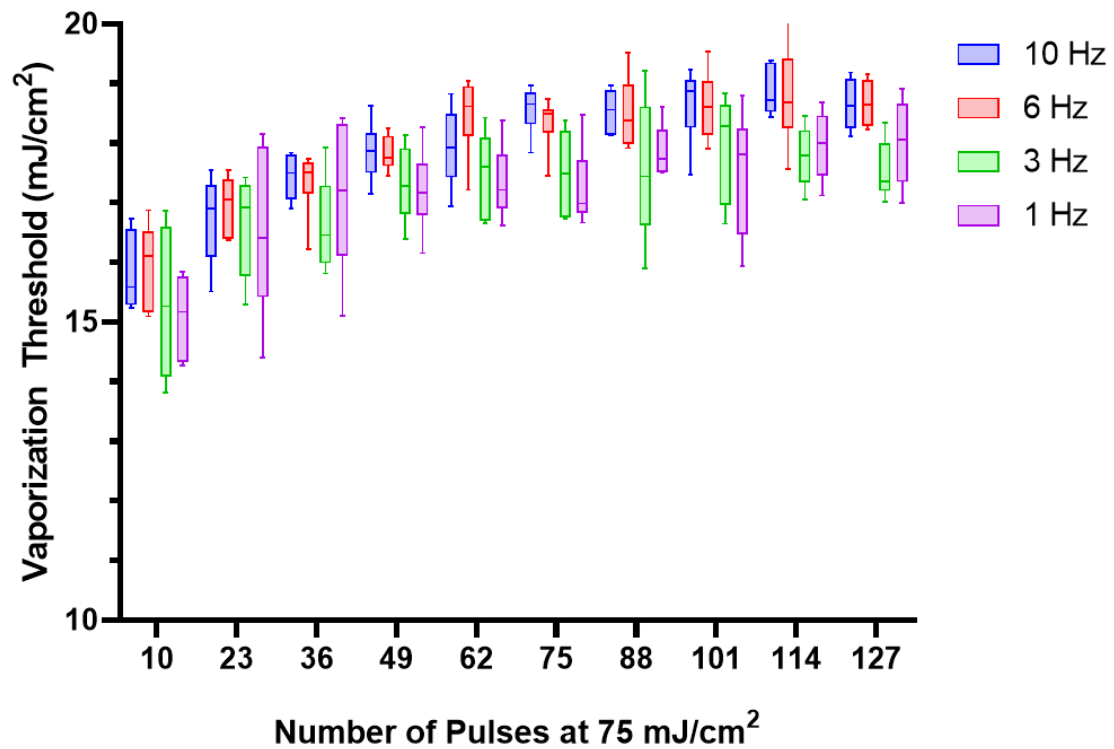


**Figure 4 – The vaporization threshold of lipid, PFH, nanodroplets (n = 6) embedded in a polyacrylamide phantom at different laser pulse repetition frequencies (PRF; 10 Hz, 6 Hz, 3 Hz, and 1 Hz). The different PRFs did exhibit a statistical difference (repeated measures ANOVA;  $F(3, 20) = 4.146, p = 0.0194$ ), with differences detected between 10 Hz and 3 Hz/1 Hz ( $p = 0.0014$  and  $p = 0.0029$ ) and 6 Hz and 3 Hz/1 Hz ( $p = 0.0005$  and  $p = 0.0012$ ). However, the mean differences were small ( $\sim 0.8 \text{ mJ/cm}^2$ ).**

This result suggests that, based on the PRFs used in this study, heat buildup is unlikely, as that would result in a reduced vaporization threshold for the nanodroplets lazed at higher PRFs. Oddly enough, the nanodroplets lazed at 10 Hz and 6 Hz exhibited a slightly elevated vaporization threshold ( $\sim 0.8 \text{ mJ/cm}^2$ ) in comparison to the 3 Hz and 1 Hz samples. The difference in vaporization threshold is relatively small and likely an artefact of the laser itself due to pulse-to-pulse variations at different PRFs, which can vary by 2.5%. These slight differences could contribute to the difference between the PRFs.

Studies examining PRF for ADV performed by Wu et al. and Fabiilli et al. showed that higher PRFs result in lower pressure thresholds for lipid-coated perfluorobutane nanodroplets<sup>39,40</sup>. However, these studies were performed in a flow environment, and increasing the PRF would increase the number of pulses to which a subpopulation of nanodroplets were exposed. Thus, it is not analogous to compare the impact of laser PRFs on ODV thresholds to the impact of ultrasound PRFs on ADV.

### 3.3.3 *Shell Variation*

Previous studies have used a variety of materials to stabilize droplets, but no work has been performed directly comparing shell compositions and their effect on ODV. Typically, droplets are synthesized with a lipid shell using DSPC-PEG, DSPE, or similar lipids. Others have used proteins such as bovine serum albumin (BSA), fluorosurfactants such as zonyl, krytox, or other polymers to stabilize the droplet.<sup>30,34,42,52-57</sup> In lipid nanodroplets, shell composition has been shown to impact the echogenicity and size of the droplets.<sup>45,58</sup> This would suggest that changing the shell composition could also impact the vaporization threshold and recondensation of the nanodroplets.

To examine this hypothesis, nanodroplets formulated with lipid, BSA, and zonyl, a fluorosurfactant, were characterized at the same concentration ( $5 \times 10^9$  nanodroplets/mL) in the tube phantom. The different formulations were of similar sizes (z-average size BSA: 314 nm, lipid: 293.6 nm, and zonyl: 285.8 nm). These experiments were performed at room temperature in water, as zonyl nanodroplets did not fully recondense at physiological temperature before the subsequent laser pulse.

The different formulations had a substantial impact on the vaporization threshold (Figure 5 A), with zonyl nanodroplets exhibiting the lowest vaporization threshold, followed by lipid and then BSA. However, each formulation contained different amounts of dye (Figure 5 B). Surprisingly, the dye content did not correlate with the vaporization threshold, with BSA having the most, followed by lipid, and then zonyl. This suggests that the shell has an impact on the vaporization threshold independently of the dye content.

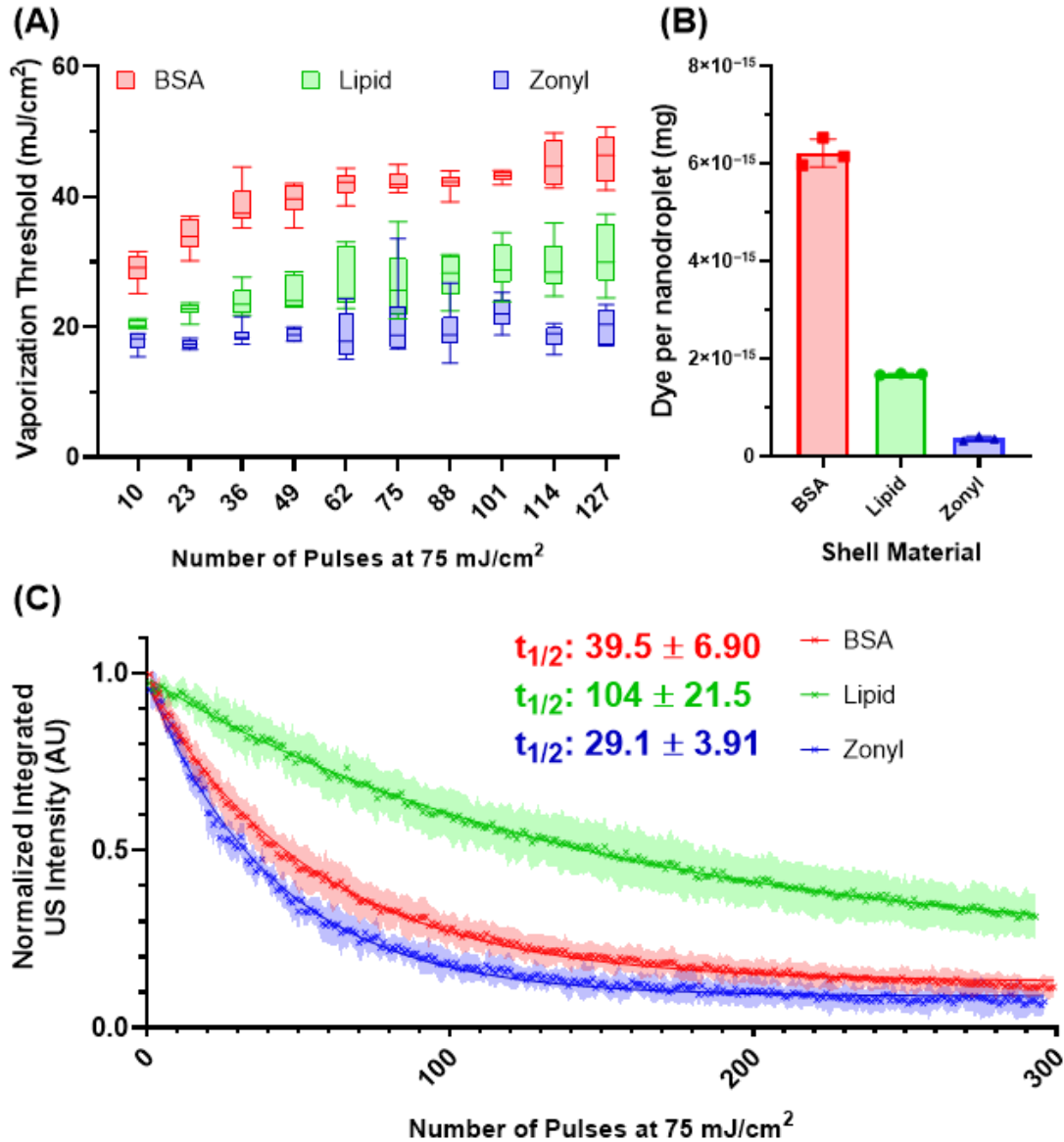


**Figure 5 – (A)** The vaporization threshold of the different formulations of the nanodroplets ( $n = 6$ ) after exposure to varying numbers of laser pulses ( $75 \text{ mJ/cm}^2$ ). Significant differences in the vaporization threshold were observed among the different shells ( $F(2, 15) = 172.3, p < 0.0001$ ). Tukey’s comparison test indicated significant differences between all shells ( $p < 0.0001$ ). **(B)** Dye content per formulation ( $n = 3$ ). Error bars represent the standard deviation. **(C)** The decay behavior of the normalized integrated US intensity for each formulation ( $n = 6$ ) after repeated lasing at  $75 \text{ mJ/cm}^2$ . The half-life for each formulation was determined by fitting each curve with an exponential decay.

The difference in vaporization thresholds could be due to the difference in the interfacial tension at the water/PFH interface. Lipid surfactants have been shown to have minimal interfacial tension between water and perfluorocarbons, with measurements at 1.14 dynes/cm and the interfacial tension between water and PFP stabilized by zonyl was found to be 5.8 dynes/cm<sup>59,60</sup>. The interfacial tension of BSA has been reported to be ~30 dynes/cm, which is much higher than that of lipids and zonyl.<sup>61</sup> This would result in BSA exhibiting a Laplace pressure of 400 kPa, compared to 15.2 kPa and 77.3 kPa for lipids and zonyl, respectively. Approximating the boiling temperature utilizing the Antoine equation<sup>62,63</sup> results in a boiling temperature of 132.85 °C, 61.9 °C, and 77.65 °C for BSA, lipid, and zonyl, respectively. While these differences do appear to somewhat agree with the vaporization thresholds, the dye loading values suggest that the threshold for BSA should be far greater, and like for ADV, Laplace pressure alone is unlikely to predict the vaporization threshold for ODV.<sup>20</sup>

Another factor that could influence the vaporization threshold could be the intermolecular forces between the surfactants. A study performed by Mountford et al. demonstrated that increasing acyl chain length increased the activation energy required for ADV,<sup>64</sup> and Huang et al. showed that crosslinking polymers on the surface of the perfluorocarbon nanodroplet increased the ADV threshold compared to uncrosslinked polymers.<sup>65</sup> Since BSA microbubbles are stabilized by cross-linked cysteine residues found on the proteins formed due to cavitation during the sonication process,<sup>66</sup> this suggests that higher vaporization thresholds for BSA nanodroplets could be due to crosslinking of the BSA proteins. Moreover, fluoroalkanes have weaker intermolecular forces in comparison to their hydrocarbon cousins.<sup>67</sup> This could explain the difference in the vaporization

thresholds between zonyl and lipid nanodroplets, as the hydrophobic tails of the lipids have a higher activation energy compared to the fluorinated segment of the fluorosurfactants.

In order to better isolate the impact of the shell, future studies should conjugate the photoabsorber onto the surface of different shells at known ratios such that concentrations will be uniform between samples.

Following repeated lasing at  $75 \text{ mJ/cm}^2$ , all the formulations exhibited a decay in US contrast (Figure 5 C). This decay is unlikely to be driven by photobleaching of the dye, as Epolight 3072 appears to be stable past 400 pulses at  $90 \text{ mJ/cm}^2$ , showing little change in the UV-Vis spectrum (Figure 6). This suggests that the decrease in US contrast is primarily driven by nanodroplet destruction or ejection of the dye.

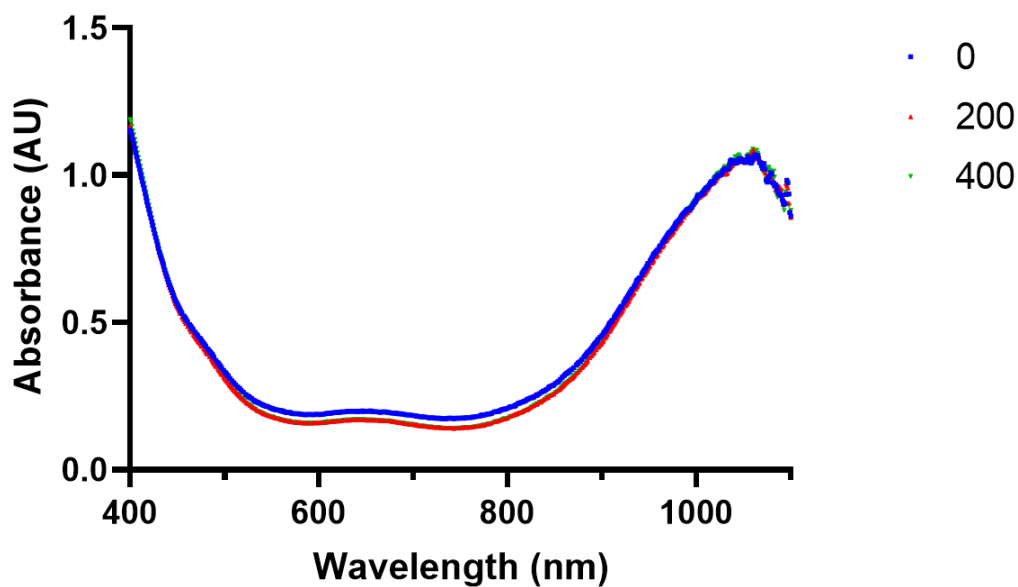


**Figure 6 – UV-vis spectra comparison of Epolight 3072 in DMSO before and after being lased at 1064 nm at  $90 \text{ mJ/cm}^2$  for 0, 200, and 400 pulses.**

Lipid nanodroplets exhibited the longest half-life (100 pulses) in comparison to BSA and zonyl, which had half-lives of 39.5 and 29.1 pulses, respectively. The longevity of the nanodroplets may be related to the flexibility of their shells. Lipid microbubbles exhibit more flexibility in their shell compared to the more rigid BSA, which may explain the ability of these nanodroplets to undergo repeated vaporization events.<sup>68</sup> However, there are few studies that examine the shell behavior of fluorosurfactants, limiting any further comparisons.

After vaporization, the distribution of the surfactants could also influence the nanodroplet's performance. A comparison between nanodroplets formulated from fluorescently tagged lipids and BSA showed that the lipids were homogeneously distributed after vaporization, while the BSA bubble exhibited a heterogeneous coating. Furthermore, lipid nanodroplets exhibited slower expansion post-vaporization in comparison to BSA and fluorosurfactant-stabilized nanodroplets, suggesting that lipids were better retained and limited gas transfer.<sup>56</sup> These factors could limit the fragmentation of the shell, loss of dye, and diffusion of PFH out of the nanodroplet, resulting in more sustainable vaporizations.

#### *3.3.4 Environmental Variation*

To determine the impact of the local environment on the nanodroplet vaporization, lipid nanodroplets were embedded in polyacrylamide and compared to those suspended in water within the tube phantom at the same concentration ( $5 \times 10^9$  nanodroplets/mL). The vaporization thresholds were initially similar (Figure 7 A), but they quickly diverged. The

initial similarity suggests that embedding the nanodroplets within the phantom had minimal impact on the nanodroplet vaporization.

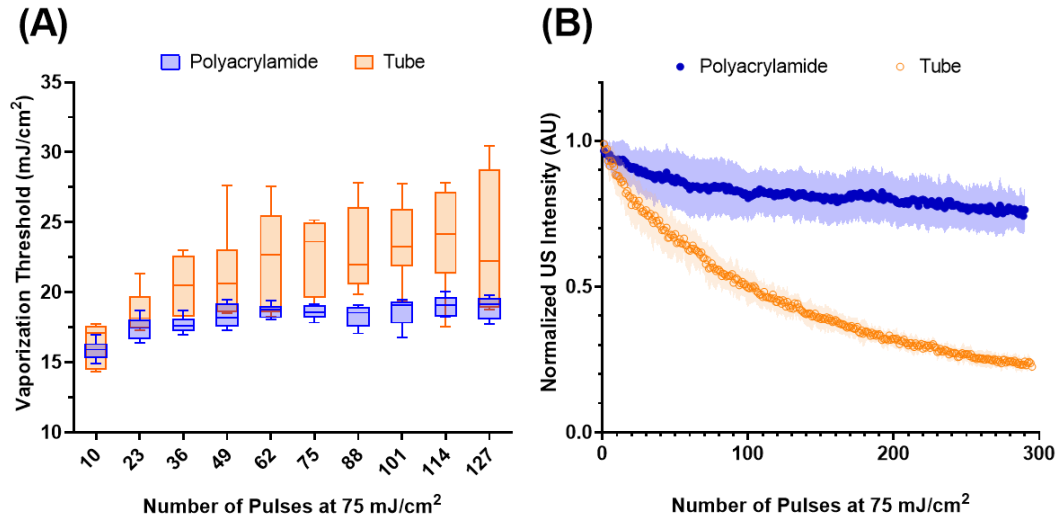


**Figure 7 – (A) The vaporization threshold of lipid, PFH, nanodroplets (n = 6) embedded in a polyacrylamide phantom compared to those within the tube phantom over repeated lasing at 75 mJ/cm<sup>2</sup>. The environments exhibited a statistically significant difference (paired *t*-test, *p* < 0.0001). (B) The decay behavior of the normalized integrated US intensity for each environment (n = 6) after repeated lasing (75 mJ/cm<sup>2</sup>).**

Further lasing leads to an increase in the average and standard deviation of the threshold of the nanodroplets in water, whereas in the phantom, the increase is more gradual with smaller standard deviations. This observation suggests that nanodroplets with lower vaporization thresholds were destroyed in water, while the phantom environment likely mitigated nanodroplet destruction. This is supported by (Figure 7 B), where the nanodroplets are lased repeatedly at 75 mJ/cm<sup>2</sup> and demonstrate a limited decrease in US contrast in comparison to nanodroplets in water.

Microbubble behavior is known to be impacted by the surrounding environment, where fragmentation of microbubbles is reduced in more viscous fluids.<sup>69</sup> Thus, it is likely

that the viscoelastic properties of the polyacrylamide phantom help stabilize the vaporization of the nanodroplets, reducing their destruction.

Furthermore, it was observed that repeated vaporization of PFH nanodroplets in the phantom resulted in the formation of residual microbubbles that did not recondense within the duration of the imaging sequence. This behavior has also been observed in repeated ADV of lipid PFH nanodroplets.<sup>51</sup> The nanodroplets likely coalesced together during the repeated vaporization, eventually forming stable microbubbles. A similar behavior has been described with ADV of PFP nanodroplets, where repeated vaporization is needed to result in the formation of stable microbubbles.<sup>70</sup> Meanwhile, nanodroplets in water did not exhibit this behavior.

These observations have implications for characterizing nanodroplet behavior. Nanodroplet behavior is commonly studied within phantoms such as polyacrylamide or agarose. While this does allow for observation of individual nanodroplet dynamics without movement of the particles, it's clear that the phantom could help stabilize the nanodroplets and resulting microbubbles, and the impact of the phantom should be considered.

Surface wave elastography was used to measure the stiffness of the polyacrylamide phantom, which was found to have a Young's modulus of  $100 \pm 3.11$  kPa (Figure 8). This is notably higher than most tissues within the human body,<sup>71</sup> suggesting that nanodroplet vaporization is unlikely to be suppressed due to the stiffness of the surrounding tissue. This observation holds implications for applications where the nanodroplets are embedded in tissue, bound to a cancer cell,<sup>72</sup> or taken up by macrophages.<sup>73-75</sup>

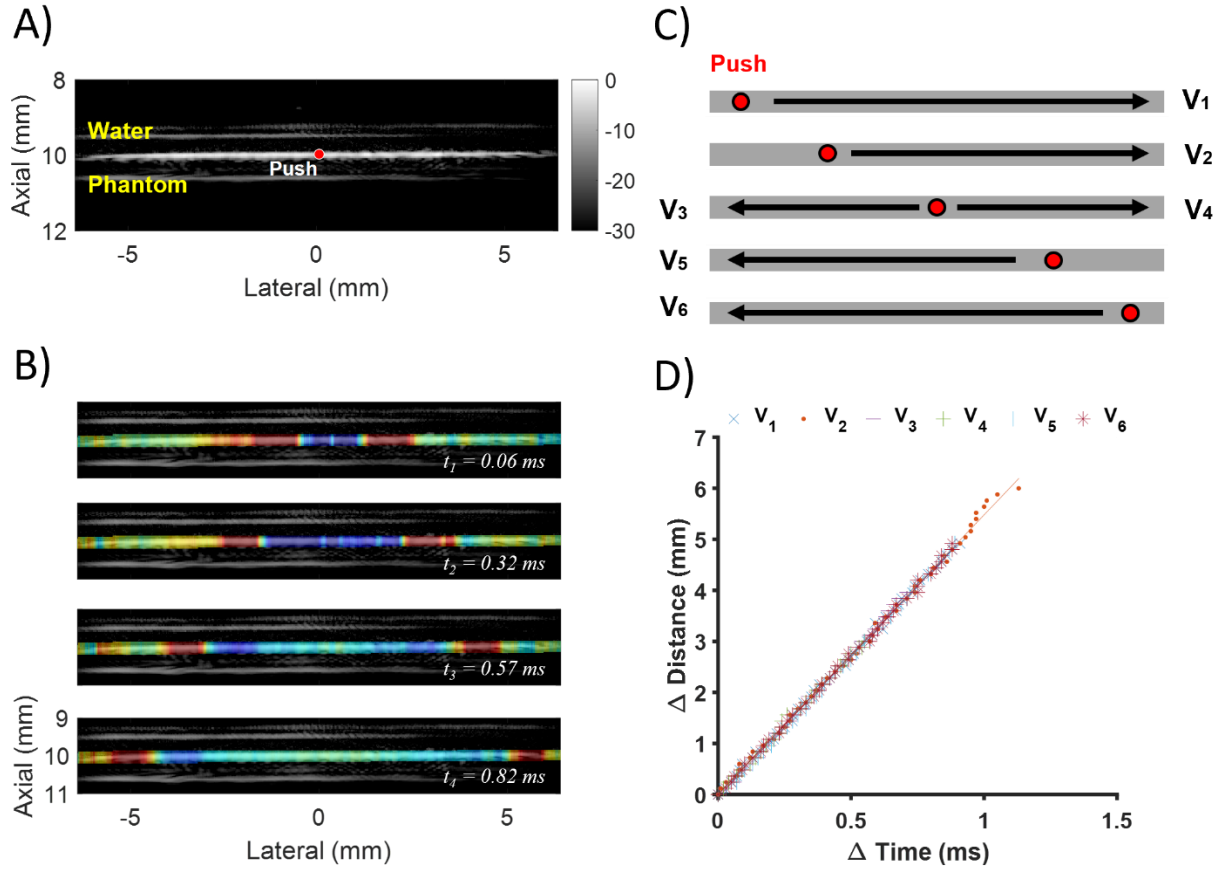


**Figure 8 – A) Ultrasound image of the interface between the phantom and the water along with the push location. B) The interface overlaid with multiple frames of the calculated axial displacement, depicting the propagation of surface waves over time. C) A schematic illustrating the push locations and the direction of wave speed measurement from each push. D) Wave speeds were calculated by a linear fit of the distance traveled by the peak of the wave over time. The surface wave speed in the polyacrylamide phantom was determined to be  $5.51 \pm 0.09$  m/s and the Young’s modulus was calculated to be  $100.26 \pm 3.11$  kPa.**

However, the mean peak ultrasound intensity showed a 46% reduction in the polyacrylamide in comparison to the tube phantom. This could be due to two main factors: destruction of nanodroplets during polymerization and suppression of microbubble expansion. The polyacrylamide polymerization process is exothermic, which could result in the destruction of the nanodroplets through spontaneous vaporization from heating. Microbubbles can sometimes be visualized before the lasing of the phantom (Figure 1).

Furthermore, the polyacrylamide phantom itself can restrict the expansion of the microbubble.

Repeated lasing of the phantom was not observed to impact the polyacrylamide phantom. Photodegradation of hydrogels primarily occurs through the process of plasma generation at the site of lasing, which results in the formation of bubbles that cavitate.<sup>76</sup> While the nanodroplets embedded in the phantom undergo a similar process, these particles occupy a small volume fraction of the phantom (~0.004%), and no damage was observed visually or in the ultrasound images.

### 3.3.5 Core Variation

Previous work has shown that ADV thresholds heavily depend on the boiling temperature of the core.<sup>18,77</sup> However, it is unclear how transitory ODV thresholds of sub-micron-sized nanodroplets depend on boiling temperature, as previous work utilized micron sized droplets, validated vaporization optically, or only characterized one core material.<sup>31,42,52</sup>

To this end, lipid nanodroplets were synthesized with PFP, PFH, and PFHept with z-averaged sizes of 309.0 nm, 293.6 nm, and 265.1 nm, respectively. These nanodroplets were then embedded within polyacrylamide phantoms to ensure more precise measurements of the vaporization threshold. The phantoms were chilled to 0 °C to allow for repeated vaporization of PFP. The vaporization thresholds show variations based on the core material (Figure 9 A). The average vaporization thresholds of the nanodroplets were plotted against the critical temperature of their respective cores and fitted with a linear regression, assuming vaporization occurred via homogeneous nucleation, with an x-

intercept at 0 °C (Figure 9 B). This suggests that ODV thresholds are correlated to the critical temperature, and deviations could be due to minor variations in concentration, size, or pulse-to-pulse variation in laser fluence. However, application of classical homogeneous nucleation theory may not present the most accurate depiction of ODV as it does not account for interfacial tension, which our results suggest can impact the threshold (Figure 5 A) and the photoacoustic pressure generated from the dye itself. Overall, the observed behavior follows trends observed in ADV<sup>39,41</sup> and previous observations performed by Dove et al.<sup>31</sup>

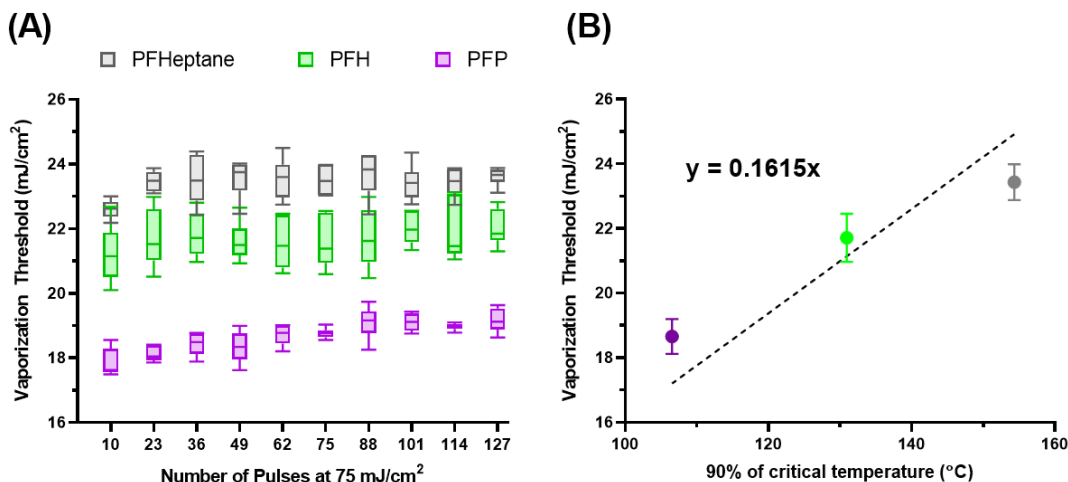


**Figure 9 – (A) The vaporization thresholds of lipid nanodroplets with different cores embedded in a polyacrylamide phantom that has been cooled to 0 °C. (B) The averaged vaporization thresholds for each core are plotted against 90% of the critical temperature for each core and fitted with a linear fit with an x-intercept set to 0 °C. Error bars represent the standard deviation of n = 6 replicates.**

The observed difference in transient vaporization thresholds is substantially lower than that previously reported in optical vaporization measurements.<sup>22,31,52</sup> Previous work noted substantial differences between the thresholds of PFP and PFH. This implies that the vaporization threshold could depend on the formulation of the particle. Dove et al.

formulated perfluorobutane (boiling point:  $-1.7\text{ }^{\circ}\text{C}$ ) droplets with gold nanoparticles conjugated onto the lipid shell and found the vaporization threshold to be  $26.1 \pm 21.7\text{ mJ/cm}^2$ , which is similar to the vaporization threshold for the lipid PFH (boiling point:  $56\text{ }^{\circ}\text{C}$ ) nanodroplets in our study. Though not directly comparable due to different absorbers and cores, this result suggests that embedding the optical absorber within the droplet shell allows for higher efficiencies of energy transfer that result in lower vaporization thresholds. Surface conjugation can result in lower amounts of absorber per droplet due to steric hinderance and limited binding sites, while encapsulation within the lipid membrane can lead to the incorporation of greater amounts of dye and higher heat transfer efficiencies compared to surface-bound nanoparticles. This is further supported by work done by Wei et al., where gold nanospheres coated with hydrophobic and hydrophilic ligands were used to create the shell, resulting in vaporization thresholds as low as  $3.5\text{ mJ/cm}^2$  for PFH nanodroplets.<sup>78</sup>

In this study, several factors that impact the vaporization threshold have been identified; however, to fully understand the underlying mechanisms of ODV, other factors that impact Laplace pressure should be examined, such as nanodroplet size. Future studies can utilize microfluidic devices to either sort or synthesize monodisperse nanodroplets to systematically examine the impact of size on nanodroplet vaporization, which would help elucidate the interplay between Laplace pressure and ODV.

### **3.4 Conclusions**

Overall, this study has investigated the dynamics of repeated vaporization of high boiling point PFCs and identified a short phase in which the nanodroplets exhibit increased

US contrast, which we term “preconditioning”. This process is likely due to a change in the size of the nanodroplet and not to the buildup of residual heat. We further examined the relationship between ODV thresholds and different shell materials, environments, and perfluorocarbon cores. Nanodroplet shells are shown to have an impact on both the vaporization threshold and imaging half-life. ODV is shown to not be impacted by environmental stiffness, and the vaporization threshold of high-boiling-point perfluorocarbons correlates with the critical temperature. Overall, this work provides a foundation for future engineering of ODV nanodroplets and a starting point for exploring other properties of the nanodroplet, such as the “preconditioning” behavior and the development of a theoretical model for ODV. These advances could lead to improved use of these contrast agents for photoacoustic and ultrasound imaging and image-guided therapy.

### **3.5 Acknowledgements**

The Cryo-EM study was supported by the Robert P. Apkarian Integrated Electron Microscopy Core (IEMC) at Emory University, which is subsidized by the School of Medicine and Emory College of Arts and Sciences. Additional support was provided by the Georgia Clinical & Translational Science Alliance of the National Institutes of Health under award number UL1TR000454. Transmission electron micrographs were collected on the JEOL JEM-2200FS 200kV TEM supported by the National Science Foundation Major Research Instrumentation Grant 0923395.

# CHAPTER 4. LASER INDUCED SONOPORATION USING PFCNDS

## 4.1 Introduction

The cell membrane presents a major barrier for regulating entry of molecules into and out of the cell. While evolutionarily, this has served as a boon by preventing foreign biologics or toxic molecules from entering, it does present a double-edged sword for the delivery of therapeutics such as gene therapies or other nucleotide-based therapeutics such as mRNA or shRNA.

One approach for cytoplasmic delivery has been to utilize microbubble in tandem with US to induced cavitation to create small pores within the cell membrane to allow the entry of external molecules.<sup>16</sup> However, this approach is limited primarily to in vitro and vascular applications as the large size of the microbubbles prevent extravasation out of the vasculature.

Perfluorocarbon nanodroplets (PFCnDs) have been developed to overcome this limitation by utilizing external triggers such as ultrasound or light to initiate a phase change. However, instead of just utilizing PFCnDs to form microbubbles in situ, previous work has shown that optically triggerable PFCnDs were capable of opening the tight junctions that make up the blood brain barrier (BBB) through repeated ODV. This process allowed for the entry of dye molecules, evan's blue, into the brain.<sup>34</sup> The application of the vaporization process have been further explored in the context of sonoporation with one study utilizing both acoustic and optical stimuli to sonoporate cells.<sup>79,80</sup>

However, for many of those studies, the cells were exposed to the nanodroplets in suspension, which may not mimic the in vivo environment. Furthermore, it is unclear what the ideal conditions for laser-mediated sonoporation through PFCnDs is.

In this study, the conditions required for laser induced sonoporation are explored by varying the dye used in the PFCnDs, concentration of the particles, fluences, pulse numbers, types of cells, and the size of particles that can enter the cells.

## **4.2 Materials and Methods**

### *4.2.1 PFHnD Synthesis and Characterization*

Epolight PFHnDs were synthesized as described previously in 3.2.1. IR 1048 PFHnDs were synthesized in the same manner except that IR1048 dye (Sigma-Aldrich, Burlington, MA, USA; 1 mg) was utilized instead of Epolight 3072. Size and concentration were characterized by DLS and NTA respectively.

### *4.2.2 Cell Culture*

Human adipose-derived mesenchymal stem cells (HADMSC) were cultured in minimum essential medium (MEM) alpha medium (Corning, NY, USA) supplemented with 10% fetal bovine serum albumin (FBS) and 1% penicillin-streptomycin (P/S). Cells were seeded on 35 mm glass bottom dishes (81218, ibidi, Gräfelfing, Germany) at 75,000 cells per dish.

HeLa and HEK 293T cells were cultured in DMEM with high glucose, supplemented with 10% FBS and 1% P/S. These cells were seeded at 500,000 and 250,000

per dish respectively. 4T1 cells were cultured in RPMI-1600 that was supplemented with 10% FBS and 1% P/S. These cells were seeded at 250,000 per dish.

#### *4.2.3 Sonoporation and Data Processing*

Variable amount of PFHnDs were added at each dish depending on the condition along with calcein (1mL of 0.5 mg/mL, filtered with a 0.2 um filter, Cayman chemical, Michigan, USA). The dishes were then lased at 1064 nm (Vibrant, Opotek Inc, CA, USA) at varying fluence and number of pulses depending on the experiment. Afterwards, the media was removed, and the dishes were washed with Hanks buffered salt solution (HBSS) three times to remove excess calcein. The cells were then stained with Hoechst 33342 (Thermo Fisher Scientific) and Calcein Red-Orange, AM (ThermoFisher Scientific). Each dish was then imaged using the Cytation 7 (BioTek, Winooski, VT, USA). Images at 4x magnification were taken of the lased region, which was identified through calcein fluorescence, and processed to remove the background utilizing rolling ball at the default settings. The images were then stitched by using calcein red-orange as the registration channel. Individual cells were identified based upon the nuclei stain using the automatic setting. The nuclei stain then used as a mask to quantify mean fluorescence of each cell for calcein and calcein red-orange. The threshold for calcein was determined by drawing four lines that intersected the lased area and determining the background intensity from the fluorescence signal over the line. These values were averaged together and then multiplied by 1.5 to determine the threshold for sonoporation. The background intensity for calcein orange was determined by drawing a line over 4 different individual cells and averaging the background intensity, which was also multiplied by 1.5 to determine the threshold for a live cell. Analysis was restricted to a circular region of interest (ROI), which was the

approximate size of the beam (7 mm in diameter), that was centered around the calcein fluorescence. For samples in which the no sonoporation was apparent, an arbitrary region was chosen. Each ROI was composed of 3000- 8000 cells, however there was wide variation in the cell number in an ROI as the geometry of the dish promoted cell accumulation in the center. An example is visualized in Appendix B (Figure 31). Furthermore, as the dishes were manually lased there were slight variation in the location of lasing.

#### 4.2.4 *Size Variation*

To examine the size of particles that could enter into the cells through sonoporation, fluorescein isothiocyanate-dextran beads (average mw: 3000-5000; Sigma-Aldrich) were dissolved in PBS at a concentration of 25 mg/mL. This solution (1 mL) was incubated with HADMSCs cultured in a glass bottom dish along with PFHnDs ( $3 \times 10^{10}$  particles/mL). The dish was lased at  $60 \text{ mJ/cm}^2$  for 300 pulses.

#### 4.2.5 *MTT Assay*

Long term viability was quantified through an MTT assay. HADMSCs were seeded at 10,000 cells per well in a 96 well plate. PFHnDs were added to the cells on the following day to form a concentration of  $3 \times 10^{10}$  particles per mL. Select wells were lased for 100 pulses at fluences varying from  $30 \text{ mJ/cm}^2$  to  $90 \text{ mJ/cm}^2$ . MTT (5 mg/mL in PBS, 20  $\mu\text{L}$ ) was added to each well and allowed to incubate for 3.5 hours. Afterwards, the supernatant was removed, and the crystals were dissolved in DMSO (150  $\mu\text{L}$ ). To remove the influence of excess nanodroplets, the DMSO solution was allowed to settle and then the supernatant

of each well (100  $\mu$ L) was transferred to another well and the absorbance was measured at 590 nm utilizing a microplate reader (Synergy HT, BioTek, Winooski, VT, USA).

### 4.3 Results

Sonoporation was characterized by seeding cells on a glass dish, which allows for multiple washing steps with minimal cell loss while retaining spatial information (Figure 10).

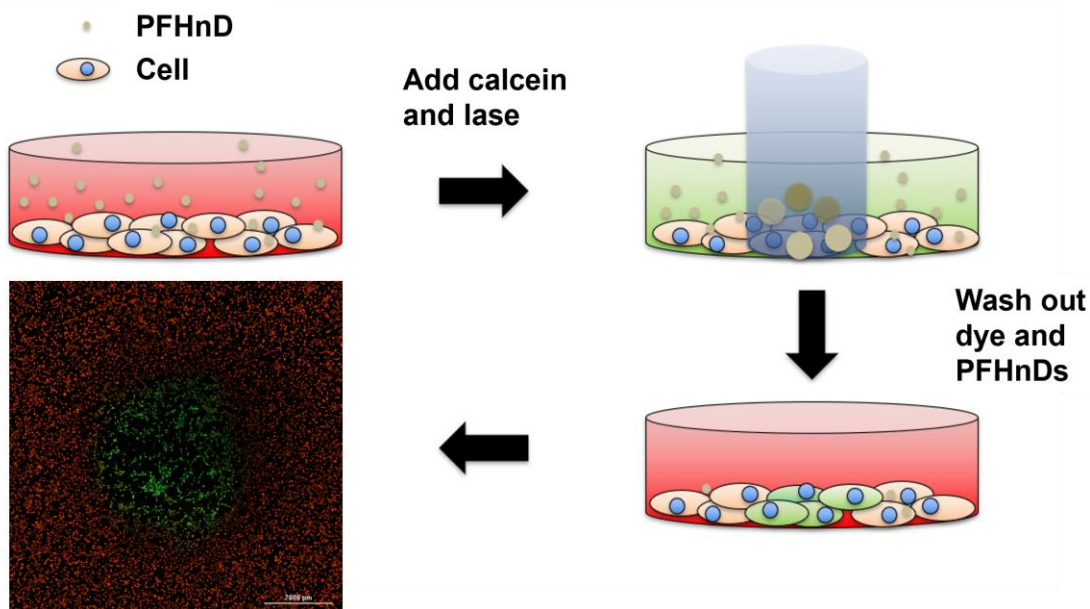


**Figure 10 – Schematic illustrating the process in which sonoporation is studied. PFHnD are added to cells with calcein (green) acting as a model drug and then the cells are lased. The excess calcein and droplets are washed out and the cells are stained with a nuclei stain (Hoechst 33342) and a live stain (calcein red-orange AM).**

Calcein was added to the media as an indicator for sonoporation. Typically, cells exclude the dye and successful sonoporation creates pores within the membrane that allow the calcein to traffic into the cytoplasm. After addition of nanodroplets and lasing, the dishes were washed three times with HBSS to remove excess calcein, and the cells were stained

with Hoechst 33342 and calcein red-orange am to allow for counting of cells and quantifying viability. Using the signal from Hoechst 33342 as a mask, successful sonoporation was defined by the presence of calcein within the cells, and the viability was quantified in a similar manner with calcein red-orange. This setup allowed for the examination of multiple variables that could impact successful sonoporation and viability of the cells.

#### *4.3.1 Dye*

The impact of the dye utilized in the nanodroplets was examined first. Two near infrared (NIR) dyes were selected: Epolight 3072 and IR 1048. Both possess absorbance peaks near 1064 nm (Figure 11 A), which falls into the second optical window where there is minimal attenuation from blood, fat, and skin.<sup>4</sup> The resulting nanodroplets exhibit similar size (Epolight 3072:  $333.5 \pm 4.8$  nm, IR1048:  $335.7 \pm 1.4$  nm; Figure 11 B). However, the IR 1048 PFCnDs are able to sonoporate a substantially greater portion of the cells (Figure 11 C, 42.5% vs 16.1%, un-paired t test  $p = 0.025 < 0.05$ ) with minimal difference in the amount of calcein delivered and minor impact on the viability (Figure 11 D).

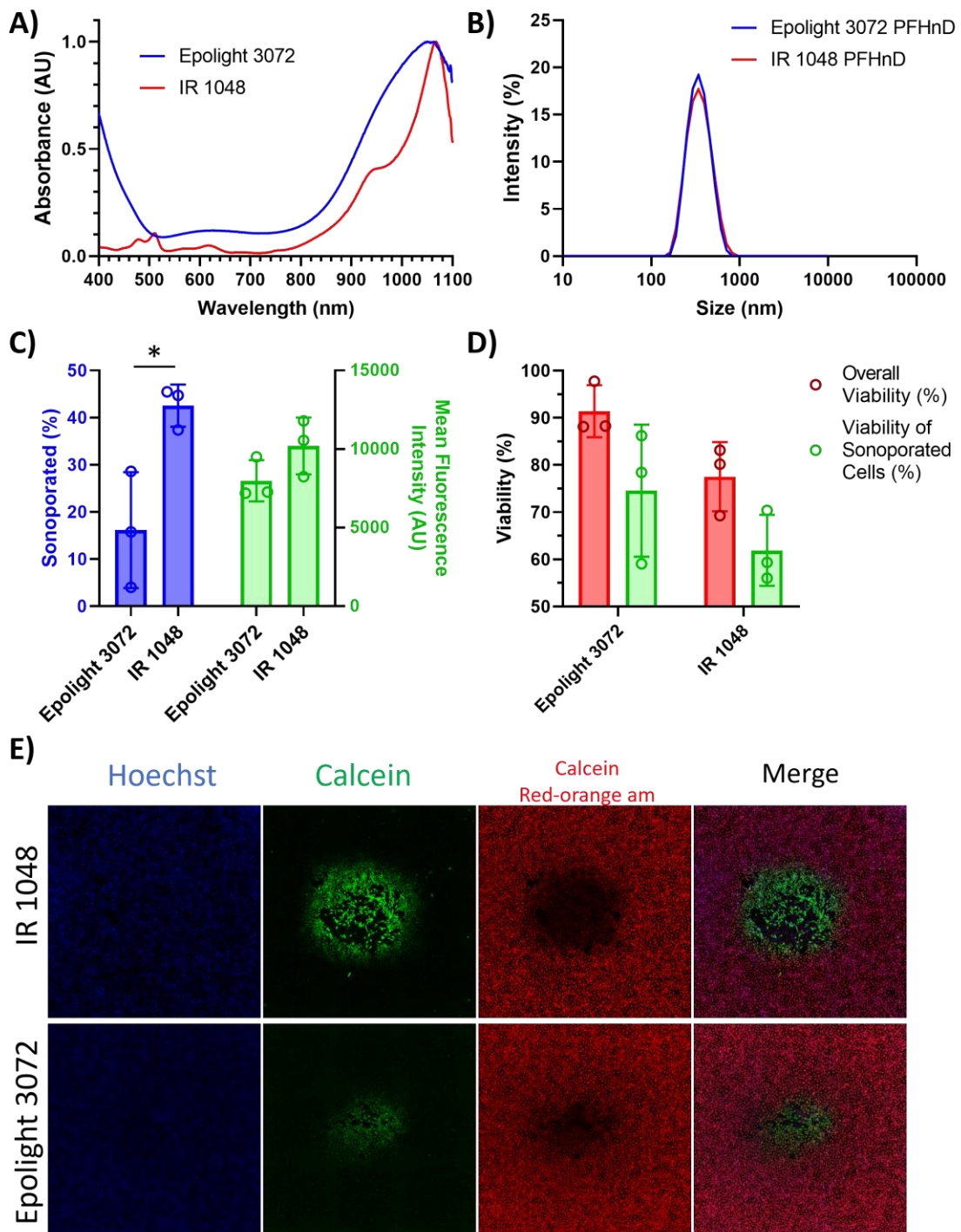


**Figure 11 – A)** The absorbance spectrum of Epolight 3072 and IR1048. **B)** The DLS size measurement of the resulting PFHnDs synthesized with different dyes averaged from  $n = 3$  measurements. Z-average of Epolight 3072 and IR1048 were  $333.5 \pm 4.8$  nm and  $335.7 \pm 1.4$  nm respectively. **C)** The sonoporation rate and the mean fluorescence intensity of successfully sonoporated cells for each formulation of

**PFHnD lased at 100 pulses at 60 mJ/cm<sup>2</sup>. The sonoporation rates of IR1048 and Epolight 3072 exhibit statistically significant differences (un-paired t-test, p=0.025 <0.05. D) The viability assessed through fluorescence of calcein red-orange of the cell population in the ROI and specifically the sonoporated cells as a function of concentration. C) and D) are the summation of n = 3 replicates with approximately 3000-8000 cells within the ROI. E) Representative images of the lased cells.**

For ODV, the dye plays a major role in the vaporization of the PFHnDs. While IR 1048 PFCnDs exhibit a higher vaporization threshold (~25 mJ/cm<sup>2</sup> vs 20 mJ/cm<sup>2</sup>), the fluences used in the study far exceed those values (60 mJ/cm<sup>2</sup>), thus both PFCnDs likely exhibit vaporization to similar extents. However, the delivery efficiencies were quite different. Epolight 3072 exhibited wild variations in the delivery rates, while IR1048 exhibited a higher sonoporation efficiency with a smaller variance. All samples are shown in Figure 33. The main difference between the PFHnD performance is the degree of preconditioning, which is when the PFHnDs require repeated lasing before significant US contrast is generated (Figure 30). This may suggest that the act of vaporization itself may not be the most effective manner for sonoporation.

#### *4.3.2 Concentration*

Using IR1048 PFHnDs, the conditions for sonoporation was further optimized. To examine the impact of the concentration of the nanodroplets, HADMSCs were incubated with PFHnDs at concentrations varying from (1x10<sup>9</sup> to 1x10<sup>11</sup> droplets/mL), and the concentration was found to have a substantial impact on the sonoporation rate (Figure 12 A) and a modest impact on viability (Figure 12 B).

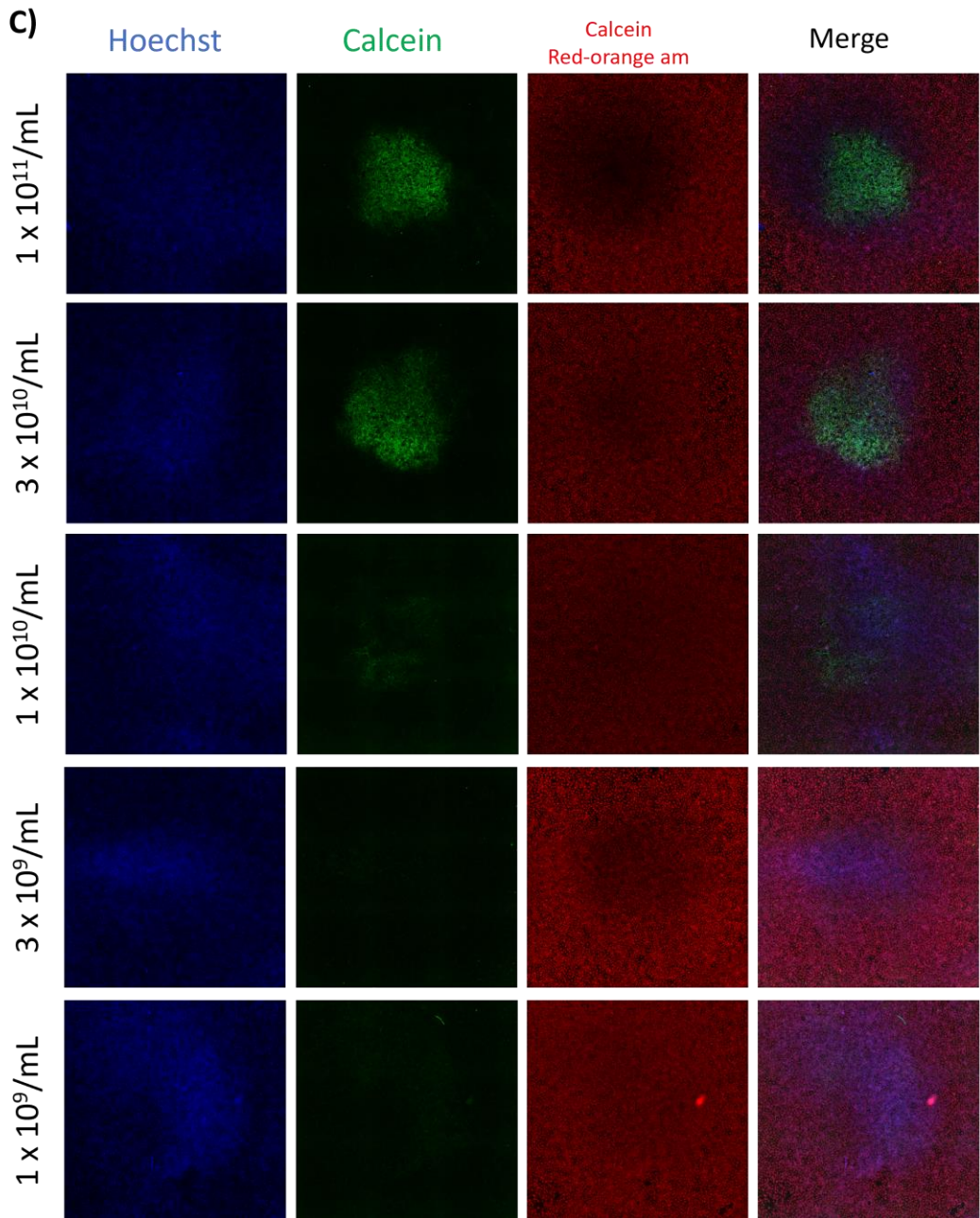
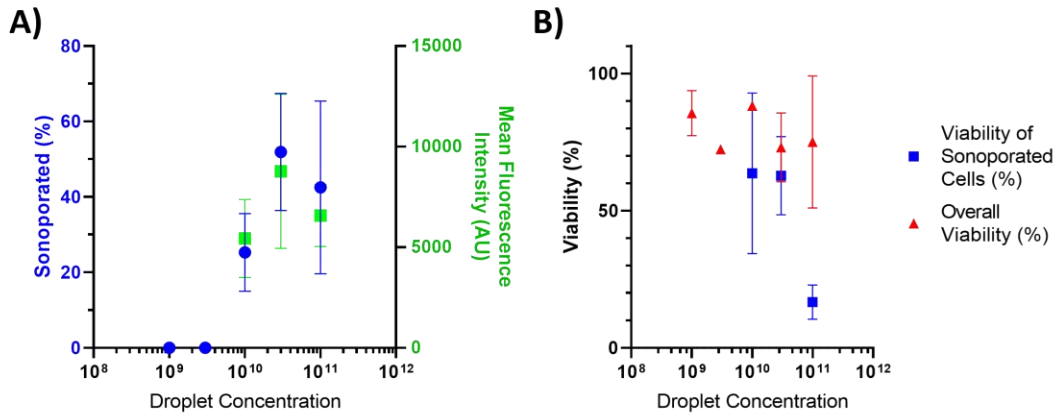


**Figure 12 – A) The sonoporation rate and the mean fluorescence intensity of successfully sonoporated cells as a function of the PFHnD concentration lased at 100 pulses at 60 mJ/cm<sup>2</sup>. B) The viability assessed through fluorescence of calcein red-orange of the cell population in the ROI and specifically the sonoporated cells as a function of concentration. C) Representative images of the lased cells. A) and B) are the summation of n = 3 separate replicates with approximately 3000- 8000 cells within the ROI.**

The results identifies a minimal concentration of PFHnDs required to achieve sonoporation, and while higher concentrations do achieve greater delivery, there is appears to be a saturation point above which the sonoporation rate and entry amount plateaus and viability falls. There is significant variance in performance, where the same concentration of PFHnDs may result in different sonoporation rates, but the trend is quite clear. In previous studies, PFHnDs were injected at concentrations of  $\sim 10^{11}$  per mL, which is well within the concentrations needed to produce sonoporation.

#### *4.3.3 Pulse Number*

Repeated lasing could present more opportunities for the nanodroplets to interact with the cells, resulting in a higher rate of sonoporation. To explore this possibility, HADMSCs were incubated with PFHnDs at a concentration of  $3 \times 10^{10}$  particles/mL and lased at 60 mJ/cm<sup>2</sup> for varying number of pulses (100-600 pulses). The pulse number was varied from (100 – 600 pulses) and was found to have minimal impact on the sonoporation rate (Figure 13 A) and viability (Figure 13 B).

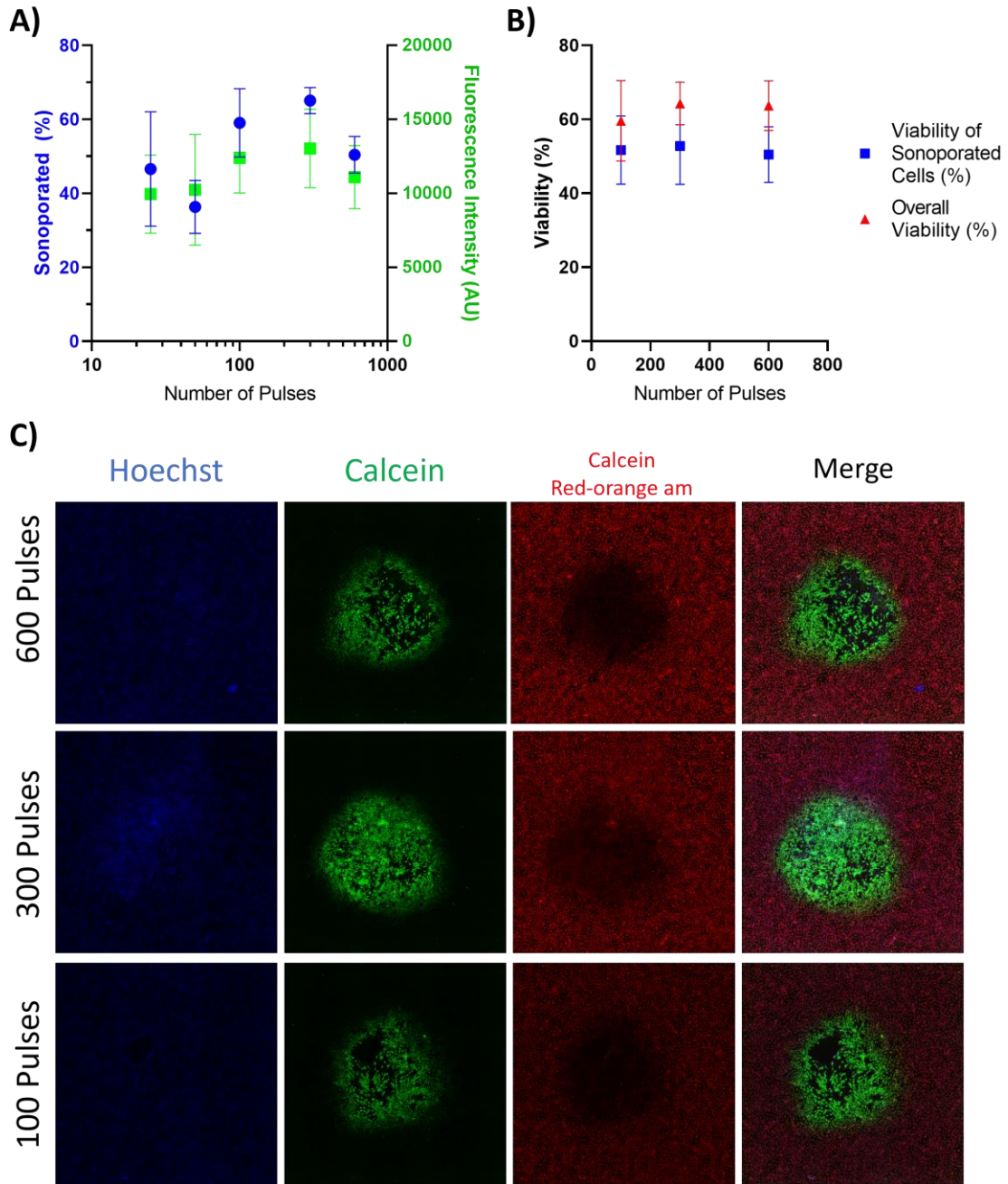


**Figure 13 – A)** The sonoporation rate and the mean fluorescence intensity of successfully sonoporated cells as a function of the pulses ( $60 \text{ mJ/cm}^2$ ) the PFHnDs and HADMSCs were lased. **B)** The viability assessed through fluorescence of calcein red-orange of the cell population in the ROI and specifically the sonoporated cells as a function of number of pulses. **C)** Representative images of the lased cells. A) and B) are the summation of  $n = 3$  separate replicates with approximately 3000- 8000 cells within the ROI.

While little difference was observed between the various pulse numbers examined, this outcome suggests that the vast majority of sonoporation activity occurs within the first 100 pulses and subsequent lasing produces minimal effect. An additional study was performed to examine lower pulse numbers (25 and 50) and found minimal difference in the sonoporation rate and fluorescence intensity. However, there calcein red-orange stain appeared abnormally dim, and the viability assessment was not included.

#### *4.3.4 Fluence*

Another factor to consider would be the fluence of the laser pulse. Higher fluence would result in both greater proportion of vaporization and greater photoacoustic pressure generated from the dye. To test this, the fluence was varied from 30 mJ/cm<sup>2</sup>, 60 mJ/cm<sup>2</sup>, and 90 mJ/cm<sup>2</sup> (Figure 14).

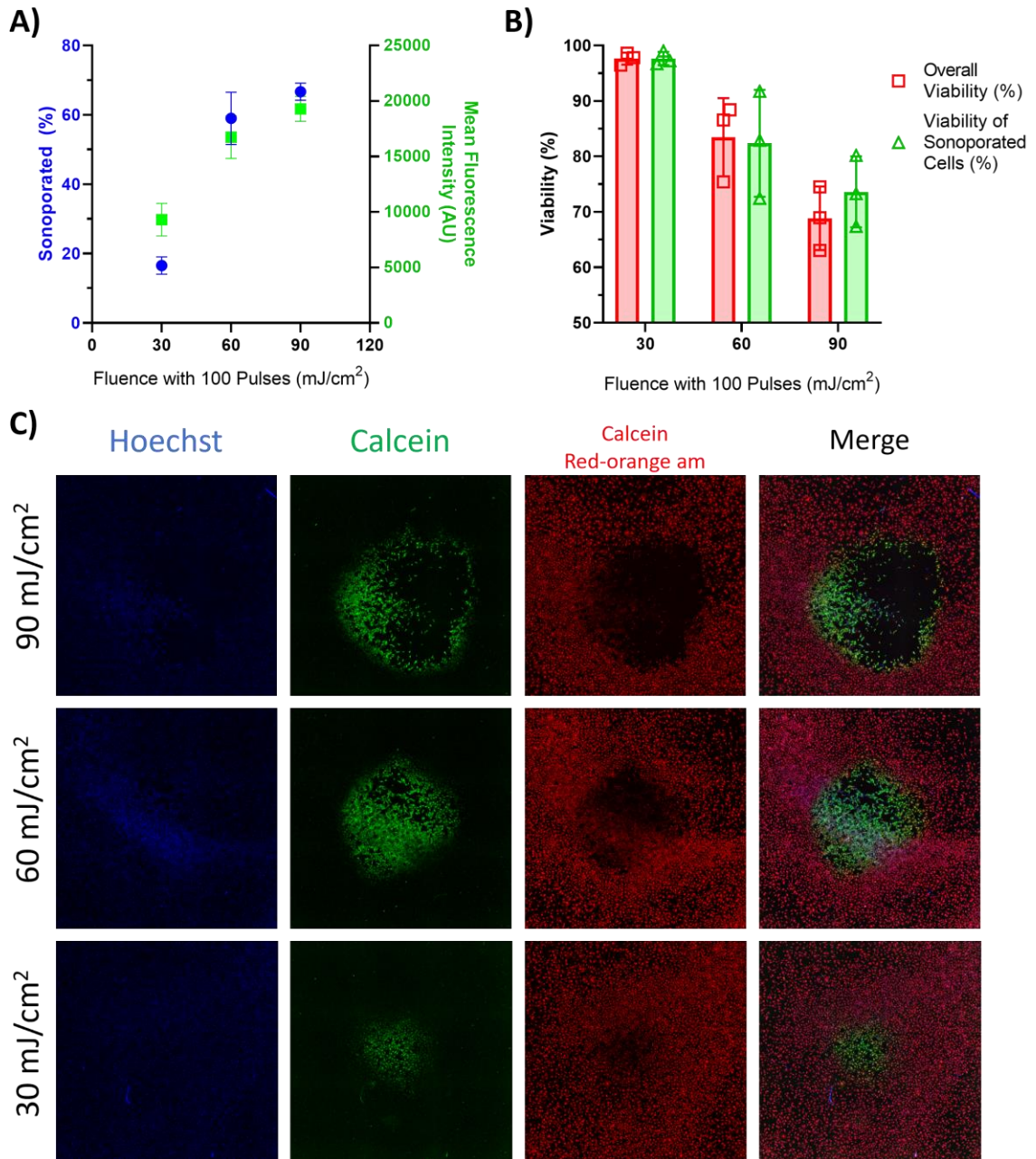


**Figure 14 – A)** The sonoporation rate and the mean fluorescence intensity of successfully sonoporated cells as a function of the fluence at which the PFHnDs and HADMSCs were lased (100 pulses). **B)** The viability assessed through fluorescence of calcein red-orange of the cell population in the ROI and specifically the sonoporated cells as a function of fluence. **C)** Representative images of the lased cells. **A)** and **B)** are the summation of  $n = 3$  separate replicates with approximately 3000- 8000 cells within the ROI.

Greater fluences resulted in greater delivery in terms of mean fluorescence intensity (Figure 14 A), however at higher energies, cell viability decreased (Figure 14 B) more cells were dislodged (Figure 14 C). Viability could only be examined for the cells that remained, and given the geometry of the dish, cells could not be seeded without accumulations occurring in the center, resulting in varying cell counts in the ROI between dishes. This loss of cells results in an underestimate on the true sonoporation rate at fluences of 90  $\text{mJ}/\text{cm}^2$ , and the viability assessment belies the true proportion of cell loss. This is also seen to a lesser extent in lower fluences such as 60  $\text{mJ}/\text{cm}^2$ . At fluences of 30  $\text{mJ}/\text{cm}^2$ , there is substantially less delivery and less loss cells. The higher fluence results in greater vaporization, which could damage the cells and result in them detaching immediately or after the multiple washing steps. As the cells are in close proximity, the loss of several cells could result in the detachment of other cells that are adhered to each other through cell adhesion molecules.

The number of sonoporate cells increase at higher fluences and are primarily clustered around the center of the beam (Figure 14 C). This increasing region is due to the beam profile of the Nd:YAG laser utilized in the study. As the fluence over the diameter of the beam is roughly gaussian, the center of the beam has greater local fluence compared to the outer edges of the beam. Sonoporation appears to require a prerequisite amount of energy, and as the average beam fluence increases, a larger proportion of the beam meets or exceeds this threshold.

#### *4.3.5 Size Dependence of Therapeutic Delivery*

Calcein is often used for determining cell membrane disruption, however it is much smaller in size (622.55 Da) than many therapeutics. To examine the limitations of sonoporation using PFHnDs, dextran beads (MW: 3000-5000 Da) functionalized with fluorescein isothiocyanate (FITC) and nanodroplets were incubated with the cells and lased (Figure 15).

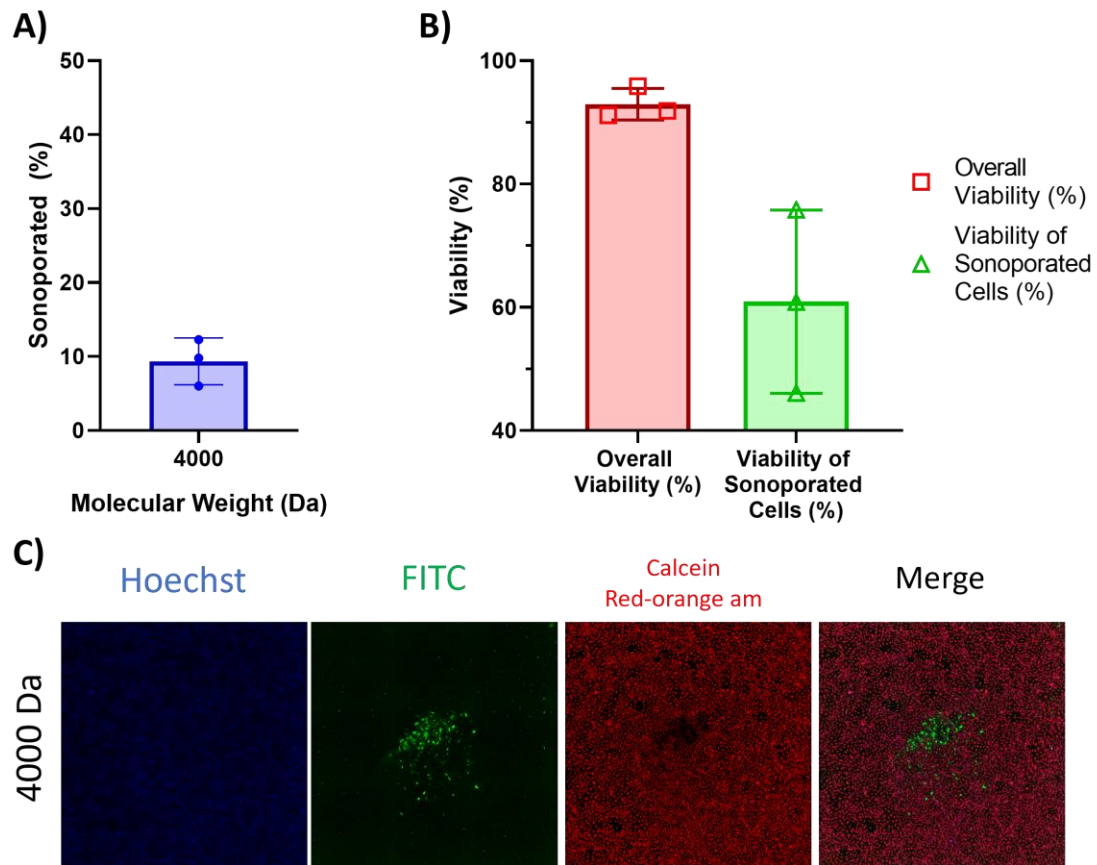


**Figure 15 – A)** The sonoporation rate of dextran beads (mw: 3000-5000 Da) labeled with fluorescein isothiocyanate (FITC) into HADMSCs that were lased ( $60 \text{ mJ/cm}^2$  with 300 pulses) with PFHnDs ( $3 \times 10^{10}$  particles/mL). **B)** The viability assessed through fluorescence of calcein red-orange of the cell population in the ROI and specifically the sonoporated cells as a function of fluence. **C)** Representative images of the lased cells. A) and B) are the summation of  $n = 3$  separate replicates with approximately 3000- 8000 cells within the ROI.

The larger beads exhibit substantially reduced entry into the cells in comparison to calcein. The full set of images of the samples is shown in (Figure 34). Furthermore, as only the cells in the center of the ROI exhibit any entry of the beads, it suggests that the entry is only due to high laser fluence. As explained earlier, each laser pulse has hot spots that typically occur in the near the center of the beam, where fluence is elevated. In addition, the sonoporated cells exhibit substantially lowered viability.

#### 4.3.6 Cell Variation

All the previous studies have been performed on HADMSCs, which are much larger in comparison to other cell types. To examine whether this phenomenon is generalizable to other cell types, three different cell types were lasered in the presence of PFHnDs (Figure 16).

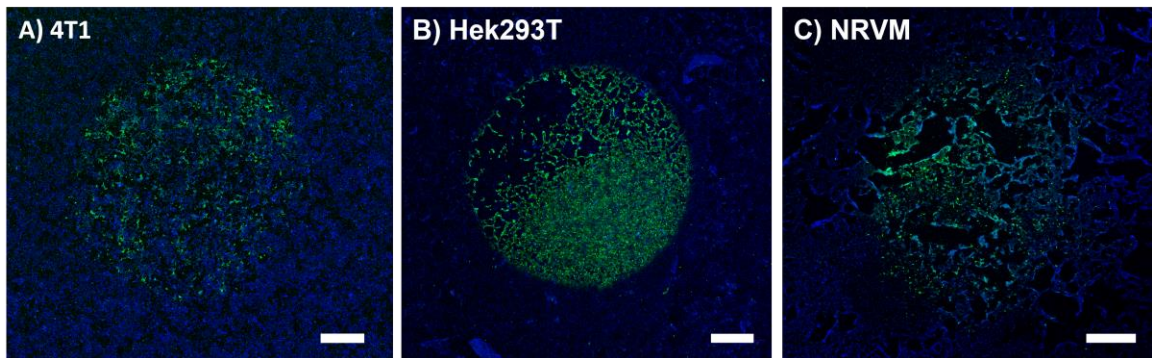


**Figure 16 – Representative images of sonoporation in different cell types: A) 4T1 B) Hek293T, and C) Neonatal Rat Ventricular Myocytes (NRVM). Scale bars represent 1 mm.**

While sonoporation appears to work on all the cell types tested, there are different degrees of response to the sonoporation. 4T1 cells and primary neonatal rat ventricular myocytes (NRVMs) exhibit limited uptake in comparison to the Hek293Ts and the HADMSCs. For

4T1s, their small size and tendency to clump together may limit their exposure to the PFHnDs. Though Hek293T cells have a similar size and tendencies, the cell line has been known to be more susceptible to transfection. Primary cells on the other hand are much resistant and show more limited signs of sonoporation, despite their larger size. Overall, all cell types tested have shown some signs of sonoporation.

#### *4.3.7 Long Term Viability*

Many of the sonoporated cells exhibited reduced calcein red-orange signal that may be due to the formation of pores that allow for the esterases that cleave the dye in viable cells to either escape, result in conditions that inactivate them, or allow for cleaved calcein red-orange to escape. Cells that exhibited a mean fluorescence intensity that is greater than 1.5 times the background were considered viable. However, the fluorescence intensity is significantly lower in comparison to unlased cells. It is unclear what the viability of these cells are long term with some studies showing that sonoporated cells with high dye uptake exhibit minimal viability 6 hours post-sonoporation.<sup>81</sup> To examine longer term impacts of sonoporation, an MTT assay was performed on HADMSCs incubated with PFHnDs and lased 24 hours after the exposure (Figure 17).

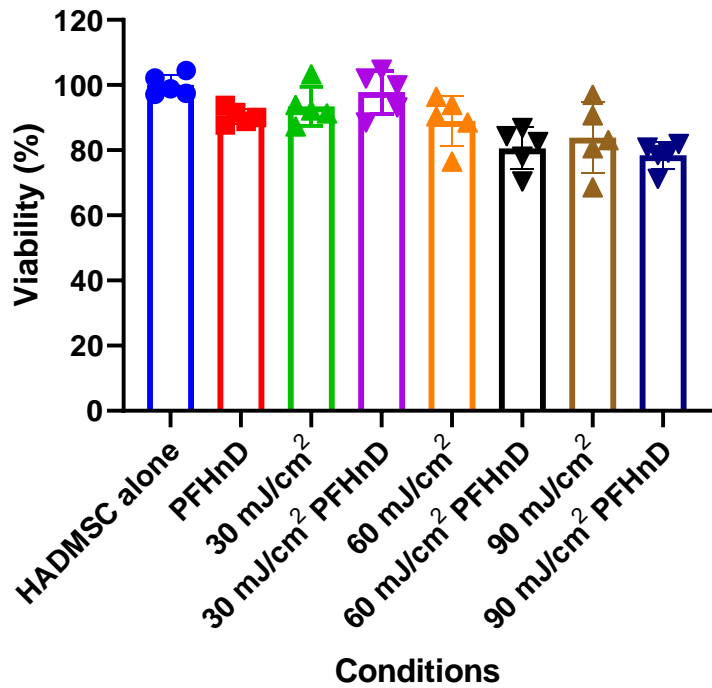


**Figure 17 – MTT assay performed on HADMSCs seeded in a 96 well plate. The PFHnDs were added at concentrations equivalent to  $3 \times 10^{10}$  droplets per mL and select wells were lased at different fluences for 100 pulses. The bars represent the mean of  $n = 5$  replicates with error bars representing the standard deviation.**

The PFHnDs exhibit minimal toxicity, which was not statistically significant, and the addition of PFHnDs did not exhibit statistically significant difference in viability compared to their equivalent counterparts. Lasing at high fluences was found to impact viability of the cells. This data does correlate well with the calcein red-orange staining, with viabilities being similar between the same conditions.

One possibility is that the repeated vaporization often loosens up the cells by disrupting the cell membrane and the repeated washing after this process end up dislodging the cells. Cells lased at fluences higher than  $30 \text{ mJ/cm}^2$  exhibited a greater propensity to be

dislodged. However, in the well plate, no wash steps were performed. This could allow for cells that normally would have been washed off remain adhered and recover.

#### **4.4 Discussion**

Lasing of PFHnDs has been shown to allow for calcein dye to enter the cytoplasm. Given that the uptake of the dye is constrained to the lased region, and the dye appears to be distributed throughout the cell; the uptake cannot be due to natural cellular processes such as endocytosis.

Interestingly, the type of dye that is incorporated within the PFHnD appears to play a vital role in efficacy. Both IR1048 and Epolight 3072 PFHnDs have similar vaporization thresholds ( $\sim 25 \text{ mJ/cm}^2$  and  $\sim 20 \text{ mJ/cm}^2$  respectively), which are lower than the fluences used in that study (100 pulses at  $60 \text{ mJ/cm}^2$ ). However, IR1048 PFHnDs exhibit a high degree of preconditioning, meaning that there is reduced vaporization during the initial 100 pulses. This suggests that the photoacoustic intensity from the dye alone is more effective than the vaporization from the droplets. While it is unclear what the individual contributions of either the vaporization event or the PA pressure from the dye, previous studies have shown that the contribution of the vaporization event itself is greater than that of the absorber, that study used relatively low amounts of gold nanoparticles.<sup>30</sup> In this study, a much higher dye concentration was used, and the PA intensity of the dye is on the same order of magnitude to that of the vaporization event. This was done based upon findings in a previous study where it was shown that higher dye loading does not reduce the vaporization threshold, but it increases the percentage of droplets that can vaporize.<sup>32</sup>

A similar study that examined photoporation rates when lasing carbon black nanoparticles in the presence of cells resulted in high transfection rates.<sup>82</sup> However, a follow up study identified energy transduction parameters (i.e. peak nanoparticle temperature, size and number of microbubbles generated) provided the greatest impact on photoporation,<sup>83</sup> which seems to suggest that the cavitation of water is pivotal. A more analogous study using gold nanoparticles in BSA nanodroplets demonstrates that timing the lasing of the nanodroplet in tandem with FUS can influence the sonoporation rate, suggesting that sonoporation is dependent on the vaporization of the nanodroplet and not just the photoacoustic pressure from the dye.<sup>80</sup> However, the timing of the laser at best could increase the sonoporation rate from ~30% to ~40%. One thing to note is that in many of those studies, non-adherent cell lines are utilized. These cells will have greater exposure to the resulting pressure wave from the lasing and vaporization, and it is not representative of the in vivo environment. Furthermore, it is possible that during processing of the cells, many of the fragmented and dead cells are lost during the washing process.

Using nanodroplets, it is not possible to separate the contribution of either the dye or the vaporization event itself without introducing further variables. However, the comparison between Epolight 3072 and IR1048 does illustrate a wide gap between the consistency and the mean transfection rates. One possibility is that vaporization of the nanodroplets is more likely to result in coalescing of vaporized nanodroplets which would be incapable of vaporizing or float away, reducing the local concentration of nanodroplets. As Epolight 3072 PFHnDs are more likely to vaporize, they may be more susceptible to coalescing. Supporting this hypothesis, microbubbles were observed that appeared to adhere onto the surface of the cells as multiple wash steps did not remove them (Figure

32), and their appearance is more prominent at higher fluences and high concentrations of nanodroplets. In addition, as illustrated in (Figure 12 A), PFHnD concentration has a large impact on the transfection efficiency. However, there is an upper limit to this efficiency, which could also support the coalescing hypothesis. Higher concentration of nanodroplets, even PFH with its high boiling point, will exhibit a higher propensity to coalesce. This could provide an upper limit on the transfection rate if new PFHnDs are not introduced.

This observation is further supported by the pulse number experiment (Figure 13) where the number of pulses had limited impact on the sonoporation rate and the delivery efficiency. The results suggest that sonoporation is most effective during the initial pulses and subsequent pulses provide limited enhancement. As the PFHnDs are repeated lased, the droplets generate less US contrast due to coalescing and destruction of the nanodroplets, which is shown in Figure 3 and Figure 5. The destruction and coalescing could reduce the local concentration of the nanodroplets at subsequent pulses, which limits the effectiveness of later pulses.

Varying fluence provides additional insight into the requirements of sonoporation. IR1048 PFHnDs start vaporizing at around  $\sim 25 \text{ mJ/cm}^2$ , however the US intensity reaches its 50% maximum at around  $40 \text{ mJ/cm}^2$  (Figure 30). At  $30 \text{ mJ/cm}^2$ , only a small fraction of the PFHnDs are capable of vaporizing, and sonoporation is centered around the center of the beam in which the local fluence is greater. As the fluence increases, the area of sonoporated cells expands because more of the central beam region surpasses the sonoporation threshold.

The cells within the center of the beam appear to have the highest fluorescence intensity, while the cells on the periphery have lower fluorescence intensity. This suggests that while sonoporation is not entirely binary, the transition is rather sharp and suggests that there exists a threshold for which sonoporation occurs. This does suggest that vaporization is pivotal to sonoporation, but, it does not indicate that vaporization is the sole cause of sonoporation, as the PA intensity from the dye will also increase linearly with fluence.

Another key observation is that increasing the fluence has resulted in greater delivery and greater sonoporation rate, along with greater loss of cells. The higher fluence likely results in more violent vaporizations that along with creating more and/or larger pores in cell membranes may disrupt the cell membrane or adhesion proteins that dislodge the cells. This result is not surprising as repeated vaporization has been utilized to disrupt a blood clot<sup>78</sup> and open the tight junctions that make up the blood brain barrier.<sup>34</sup> The loss of cells appears to correlate with greater lasing fluence, but there is variance between experiments that may depend on arbitrary biological factors such as passage number and the orientation in which the cells adhered onto the dish.

When considering the size of cargo that can be delivered, it is shown that the larger the cargo the lower likelihood of successful entry into the cell (Figure 15). Delivery for large particles appears to be fluence dependent, as the sonoporated cells center around the middle of the beam. This does align the earlier observation of higher fluence resulting in higher delivery amounts and suggests that sonoporation at higher fluences create larger pores within the cell membrane. Naturally, there is an upper limit to this before the cells are no longer viable, in those cases the cells are more susceptible to being dislodged by the

washing steps. This likely limits the delivery potential of ODV triggered sonoporation to small molecules, which are smaller than 1000 daltons, unless there are future optimizations that can be used to enhance the delivery without negatively impacting viability.

On the other hand, sonoporation appears to be cell type independent, with multiple different types of cells being susceptible to sonoporation (Figure 16). This suggests that the process could be utilized to deliver therapeutics in multiple different applications. However, qualitatively, the susceptibility to sonoporation varies between cell types. This could be based upon the cell size as larger cells such as the HADMSCs exhibit higher rates of sonoporation than smaller cells such as the 4T1s.

Sonoporated cells often exhibited lower calcein red-orange fluorescence intensity compared to the unlased cells. While this signal was greater than the background, it is unclear if these cells would recover. An MTT assay performed 24 hours after lasing suggests that high lasing energy. For this study, the beam approximately covered the entire well, while the fluence at the edges of the beam are reduced due to the gaussian intensity distribution. The presence of PFHnDs depresses the metabolism of the cells to around 80% of the control. The high sonoporation rate (greater than 40%) and the high viability of the MTT assay suggests that a large fraction of sonoporated cells may be viable after 24 hours.

In its current form, ODV for sonoporation has many hurdles before practical clinical applications. The high fluence requirement limits the delivery depth within the body as light is scattered substantially in tissue. While there are methods that can be utilized to overcome this such as catheter based light delivery or triggering vaporization through other means such as acoustic,<sup>84</sup> acoustic and optical,<sup>80</sup> or utilizing microwaves,<sup>85</sup> further work

would need to be done to examine the impact of those alternative approaches. While the concentration used in this study fall well within the concentrations commonly used for contrast agents, these agents will likely need to be injected locally rather than systemically as the sonoporation efficiency is highly concentration dependent. Future steps could examine if the efficiency could be improved through targeting approaches to locally increase the concentration of the nanodroplets and decrease the proximity between the PFHnDs and the targeted cells.

#### **4.5 Conclusion**

In this chapter, the impacts of vaporization of nanodroplets on cells is explored in the context of sonoporation. By varying the dye used in formulation, sonoporation efficiency is enhanced based upon the dye. The sonoporation effect is highly dependent upon the concentration of the PFCnDs, with lower concentrations exhibiting markedly little to no delivery. Fluence greatly impacts both the sonoporation rate, amount delivered, and negatively impacts the viability of the cells. Indicating that there exists a happy medium for delivery with minimal cell death. This technique is however limited to small molecules as dextran beads that are larger in size exhibit a low rate of entry. ODV induced sonoporation appears to be cell type independent, with sonoporation observed in all tested cell types. While sonoporation impacts the viability of the cells, even at high fluences the toxicity appears limited. Taken together, this suggests that ODV induced sonoporation can provide an image guided approach to intracellular delivery of small molecules.

#### **4.6 Acknowledgments**

NRVMs were isolated by and generously provided by Dr. Heecheol Cho.

## CHAPTER 5. DOUBLE EMULSION PFCNDS FOR HYDROPHILIC DRUG DELIVERY

### 5.1 Introduction

The pinnacle achievement in the field of drug delivery would be the capacity to finely regulate the spatial and temporal control of drug release within the human body with feedback to monitor the trafficking of the drug and estimate local dosage. This ability would be able to give clinicians unprecedented ability to both target and monitor treatment. The ability to control the release is imperative to avoid non-specific toxicity. A recent literature survey has found that only 0.7% of an administered nanoparticle dose actually reaches a solid tumor.<sup>86</sup> This can result in non-specific delivery of therapeutics that can lead to poor health outcomes particularly for formulations that do not possess a mechanism for targeted release.

One way to limit this is to develop stimuli responsive particles that can deliver therapeutics from either internal (pH, GSH, etc.) or external conditions (light, ultrasound, etc.) to target the tumor microenvironment in a spatially controlled manner.<sup>87</sup> PFCnDs have been modified to allow for the encapsulation and release of drugs based upon external acoustic stimuli. These modifications primarily utilize the shell to encapsulate hydrophobic or amphiphilic moieties such as doxorubicin or paclitaxel.<sup>33,88,89</sup> However, this approach limits the types of drugs that can be delivered to only hydrophobic and amphiphilic. One approach to remedy that issue was to encapsulate PFCnDs within liposomes that could then be ruptured through ultrasound stimulation.<sup>90,91</sup> Other approaches sought to develop

double-emulsion nanodroplets that contain an internal emulsion that can solubilize hydrophilic drugs. This internal emulsion is then surrounded by a layer of perfluorocarbon which is stabilized by an outer shell, similar to a standard PFCnD. The earliest formulations produced relatively large micron-sized particles that could be triggered to release drugs through exposure to ultrasound.<sup>92,93</sup> Others have iterated upon this approach, producing smaller droplets, but these are prone to leakage.<sup>27</sup>

In this study, we aim to develop a double emulsion PFCnD that is optimized for hydrophilic drug encapsulation and can be tracked using PA imaging and once reaching the target site, release the encapsulated drugs through FUS stimulation. We aim to achieve this using a higher boiling point PFC and further optimization of the formulation to achieve more stable encapsulation and allow for vaporization without release. To demonstrate functional release of a therapeutic, poly I:C was encapsulated in the presence of macrophages.

## **5.2 Materials and Methods**

### *5.2.1 dePFHnD Synthesis and Characterization*

dePFHnDs were synthesized using probe sonication. First, 75mg of 008-FluoroSurfactant (RAN Biotechnologies, MA, USA) was added to 1.5 ml of ice-cold perfluorohexane (PFH, FluoroMed, TX, USA). Then, 1.5mL of a hydrophilic model drug solution (0.5mg/ml calcein (Sigma-Aldrich, MO, USA), filtered through a 0.2 $\mu$ m filter) in PBS or 10mg/ml Poly (I:C) (Sigma-Aldrich, MO, USA) in PBS was mixed with the 008-FluoroSurfactant in PFH. This mixture was probe sonicated (Q700, QSONICA, CT, USA) in an ice bath at an amplitude of 1 (30 watts/cm<sup>2</sup>) for 30s to fabricate the first emulsion. A

volume of 1.5ml of the first emulsion was added to the 3ml of 0.5% pluronic f-68 (Sigma-Aldrich, MO, USA) in PBS with a NIR dye (0.2mg of Epolight 3072 (Epolin, NJ, USA)) with a peak absorbance at 1064nm. The mixture was then probe sonicated for 60s using the same parameters as the first emulsion to form the second emulsion.

The dePFHnDs mixture was centrifuged at 43 RCF for 3 min using a mini-centrifuge (5452 Minispin Centrifuge; Eppendorf, Hamburg, Germany) to remove large particles and unencapsulated dye. After discarding the pellet, the supernatant underwent three rounds of centrifugation at 4500 RCF for 3 minutes to remove the residual free hydrophilic drug. After each centrifugation step, the supernatant was discarded, and the pellet was resuspended with PBS.

The average size of the dePFHnDs was determined by a Malvern Zetasizer Dynamic light scattering (DLS, Zetasizer Nano ZS; Malvern Panalytical, Malvern, UK) after 1000-fold dilution. Internal structure of the double emulsion was verified utilizing cryo-TEM imaging. Methods are similar to those in 3.2.2. Briefly, Nanoparticle preparations were plunge frozen onto glow-discharged, 200 mesh, copper Quantifoil grids in liquid ethane using a Vitrobot Mark IV. Cryo-TEM images were acquired on a 120 kV Talos L120C TEM (Thermo Fisher Scientific, USA) with a Ceta CMOS camera. Most of the images were collected at a magnification of 36Kx (pixel size 4 Å/pix) and 45Kx (pixel size 3.2 Å/pix). The dose rates were between 15 to 20 e/Å<sup>2</sup>. The defocus range used was from -4 to -5.

The loaded drug amount in the nanodroplets was measured by freezing 200ul of sample overnight at -80°C, followed by lyophilization (Labconco, MO, USA) for a day.

The resulting powder was resuspended in 200ul PBS and centrifuged at 4500 RCF for 3 minutes to remove the surfactants. The resulting supernatant (100uL) was added to a black 96-well plate. Using a microplate reader (Cytation 7; BioTek Instruments, VT, USA) with the standard plate reader software (Gen 5; BioTek Instruments, VT, USA), the fluorescence of each well was measured with 485 nm excitation and 528 nm emission. The fluorescence intensity was converted to calcein concentration using a standard made from calcein solution at concentrations ranging from 62.5  $\mu\text{g/ml}$  to 3.8  $\text{ng/ml}$  in PBS. Release efficiency was calculated by dividing the released calcein by the amount of loaded calcein.

For the stability test, sizing and loaded drug measurements were conducted using the same procedure after storage at 4°C for one, three, five, and seven days after synthesis.

### 5.2.2 *Lasing and Heating*

To evaluate the drug release behavior of nanodroplets under laser irradiation, dePFHnDs loaded with calcein were diluted 2-fold and placed within a 96-well plate. Each well was lased utilizing a custom-built well plate lasing system. The system consisted of a 10 Hz pulsed Nd: YAG laser (Vibrant; Opotek Inc, CA, USA) with a 3-axis motion stag, and the number of pulses and lasing intensity irradiated into each well were adjusted through LabVIEW software (National Instruments, TX, USA). To evaluate the effect of laser intensity on calcein release, the number of pulses was held constant at 100, while the laser fluence was varied: 0, 20, 50, 70, and 100  $\text{mJ/cm}^2$ . Similarly, to analyze the effect of the number of pulses, the laser intensity was set to 70  $\text{mJ/cm}^2$ , and the number of pulses was varied to 0, 10, 100, and 1000.

To quantify the drug release efficiency of the lased dePFHnDs samples, the irradiated samples were centrifuged at 4500 RCF for 3 minutes to remove residual nanodroplets. The resulting supernatant (100uL) was added to a black 96-well plate, and the concentration was determined as previously described.

To determine the effect of heating on drug release and size variation, the 2 times diluted dePFHnDs were placed in a mini heat block (Fisherbrand, MA, USA) at 25°C, 37.5°C, 50°C, 60°C, and 70°C for 10 minutes. DLS was used to determine the size after heating. 200uL of heated samples were transferred to a 1.5 ml microtube (USA Scientific, FL, USA) and centrifuged at 4500 RCF for 3 minutes to remove residual nanodroplets. The concentration of calcein in the supernatant solution was determined as stated earlier.

### *5.2.3 Focused Ultrasound Parameter Optimization*

To optimize the drug release effect of nanodroplets through focused ultrasound (FUS), dePFHnDs were suspended within a polyacrylamide cuvette phantom and exposed to a range of acoustic parameters.

The polyacrylamide cuvette phantom was synthesized by combining 50 ml of a 40% polyacrylamide solution (Sigma-Aldrich, MO, USA), 150 ml of deionized water, and 2 ml of a 10% ammonium sulfate solution (APS, Sigma-Aldrich, MO, USA). This mixture was placed in a vacuum flask, sealed with a rubber stopper, and connected to a vacuum. The solution was then degassed using a water bath sonicator. After degassing, 250 ul of TEMED (N,N,N',N'-Tetramethylethylenediamine, Sigma-Aldrich, MO, USA) was added to the degassed solution and poured into a rectangular plastic mold to solidify. During the solidification process, a plastic cuvette was inserted center of the phantom to create a

rectangular void. Once the phantom was fully polymerized, the cuvette was removed, and the phantom was extracted from the plastic mold.

The cuvette phantom was placed in a 37°C water bath (WB-200; Cole-Parmer, IL, USA), and the dePFHnDs samples were diluted 2-fold and placed within the rectangular void area of the phantom. Focused ultrasound sonication was performed utilizing a ring-shaped single-element 2MHz focused ultrasound transducer (H-148, Sonic Concept, WA, USA) with a focal length of 63.2mm. The 2MHz sinusoidal pulse with varying peak negative pressures (PNP), duty cycles, pulse repetition intervals (PRI), and durations was generated by a function generator (AFG3022C; Tektronix Inc, OR, USA). This pulse was then amplified by 55dB with an RF power amplifier (1040L; Electronic and Innovation, NY, USA) and transmitted via an impedance-matching circuit to the focused ultrasound transducer. To identify optimal acoustic parameters, individual parameters were modified while keep others at default values: 1.44 MPa PNP, 50% duty cycle, 300 ms PRI, and 120 s duration. However, for the duration experiment, three PNPs - 1.08 MPa, 1.44 MPa, and 2.16 MPa – were used. The drug release efficiency was quantified based on fluorescence as stated earlier.

#### *5.2.4 Agarose Gel Electrophoresis*

Agarose gel electrophoresis was used to visualize the release of poly I:C from the dePFHnD. A 1% agarose gel was cast by dissolving 1 gram of agarose (Sigma Aldrich) in 100 mL of TAE buffer (Tris-acetate-EDTA, ThermoFisher Scientific). The solution was then heated in a microwave until the agarose was fully dissolved. The solution was then poured into a mould and allowed to cool until the gel solution solidified. Poly I:C (2.5 µg),

dePFHnD loaded with poly I:C, and dePFHnD loaded with poly I:C after exposed to HIFU were loaded into separate wells with 6x gel loading dye (NEB, MA, USA), and the gel was run with TAE as a running buffer at 120 volts at 0.05 amps for 30 minutes. The resulting gel was then stained using SYBR gold nucleic acid gel stain (ThermoFisher Scientific) for 10 minutes. The gel was then imaged using a Gel Doc EZ Imager (Bio-Rad, CA, USA).

### 5.2.5 *Ultrasound/Photoacoustic Imaging of Phantom and Vaporization Threshold*

To visualize nanodroplets using ultrasound/photoacoustic imaging and monitor changes in ultrasound and photoacoustic signals after various degrees of drug release through focused ultrasound, a polyacrylamide tube phantom was used.

Polyacrylamide tube phantom was synthesized in a similar manner as the cuvette phantom, with the exception that a 5 mm diameter plastic pipette was utilized to create a tubular void.

After focused ultrasound-induced drug release with varying efficiencies, the dePFHnDs samples were diluted 500 times and placed in a tube within the phantom. Both ends of the tube was sealed by ultrasound gel. The phantom was imaged using photoacoustic and plane-wave ultrasound imaging. For this purpose, an ultrasound linear array transducer L11-4v (Verasonics Inc, WA, USA) and an optical fiber bundle positioned on either side of the transducer were placed over the phantom to image the phantom from top to bottom. The imaging probe was acoustically coupled with the phantom using clear ultrasound gel. The ultrasound transducer was connected to a programmable research ultrasound imaging system (Vantage 128; Verasonics, WA, USA) and operated at a center frequency of 7MHz, while the optical fiber was coupled to an Nd: YAG pulsed laser system

operating at 1064nm (Tempest 30, New wave Research, Fremont, CA, USA). The estimated fluence at the output of the fiber bundles, measured by a laser power meter (Nova II, Ophir-Spiricon, UT, USA), was  $75 \text{ mJ/cm}^2$ .

Each sample was imaged in three distinct planes, with each plane irradiated by 66 laser pulses. Photoacoustic images were acquired immediately after each laser pulse. Following that, three ultrafast ultrasound B-mode images were taken at a pulse repetition frequency of 2 kHz using  $0^\circ$  planar ultrasound waves. Background ultrasound images were also obtained prior to laser activation.

The photoacoustic images from each plane were created by averaging 66 individual photoacoustic images. The differential ultrasound images were obtained by averaging three ultrasound images from each laser irradiation, subtracting the background ultrasound image, and then averaging the 66 ultrasound differential images that were obtained. Photoacoustic intensity and ultrasound intensity were determined by integrating over the region of interest.

The vaporization threshold was determined by embedding the dePFHnDs within a polyacrylamide phantom, synthesized using the same methodology as previously described. In this case, dePFHnDs (400  $\mu\text{L}$ ) were added to the phantom to yield a 1:500 dilution of stock dePFHnDs. The phantom was then irradiated for multiple pulses with increasing fluence from  $10 \text{ mJ/cm}^2$  –  $75 \text{ mJ/cm}^2$  at intervals of approximately  $10 \text{ mJ/cm}^2$  with three pulses per fluence. This was followed by 10 pulses at the peak fluence and then a ramp down in fluence using the same fluences as the ramp up cycle. After each pulse, five ultrafast ultrasound B-mode images were taken at a pulse repetition frequency of 2

kHz using 0° planar ultrasound waves. Differential frames were determined by subtracting the fifth frame from the first frame, and the vaporization threshold was determined by plotting the integrated differential US intensity against the fluence acquired during the ramp down cycle. This was then fitted to a sigmoidal curve. The threshold was identified as the intersection of a line drawn from the midpoint of the curve to the x-axis, which shared the same slope as the midpoint of the curve.

#### 5.2.6 *Poly(I:C) dePFHnD Griess Assay*

RAW 264.7 cells were cultured in DMEM supplemented with 10% fetal bovine serum (FBS) and 1% penicillin-streptomycin (P/S). For cell splitting, a cell scraper was used. The RAW 264.7 cells were seeded in a 24-well plate with a fluorocarbon film bottom (Boca Scientific, MA, USA), at a density of 1.2 million cells per well (1 mL) and incubated for 24 hours. Following the 24-hour incubation, the media was replaced with 1.8 mL of phenol-free DMEM. Subsequently, 180 uL of three different solutions (dePFHnDs loaded with poly (I:C), 1 mg/ml concentration free poly (I:C), and sterile PBS) were individually added to separate wells.

Following the addition of particle solutions to the media, the well plates were placed in a 37°C water bath. Half of the wells underwent sonication for 5 minutes using a focused ultrasound sonication system customized for delivering acoustic energy to a cell culture well plate. The sonication system included a ring-shaped single-element 2MHz focused ultrasound transducer (H-148, Sonic Concept, WA, USA) positioned at the bottom of the well plate to deliver acoustic energy from the bottom upward. The 2MHz sinusoidal pulse with 1.08Mpa peak negative pressure, 50% duty cycle, and 15ms pulse repetition

interval was generated by a function generator (AFG3022C; Tektronix Inc, OR, USA) and then amplified by 55dB with an RF power amplifier (1040L; Electronic and Innovation, NY, USA). The amplified pulse was passed through an impedance-matching circuit to the focused ultrasound transducer. To prevent media from splashing onto other samples during sonication, the lid of the well plate was kept closed. After sonication, the 24-well plates were returned to the incubator.

After 24 hours of incubation, 100  $\mu$ L of supernatant was removed from each well and transferred to a well within a 96-well plate. The first three columns of this well plate were loaded with sodium nitrite at concentrations ranging from 25 $\mu$ M to 0.39 $\mu$ M and 0 $\mu$ M dissolved in phenol-free DMEM solvent as standard. A 40mg/ml solution of modified Griess reagent (Sigma-Aldrich) was prepared in deionized water. Then, 100 $\mu$ L of Griess reagent solution was added to each well of the 96-well plate.

After adding the Griess reagent to the samples, the 96-well plate was covered with aluminum foil to minimize light exposure. The plate was incubated for 10 minutes and the absorbance of each well was measured using a microplate reader (Synergy HT; BioTek Instruments, VT, USA) with the standard plate reader software (Gen 5; BioTek Instruments, VT, USA) at 546nm. The absorbance data was converted to moles of nitrite using the standard.

#### 5.2.7 *MTT*

Cytotoxicity was quantified through an MTT assay. RAW 264.7 cells were seeded at  $2 \times 10^5$  cells per well in a 96 well plate. dePFHnDs were added to the cells on the following day at varying concentrations, with PBS serving as a control. On the subsequent

day, MTT (5 mg/mL in PBS, 10  $\mu$ L) was added to each well and allowed to incubate for 2 hours. Afterwards, the supernatant was removed, and the crystals were dissolved in DMSO (150  $\mu$ L). To remove the influence of excess nanodroplets, the DMSO solution was allowed to settle and then the supernatant of each well (100  $\mu$ L) was transferred to another well and the absorbance was measured at 590 nm utilizing the microplate reader (Synergy HT; BioTek Instruments, VT, USA).

### 5.3 Results and Discussion

#### 5.3.1 Formulation Optimization

Previous studies that developed double emulsion droplets utilized two different surfactants: a fluorosurfactant for the inner emulsion (w/f) and an outer surfactant to stabilize the double emulsion (w/f/w).<sup>27,93,94</sup> The outer surfactant was chosen to be pluronic F-68 due to its biocompatibility (FDA approved to reduce viscosity in blood transfusions and other over the counter products)<sup>95</sup> and previous use in double emulsion nanodroplets (Figure 18).<sup>94</sup>

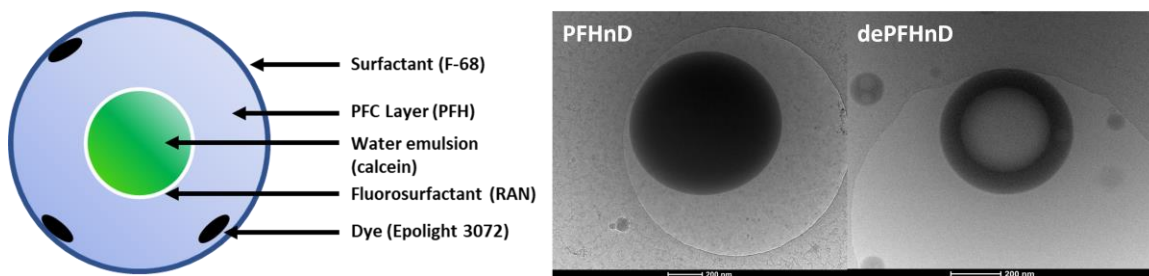


**Figure 18 – Schematic illustrating the overall structure of the double emulsion along with cryo-TEM images taken of droplets synthesized using only a single emulsion and those with a double emulsion.**

To determine the ideal inner surfactant, several different fluorosurfactants were tested: krytox FSL (FSL), krytox FSH, krytox PEG (synthesized from krytox FSL), and 008-Fluorosurfactant (RAN, a commercially available surfactant commonly utilized for droplet microfluidics). From these, RAN and FSL were determined to have the greatest encapsulation efficiency and overall size. However, FSL demonstrated greater toxicity (Figure 37), leading the following work to focus upon RAN. The RAN fluorosurfactant formulation was optimized by varying the concentration from 25 mg/mL to 100 ug/100 uL to achieve the greatest loading efficiency and smallest size of the resulting dePFHnDs (Figure 19 A-B). Higher concentrations of RAN surfactant allowed for greater loading efficiency, while modestly increasing the size. From this 50 mg/mL was selected due to the higher loading efficiency. In comparison to nanodroplets that were solely synthesized with F-68 and calcein (0 mg/mL of RAN), the loading in the nanodroplets with fluorosurfactant is substantially greater (Tukeys,  $p < 0.0001$  for all comparisons) suggesting that minimal calcein is encapsulated within the F-68 shell and that the fluorosurfactant allows for the formation of double emulsion nanodroplets, which enhances the loading efficiency. This is further supported by confocal images taken of dePFHnDs synthesized with FSL that were loaded with calcein in the water in oil emulsion and cy3 loaded into the outer shell (Figure 41). The calcein and cy3 signal showed good correlation. This is because the resolution of the confocal microscope is not great enough to distinguish the outer shell of the dePFHnD from the internal emulsion.

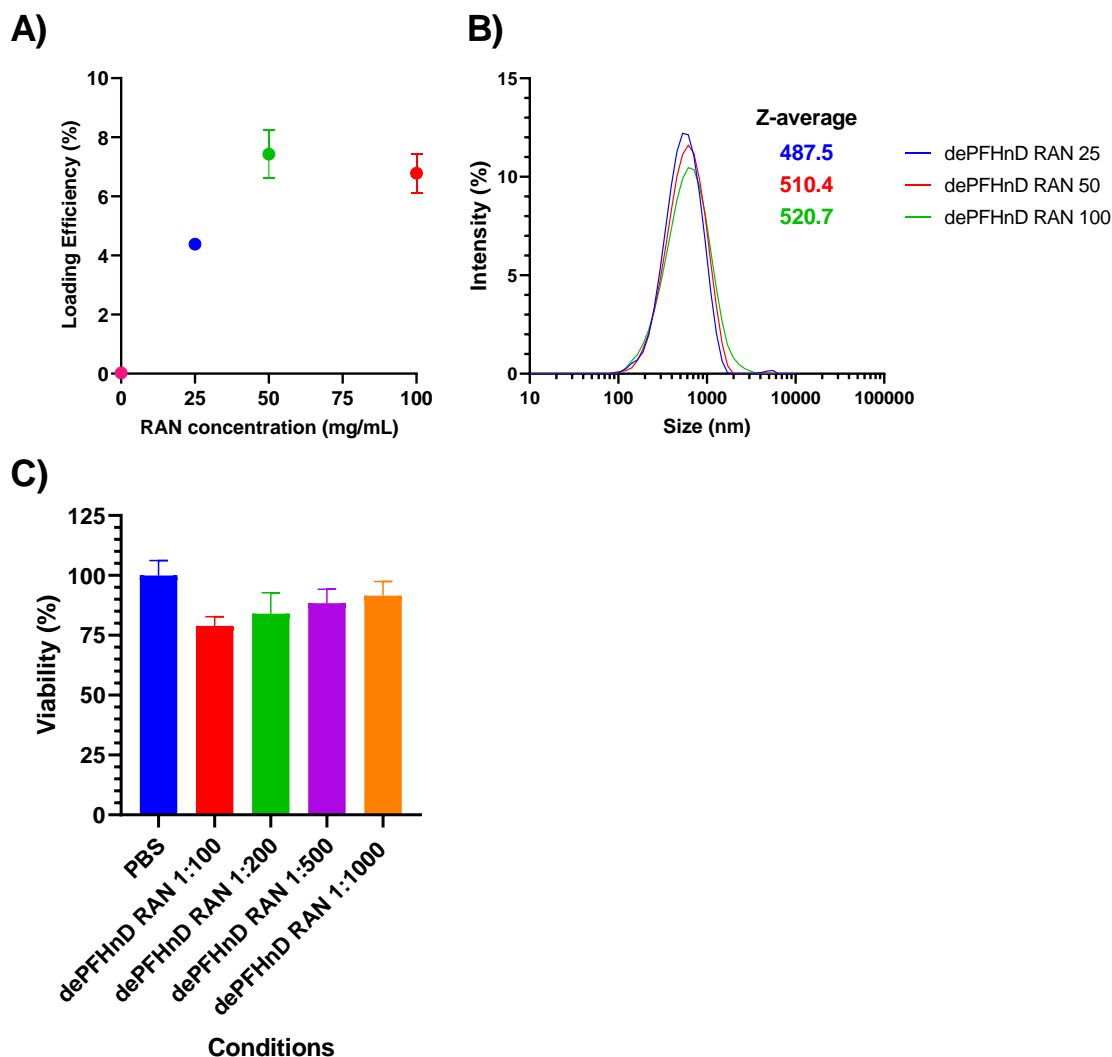


**Figure 19 – A) The loading efficiency of calcein within dePFHnDs as a function of RAN concentration used during the formulation with  $n = 3$  replicates. Differences in the means of the conditions were found to be statistically significant (one-way anova ( $F(3, 8) = 123.0$ ,  $p < 0.0001$ ) with significant differences found between 0 mg/mL of RAN and all other concentrations through Tukey’s multiple comparison test ( $p < 0.0001$ ). B) The size distribution of the resulting dePFHnDs measured by DLS. The size distributions and z-averages are an average of three measurements. C) MTT assay performed to assess the viability of RAW 264.7 cells that were incubated with various concentrations of dePFH synthesized with RAN (50 mg/mL). Error bars represent the standard deviation of  $n = 8$  replicates.**

Through an MTT assay performed by incubating various concentrations of dePFHnDs with RAW 264.7 macrophages, it was determined that at high concentrations dePFHnDs present mild toxicity (Figure 19 C). Greater toxicity was observed in other formulations of the dePFHnDs that used FSL (Figure 37), suggesting that the toxicity is primarily due to the fluorosurfactant. However, as the formulations were washed three times with PBS, it is unlikely that difference in viability is due to unincorporated fluorosurfactant. This implies that the fluorosurfactant is not only stabilizing the inner emulsion but is also incorporated within the outer layer. Zeta potential measurements of dePFHnDs formulated with RAN and PFHnDs formulated with just F-68 indicate that the RAN formulation was more neutral compared to nanodroplets formed with just F-68 alone.

A full characterization of the release profile for FSL dePFHnDs was performed and is described in Supplementary Information for Chapter 5: Double Emulsion Characterization. This characterization can allow for extrapolation of what characteristics are universal for these dePFHnDs and which are likely surfactant specific.

### *5.3.2 Release Quantification*

After developing a formulation that was optimized for greater encapsulation efficiency and smaller size, the release profile due to lasing and HIFU was characterized. To determine the susceptibility for release after lasing, the dePFHnDs were lased in a well plate at varying number of pulses and fluences within the ANSI safety limit, and the release was quantified (Figure 20).

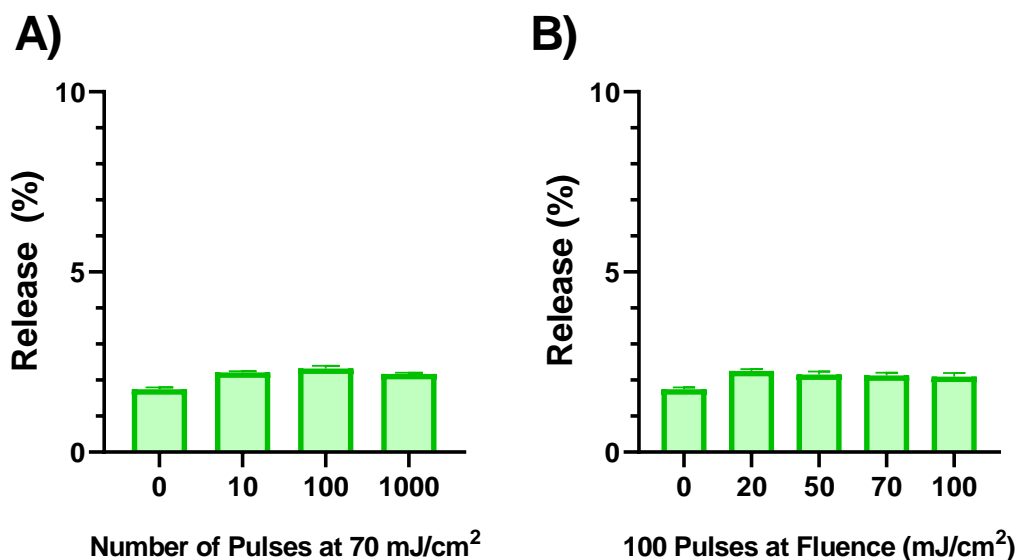


**Figure 20 – The release profile for the dePFHnDs at A) varying number of pulses at 70 mJ/cm<sup>2</sup> and B) at 100 pulses at varying fluences. Bar plots represent mean while the error bars indicate the standard deviation of n = 3 replicates.**

The dePFHnDs exhibited little release regardless of fluence or number of pulses, suggesting that the vaporization event is reversible and does not disrupt the internal emulsion. This runs counter to observations by Spatarelu et al.<sup>27</sup> in which a double emulsion construct formed of PFP exhibited drug release after lasing. We theorize that this is due to a combination of the brevity of the vaporization and the hydrophobicity of the fluorosurfactant, preventing the particle from breaking up. With PFP droplets that were used by Spatarelu et al., the vaporization is more likely a permanent transformation from droplet to microbubble, forcing the encapsulated drugs out of the construct. With the use of PFH, this transformation is transitory and repeatable, suggesting that these nanodroplets could be tracked using photoacoustics without release of the therapeutic cargo. Other formulations such as those using FSL have also been observed to have little to no release

after lasing (Figure 38), further supporting the idea that transitory vaporization reduces the release of encapsulated drugs.

Next, we sought to optimize the release efficiency of the dePFHnDs at different HIFU conditions. By varying the peak negative pressure (PNP), pulse repetition interval (PRI), duty cycle, and duration, the release dependency on each condition was determined (Figure 21).

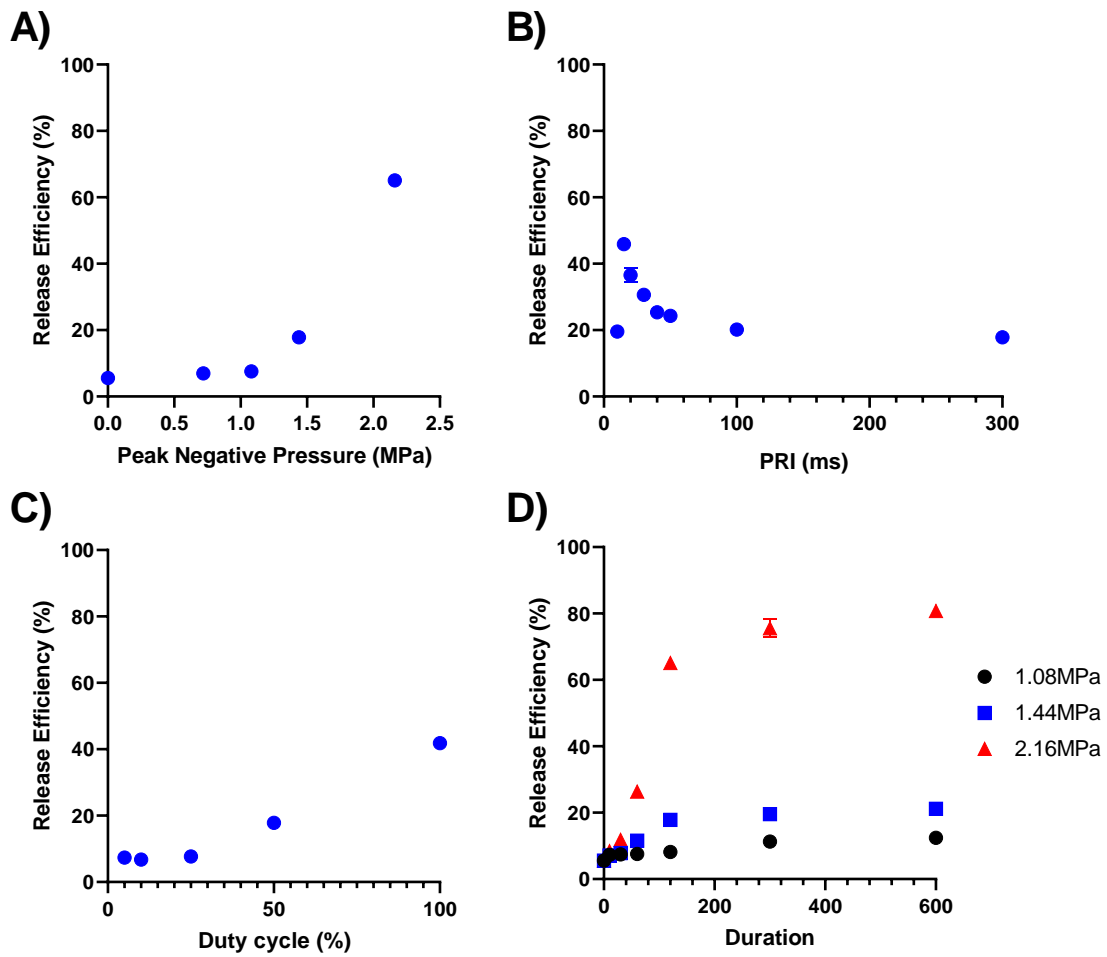


**Figure 21 – The release efficiency of RAN dePFHnDs as a function of A) peak negative pressure (PNP), B) pulse repetition interval (PRI), C) duty cycle, and D) duration at different PNPs. All experiments were conducted under the following conditions, with the exception for the condition being tested: PNP: 1.44 MPa, duty cycle: 50%, PRI:**

**300 ms, and duration 120 s. Each point represents the mean while the error bars indicate the standard deviation of n = 3 replicates.**

From this, it is found that the peak negative pressure has the greatest impact on the release efficiency. The influence of peak negative pressure is not surprising as higher pressures result in greater deposition of thermal energy and greater mechanical impact through cavitation. The greater heat deposition could result in vaporization of the PFH within the dePFHnDs. The formation of this microbubble could aid in breaking up the internal emulsion through FUS mediated effects such as cavitation and microstreaming. This would improve the release of the cargo therapeutic in comparison to lasing, which only provides rapid deposition of heat. One interesting observation is the impact of pulse repetition interval (PRI) upon the release efficiency. This suggests that there is an optimal time period between bursts that further stimulate release. This could be related to the recondensation time of the dePFHnD. One possible explanation is that by shortening the PRI maximizes the number of vaporization and recondensation events from the same set of dePFHnDs, and once that interval is shortened there is a smaller fraction of dePFHnDs that are vaporized. This finding highlights an opportunity to improve release with minimal increase to the mechanical index, and based on similar release studies performed on FSL dePFHnDs (Figure 39), it is likely generalizable to dePFHnDs as a whole.

Other factors such as duty cycle possess much more intuitive explanations. Increasing the duty cycle leads to obvious increases within the release efficiency as longer exposure results in greater heat deposition and exposure to potential mechanical effects from vaporization and cavitation of surrounding dePFHnDs. A similar impact is observed by increasing the duration. However, there appears to be an upper limit on the release

efficiency that is dependent on the PNP, suggesting that there could be various sub-populations within the dePFHnDs that have different thresholds for vaporization.

To clarify the relation between temperature and release rate, dePFHnDs were incubated for 10 minutes at different temperatures ranging from room temperature (24°C to 70°C) and the release was quantified (Figure 22). Temperature had minimal impact on the release, suggesting that the thermal effect from FUS alone is not sufficient for the release observed.

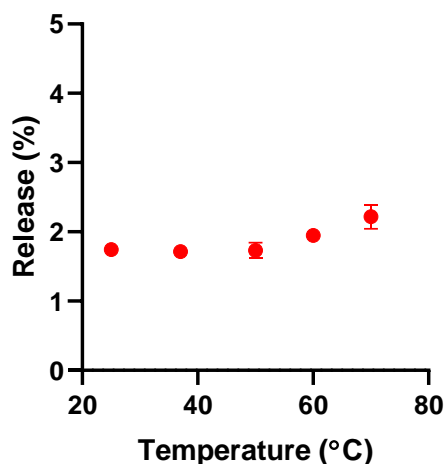


**Figure 22 – The release profile of RAN dePFHnD at various temperatures. Each point represents the mean of n = 3 replicates with error bars representing the standard deviation.**

This observation validates the laser release studies (Figure 20), where vaporization is not sufficient for substantial release as the dePFHnDs are heated past the bulk boiling point of PFH (56°C). As a result, the mechanical component of HIFU exposure likely plays a vital role in achieving greater release of the model drug.

Furthermore, the dePFHnDs exhibit minimal increase in size and leakage of the cargo over time (Figure 23).

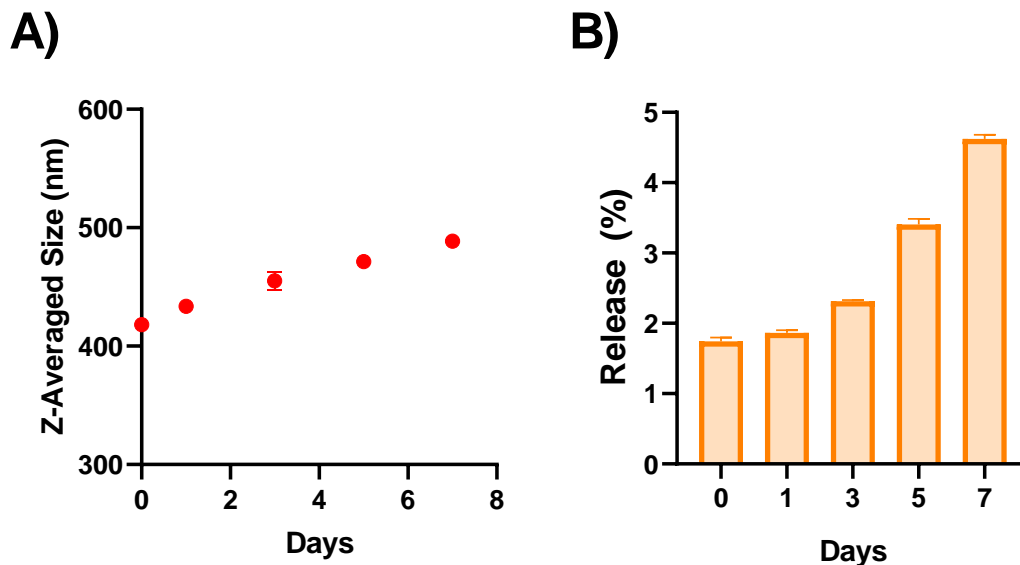


**Figure 23 – A) The change in z-average size over the course of several days as taken by DLS. B) The release of calcein measured as a percentage of the total encapsulated amount over the course of 8 days. Each measurement is an average of  $n = 3$  replicates with the error bars representing standard deviation.**

The increase in size is observed in standard PFCnDs and is commonly attributed to Ostwald ripening.<sup>96</sup> This behavior is like exacerbated by the fact that dePFHnDs are larger than typical PFCnDs and are more susceptible to coalescing, which could result in the release of calcein over the course of several days.

### 5.3.3 Delivery of Poly I:C

After validation of both the encapsulation and release of a model drug, a double stranded RNA mimic, poly I:C, was loaded into the double emulsion nanodroplet. Poly I:C is utilized as an adjuvant and is recognized by toll-like receptor 3 (TLR3), leading to the downstream activation of NF-kappaB; this results in the expression of inducible nitric-oxide synthase and the production of nitric oxide.<sup>97</sup> Nitric oxide is then oxidized to produce nitrite, which can be detected utilizing a colorimetric Greiss assay. To determine if the

process of encapsulation and release impacted the poly I:C, gel electrophoresis was used to both confirm release of poly I:C through HIFU and determine if the process resulted in fragmentation (Figure 24 A).

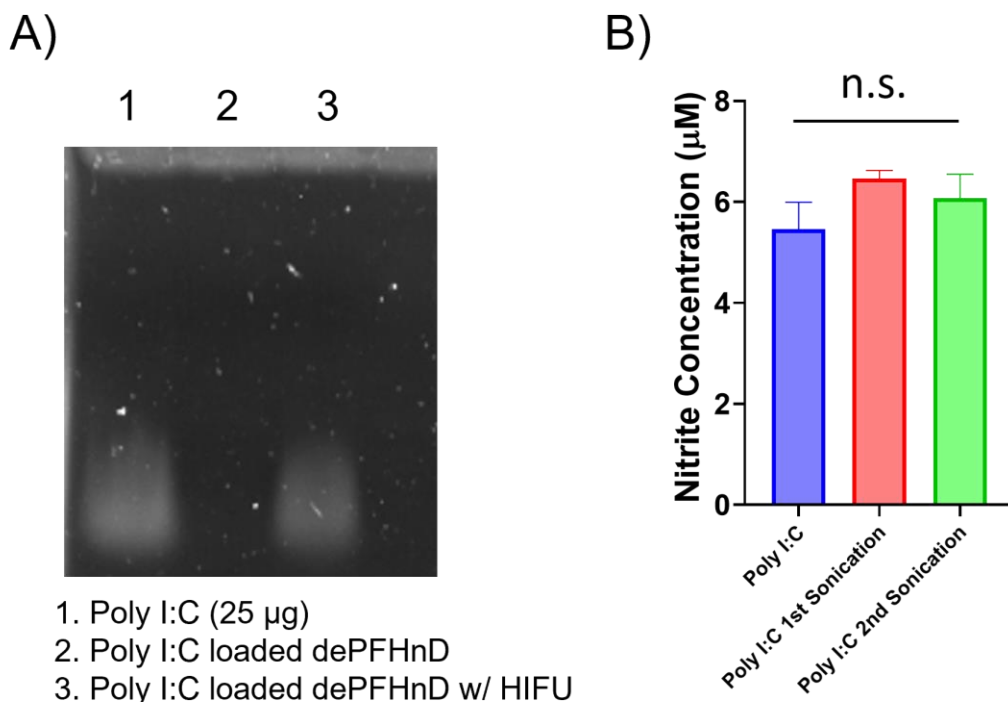


**Figure 24 – A) Agarose gel electrophoresis of poly I:C loaded into dePFHnDs and subjected to HIFU (PNP: 2.16 MPa, PRI: 15ms, duration 5 minute) in comparison to unprocessed poly I:C. The released poly I:C shows no signs of degradation. B) The activity of poly I:C remains unchanged after the two probe sonication steps needed to produce dePFHnDs, as indicated in the Greiss assay. Bar plots represent the mean, while the error bars represent the standard deviation of  $n = 3$  replicates. N.S. represents not significant (one-way ANOVA  $F(2, 6) = 4.242$ ,  $p = 0.0711 > 0.05$ ).**

dePFHnDs loaded with poly I:C and not exposed to HIFU showed no band, confirming that the band observed in dePFHnDs exposed to HIFU resulted from released poly I:C and not from poly I:C that adhered to the particle surface. Activity of the poly I:C after probe sonication the two round of probe sonication required to form the dePFHnD was confirmed through griess assay (Figure 24 B). Probe sonication would subject the therapeutics to

acoustic cavitation along with hydrodynamic shearing that could result in the fragmentation<sup>98</sup> or even destruction of delicate nucleic acid based therapeutics such as mRNA. The relatively short duration in the probe sonication along with the double stranded nature of poly I:C, likely conferring greater stability to the molecule, allowed for minimal damage and fragmentation of the poly I:C. This process may limit the therapeutic applications of the particle and future work should investigate alternative formulation processes that could allow for encapsulation of more delicate therapeutics.

As HIFU exposure and probe sonication resulted in minimal fragmentation and had no impact upon the therapeutic activity of the poly I:C, dePFHnDs loaded with poly I:C were then exposed to HIFU and the resulting solution was incubated with RAW 264.7 macrophages to determine if the release could trigger production of nitrite (Figure 25).

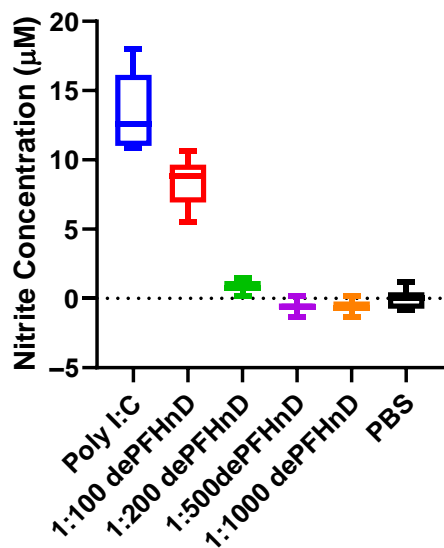


**Figure 25 – Griess assay of dePFHnD exposed to HIFU (PNP: 2.16 MPa, PRI: 15 ms, duration: 5 minutes) and incubated with RAW 264.7 macrophages (N = 8) at different concentrations of the dePFHnD. Statistically significant differences in the mean were detected (one-way ANOVA,  $p < 0.0001$ ) with significant differences detected between 1:100 dePFHnD and PBS (Tukey’s multiple comparison,  $p < 0.0001$ ).**

dePFHnDs that were exposed to HIFU exhibited an increase in production of nitrite at the highest concentration (Tukey's multiple comparison,  $p < 0.0001$ ). This validates that the poly I:C was not fragmented or destroyed during the process of formulation of the dePFHnD or from the release, and that the fragments of the dePFHnD do not inhibit the activity of poly I:C. However, it does suggest that the stimulation of the macrophages is non-linear with relation to the poly I:C concentration. To further simulate a more realistic situation, RAW 264.7 macrophages were seeded in a film bottom well plate and incubated with dePFHnDs encapsulating poly I:C (Figure 26 A). Select wells were exposed to HIFU, and the nitrite production was quantified (Figure 26 B).

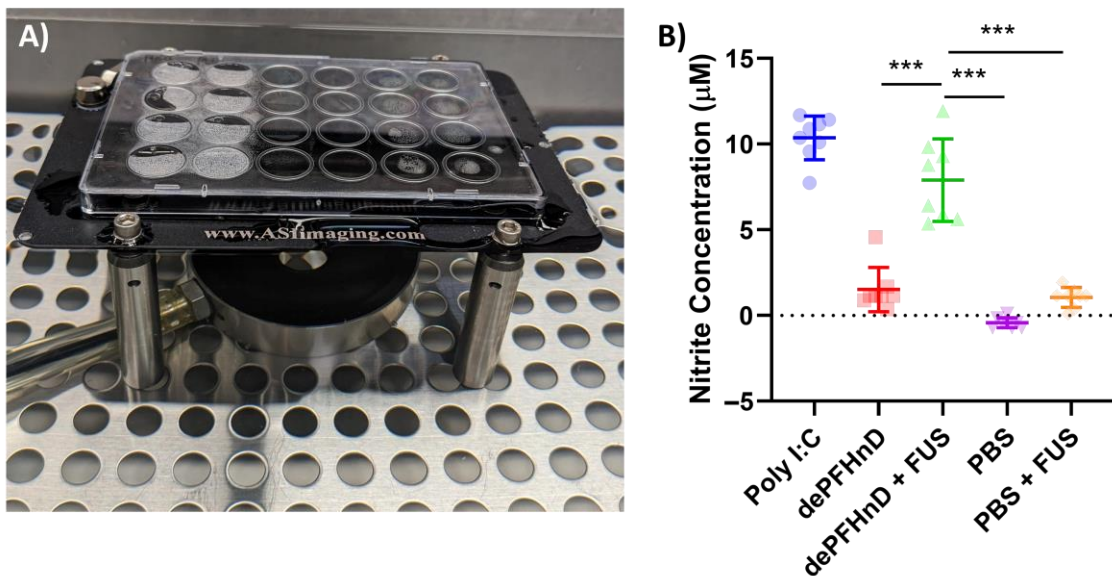


**Figure 26 – A) Image of the setup utilized to hold a film bottom 24 well plate to allow for FUS exposure from the bottom in a water bath held at 37°C. B) Nitrite generated from the RAW 264.7 macrophages that were incubated with poly I:C alone (0.1mg/mL), dePFHnDs, dePFHnDs and exposed to FUS (PNP: 1.08 MPa, PRI: 15 ms, duration: 5 minutes), PBS, and PBS with FUS exposure with n = 8 replicates. Differences in the mean were observed (one-way ANOVA,  $F(4, 35) = 94.69$ ,  $P < 0.0001$ ) with significant differences detected between dePFHnD + FUS and all other groups (Tukey's multiple comparison,  $p < 0.0001$  represented by \*\*\*).**

Exposure of the cells to dePFHnDs in tandem with FUS led to increased production of nitrite (Tukey's multiple comparison,  $p < 0.0001$ ) compared to just the dePFHnDs alone, PBS, and PBS with FUS. This is definitive evidence that hydrophilic, therapeutic cargo can be encapsulated within dePFHnDs and delivered to cells without compromising therapeutic activity. While the stimulation of the macrophages seems slightly subdued compared to using only poly I:C, this is due to the difficulty in quantifying the release of poly I:C release from the dePFHnDs. Therefore, a rough estimation of the release was made by adding naked poly I:C. Another factor of consideration is that the intensity of the FUS was limited to prevent the detaching and loss of cells at the focal point of the beam. This limited the release efficiency that could be utilized in this in vitro study. For studies in tissue, a higher mechanical index could be used to stimulate greater release of the dePFHnDs.

#### 5.3.4 PA Trackability

As mentioned earlier, the dePFHnDs exhibit limited release upon lasing, which could allow for PA tracking and monitoring of the particles without impacting the therapeutic release. Previous approaches present no method for non-disruptive imaging and tracking.<sup>27,33</sup> Thus, it would be beneficial to quantify the amount of drug-loaded particles that have entered the treatment site and be able to monitor the extent of drug release during the treatment. To demonstrate this ability, dePFHnDs were exposed to different HIFU conditions that correlated with different release percentages, which were then inserted into a tube phantom and imaged using USPA (Figure 27).

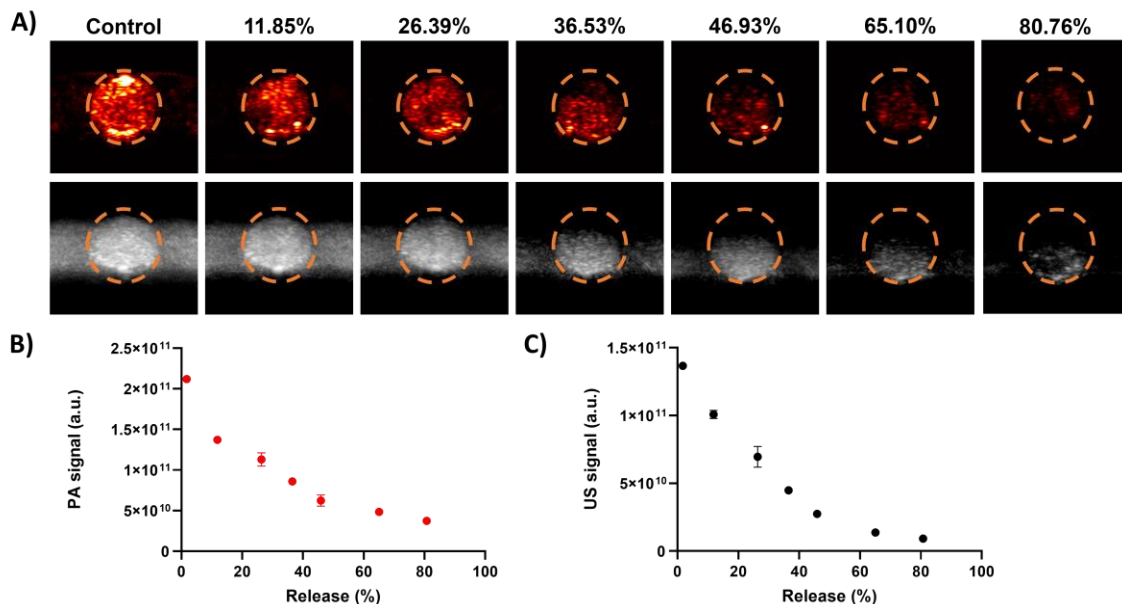


**Figure 27 – A) US and PA images of dePFHnDs after exposure to HIFU of varying conditions and the resulting release percentages at each point. B) Integrated PA intensity of the dePFHnDs at different release points. C) Integrated US intensity at different release points.**

The dePFHnDs exhibit a monotonic decrease in PA intensity and US signal as more of the model drug was released. As the dePFHnDs are exposed to greater intensities and durations, they are likely destroyed, causing release of drug and reduction of US/PA intensity. This suggests that the particles can be imaged in real-time to obtain during the treatment to estimate the number of particles and drug released based upon the initial PA signal and changes in US and PA signal after HIFU exposure. The ability to utilize both PA and US signal can allow for exclusion of signal generated from endogenous absorbers and background US signal to better identify dePFHnD signals. Longitudinal tracking can allow for better isolation of the dePFHnD signal as it should present a decay.

## 5.4 Conclusion

In this chapter, dePFHnDs were optimized for greater encapsulation efficiency through fluorosurfactant selection and concentration variation. The release through lasing and FUS exposure was characterized to validate release-free tracking of the particles and optimized FUS settings to initiate the delivery of the drugs. Using this platform, poly I:C, a synthetic dsRNA mimic that can be used as a vaccine adjuvant, was encapsulated and released with FUS stimulation. The adjuvant retained therapeutic activity and showed no signs of fragmentation. The development of these particles could allow for real-time tracking and qualitative estimation of the number of nanoparticles that arrive at the target site and the subsequent release fraction after HIFU triggered release. Future efforts should focus on the development of a more biocompatible fluorosurfactant or improved synthesis methods that can be used to restrict excess fluorosurfactant from incorporating onto the outer shell.

## CHAPTER 6. FUTURE WORKS

As is often the case, scientific research is never completed, and there are always numerous additional avenues to explore. In this section, some possible future directions will be discussed along with observations that warrant further examination. This section will be broken up based upon each chapter.

### 6.1 Repeated Optical Nanodroplet Vaporization

In CHAPTER 3, the behavior of repeated nanodroplets vaporization is described and the impact of different variables such as nanodroplet shell, lasing PRF, environment, and PFC core are described. Through the characterization of these behaviors other observations have been noted.

#### 6.1.1 High Fluence Suppression

When the nanodroplets are lased at high fluences at around 90-100 mJ/cm<sup>2</sup>, the nanodroplet vaporization appears suppressed. As fluence is ramped up from 0 – 70 mJ/cm<sup>2</sup>, the nanodroplets exhibit an expected response where the US contrast increases once the threshold is surpassed and then reaches a saturation point, where maximal US contrast observed. This behavior is as expected since the nanodroplets have reached a point in which all the nanodroplets that can vaporize do vaporize and higher energy will not increase the number of microbubbles that are generated. It is possible that higher fluence can be converted into higher temperatures that would result in greater expansion of the microbubbles. However, it is often observed that above this fluence, the nanodroplets start exhibiting a decrease in US contrast. In earlier studies, the nanodroplets are lased with an

initial ramp up (0 – 100 mJ/cm<sup>2</sup>) with 3 pulses at each fluence with intervals of ~10 mJ/cm<sup>2</sup> between each fluence, followed by 10 pulses at a max fluence of 100 mJ/cm<sup>2</sup> and then a ramp down composed of three pulses at each fluence with intervals of ~10 mJ/cm<sup>2</sup> between each fluence. During these studies, nanodroplets would exhibit an increasing fluence up to around 70 mJ/cm<sup>2</sup>, after which the US contrast would decrease at around 80-90 mJ/cm<sup>2</sup>. This was sustained during the repeated lasing at 100 mJ/cm<sup>2</sup>. Surprisingly, the US signal recovers during the ramp down following the repeated lasing. This suggests that contrast reduction is not due to nanodroplet destruction, but to the high lasing itself. Furthermore, the PA signal exhibits a linear increase, which rules out the possibility of issues with the laser energy. This behavior was also observed after swapping the lasing from fiber bundles to air beam. While the exact explanation for this behavior is unclear, one potential explanation is that the high pressure generated due to the high laser fluence suppresses the nanodroplet vaporization.

This observation would likely have limited impact on the vaporization of nanodroplets, because the phenomenon is most observed at high fluences (>70 mJ/cm<sup>2</sup>); these values are near the ANSI laser safety limit (100 mJ/cm<sup>2</sup>) for lasers operating at 1064 nm at a PRF of 10 Hz. Due to how light scatters in tissue, exposure to fluence high enough to result in suppression would only occur directly under the fibers, with the fluence quickly falling off to lower levels.

However, the phenomenon should be examined to better understand the underlying nanodroplet physics, and high fluence suppression may impact the ability to detect the nanodroplets at low depths where the fluence is much higher due to reduced scattering.

Future studies should aim to better characterize the factors that influence the behavior and methods to mitigate the suppression.

### *6.1.2 Vaporization Thresholds of Very High Boiling Point PFC and Differential Dye Loading*

The initial examination of different high boiling point PFC showed that most repeated ODV nanodroplets (PFP, PFH, and PFHept) showed some correlation of the vaporization threshold with the critical temperature of the PFC core. Other attempts were made to examine the ODV threshold for even higher boiling point PFC such as perfluorooctane (PFO, boiling point: 103°C), perfluorooctyl bromide (PFBr, boiling point: 142°C), and perfluorodecalin (PFD, boiling point: 142°C). Preliminary results indicate that nanodroplets exhibited surprisingly low vaporization thresholds, which contradicted literature of higher ADV thresholds for those PFCs. Some of the nanodroplets (PFBr and PFD) were synthesized at lower concentrations ( $\sim 10^{11}$  nanodroplets/mL compared to  $\sim 10^{12}$  nanodroplets/mL for PFH), smaller sizes ( $\sim 200$  nm compared to  $\sim 300$  nm), and higher dye concentrations. This made it quite difficult to tease out specific differences and identify the effect of the cores by themselves. An attempt was made to examine this further by reducing the amount of dye in the nanodroplets from 0.5 mg/mL of lipid solution to 0.2 mg/mL of lipid solution. However, this change did not result in any change. While perplexing, a similar observation has been described before with differential loading of nanodroplets.

This fundamental behaviour could be better studied by more precisely synthesizing the nanodroplets to be similar sizes and encapsulate similar amounts of photoabsorber. This can be accomplished either through microfluidics, in which the exact size of the emulsion

can be finely tuned and the amount of photoabsorber can be loaded with greater precision, or through extrusion of the nanodroplets followed by chemical conjugation of photoabsorber on to the surface, where the amount of chemical linkers on the nanodroplets can be made to be uniform between samples. This work would be vital to better understanding the exact process by which ODV occurs. Current explanations are primarily based upon homogeneous nucleation from heating of the nanodroplets from the photoabsorber and do not account for the photoacoustic pressure from the dye.

### *6.1.3 Preconditioning for Multiplexing*

Briefly described in 3.3.1, preconditioning occurs during the initial laser pulses where nanodroplets generate less US contrast that gradually increases after more laser exposure, and this behavior is impacted by the dye used in the nanodroplet. This change in behavior could be leveraged for improved in vivo performance. The change in behaviour could be used to identify the nanodroplets and isolate them from the background signal.

The fact that different dyes exhibit different preconditioning behaviors can be used to differentiate different nanodroplets. Previously, Santiesteban et al. utilized different laser wavelengths to differentiate two different dye used to vaporize different sub-populations of nanodroplets.<sup>99</sup> Preconditioning behavior could be utilized to differentiate between two dyes that would absorb at the same wavelength. For example, both Epolight 3072 and IR1048 can result in vaporization of PFH nanodroplets after being lased at 1064 nm. However, Epolight 3072 has a short preconditioning period (~5 pulses), while IR1048 has a longer preconditioning period (200 pulses; Figure 30). This can allow for the differentiation of different nanodroplet populations that are activated at the same

wavelength. If the preconditioning phenomenon is consistent among Epolight and IR dyes, then it would be possible to differentiate between four different sub-populations of nanodroplets using those dyes (Figure 28).

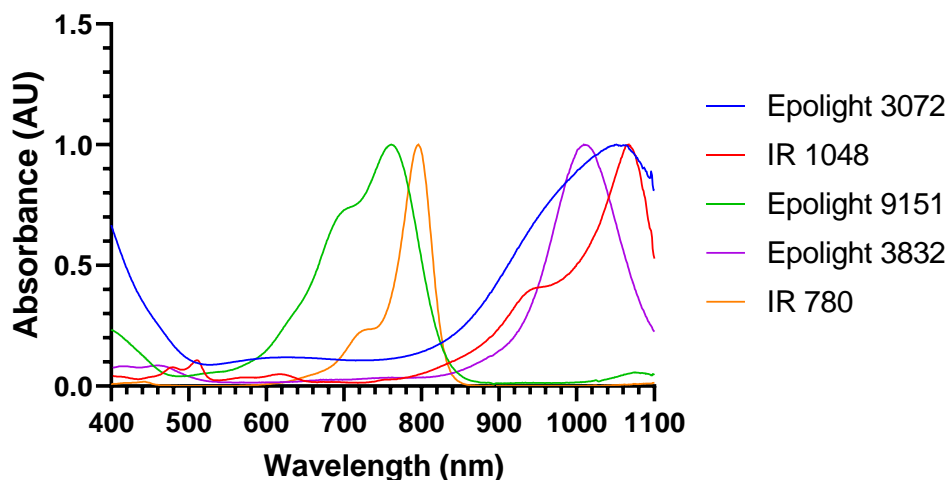


**Figure 28 – The normalized absorbance spectrum of near-IR dyes dissolved in chloroform that exhibit peak absorptions around 775 nm and 1064 nm. These could be candidates for dyes that could be used in nanodroplet formulations that would allow for multiplexing.**

IR780 and Epolight 9151 could be candidates for multiplexing based on preconditioning at 775 nm. Future works can utilize a live algorithm to differentiate between the behaviors.

#### 6.1.4 Condensation Synthesis of High Boiling Point Perfluorocarbon Nanodroplets

In this study, nanodroplets are primarily synthesized through the use of probe sonication, which results in the stochastic formation of varying population of nanodroplets.<sup>100</sup> For these nanodroplets, the lipid shell completely coats the perfluorocarbon layer and helps stabilize the particle, coalescing of the nanodroplets through Ostwald ripening. Once these droplets are vaporized, they undergo up to a five-fold expansion in volume that will result in exposed water and perfluorocarbon interface,

which could impact the longevity of the resulting microbubble and repeatability of the vaporization process.

An alternative approach takes low-boiling point perfluorocarbons and generates lipid-coated microbubbles. These are then exposed to high pressures and low temperatures to condense the microbubbles down to nanodroplets. It has been suggested that the lipid shells fold in on the surface of the nanodroplets. Nanodroplets formed using this method with high-boiling point perfluorocarbon might produce more stable microbubbles after vaporization and the nanodroplets may better tolerate repeated vaporization. The main hurdles to the approach are as follows: loading of dye into microbubbles is limited and high-boiling point perfluorocarbons would require high temperatures to ensure that they retain their gaseous state to create microbubbles. The dye issue could be bypassed through chemical conjugation of near-infrared absorbing dyes or nanoparticles to the surface of the microbubble, though this could increase the vaporization threshold and limit the dye choices. For practical reasons, only perfluorocarbons such as perfluorohexane and perfluoroheptane could be used as even higher-boiling point perfluorocarbons such as perfluorooctane would require temperatures that exceed the boiling point of water.

#### *6.1.5 Vaporization Threshold Tuning Through Shell Engineering*

It was shown that the shell material impacts the vaporization threshold independent of dye loading (Figure 5). This suggests that the shell surface tension or intermolecular forces within the shell could impact the vaporization threshold. Further work could be done to tease out the threshold through direct measurements of the interfacial tension, as the

work presented here only utilized literature values. This highlights the possibility of tuning the vaporization threshold through different lipid shell optimizations.

## **6.2 Laser Induced Sonoporation**

In Chapter 4, laser induced sonoporation through the use of repeated ODV

### *6.2.1 Formulation Variation*

Sonoporation appears to be greatly influenced by the dye encapsulated within the nanodroplet, with IR1048 producing the highest sonoporation rate in comparison to Epolight 3072. It is possible that this behavior is influenced by preconditioning and that other dyes may provide more ideal methods for sonoporating cells. A deeper understanding of this behaviour could elucidate the mechanism for sonoporation that could allow for delivery of therapeutic cargo of larger sizes without high fluences and impacting viability.

Furthermore, it was determined that high fluences resulted in both substantial dislodging of cells and cell death. However, the sonoporation rate of the remaining cells and delivery amount was improved. It is possible that this response could be modulated by changing the internal core of the PFCnDs utilized in sonoporation. This could result in less destructive vaporization, while still obtaining the high delivery efficiencies. Higher boiling point perfluorocarbons such as PFHept and PFO should be investigated.

### *6.2.2 Impact of Proximity of the Particle on Sonoporation*

Future studies could examine the impact of proximity between the particle and the cell membrane. Given that concentration has a substantial impact on the sonoporation rate

and the sonoporation rate falls off dramatically as concentration decreases, it may be possible to locally increase the concentration of the nanodroplets by decorating the cells. This would minimize the amount of nanodroplets that would need to be administered and reducing the potential for toxicity.

### **6.3 Double Emulsion Nanodroplets**

In CHAPTER 5, double emulsion nanodroplets were introduced and optimized to improve encapsulation efficiency and release efficiency. These particles can be utilized to encapsulate a variety of different hydrophilic and hydrophobic molecules.

#### *6.3.1 Improving Release*

In the course of characterizing the dePFHnDs, different HIFU conditions were examined such as PNP, PRI, duty cycle, and duration. Ideal delivery conditions were identified that minimized the impact on the cells while still enabling release of the drugs from the particle. However, they still require a high intensity and long duration. One aspect of the release that has not been explored is the release efficiency in response to the frequency of the HIFU. As it was shown that heat-based stimulation from lasing and direct heating does not result in release, lower frequencies of HIFU could be utilized that emphasized the mechanical effect such as cavitation to better initiate release. If successful, this would also allow for delivery of the therapeutic at deeper depths due to reduced attenuation compared to higher frequencies.

#### *6.3.2 Develop More Biocompatible and Optimized Fluorosurfactant*

Multiple commercially available fluorosurfactants were utilized to synthesize a variety of different formulations of dePFHnDs. The fluorosurfactants impact the size of the resulting emulsion with FSL yielding dePFHnDs with a z-average size of ~400 nm while RAN yields dePFHnDs with a z-average size of ~500 nm. Unfortunately, the Ran surfactants is proprietary and it is unclear what properties of each surfactant impart this size discrepancy. Synthesizing de novo fluorosurfactants can allow for a more comprehensive examination of what factors impact the resulting size.

At low concentrations the fluorosurfactants exhibit minimal toxicity, but high concentrations of the surfactants are required to produce dePFHnDs that encapsulate a suitable amount of drug for therapeutic effect. At these higher concentrations, toxicity is more evident in the two formulations listed in this dissertation (Figure 19 and Figure 37). However, these fluorosurfactants could be engineered to be more biocompatible at higher concentrations to avoid any unintended toxicity.

### 6.3.3 *Synthesis Utilizing Microfluidics*

dePFHnDs were produced utilizing probe sonication to produce both the first emulsion and the second emulsion. These processes produce particles with a wide range of sizes. The larger particles are filtered out through centrifugation, and consequently, some of the encapsulated drugs are lost. In addition, sonication to form the second emulsion destroys some of the primary emulsion particles, resulting in the release of therapeutics within the primary emulsion. These processes both contribute to the relatively low encapsulation efficiency (~8%), which could be problematic for encapsulating costly

therapeutics. Attempts were made to reduce the size of the larger particles through extrusion, however, this was inconsistent and destroyed some of the droplets.

In addition, probe sonication would likely destroy more delicate therapeutics such as mRNA or proteins. Future studies should examine the possibility of utilizing microfluidics create these double emulsion particles. Previous studies have developed acoustically activatable double emulsion microparticles.<sup>93,101</sup> With further tinkering, the nozzles could be engineered to produce nanoscale particles.<sup>102</sup> These not only provide the benefit of size control and consistency, but also the process is “gentler” on the therapeutic itself, allowing for the encapsulation of more delicate therapeutics such as mRNA, siRNA, and proteins. Alternatives could utilize microfluidics to sort the particles with greater accuracy than centrifugation.

# APPENDIX A. SUPPLEMENTARY INFORMATION FOR CHAPTER 3: OPTICAL VAPORIZATION THRESHOLD CHARACTERIZATION

This appendix encapsulates supplementary information for CHAPTER 3.

## A.1 Dye Standard for Quantifying Concentration within the Nanodroplets

The amount of Epolight 3072 dye in each formulation of nanodroplets was quantified utilizing a standard of created with known quantities of Epolight 3072 dissolved in chloroform (Figure 29 A). The peak absorption (1060 nm) was then plotted against the concentration to determine the linear relationship between the absorbance and the concentration (Figure 29 B), which was used to calculate the concentration in the lyophilized samples.

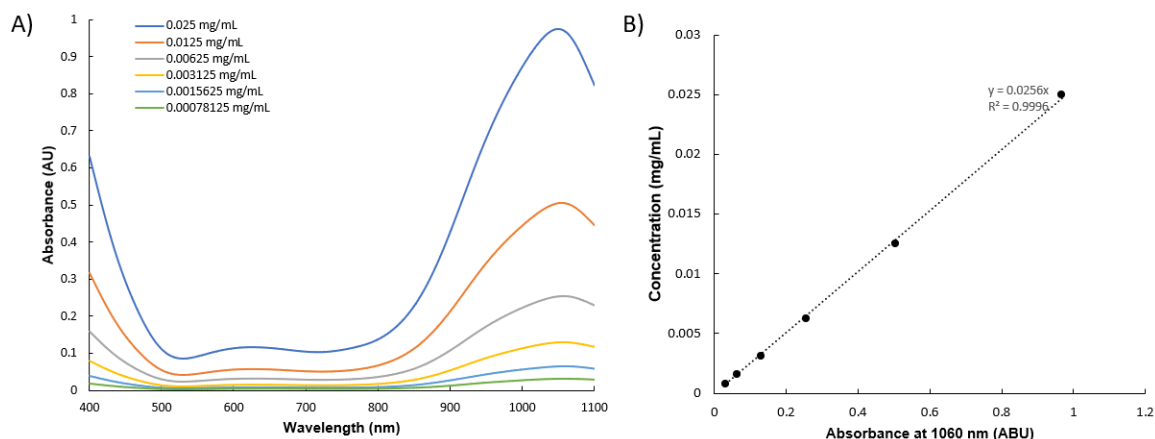


**Figure 29 – A) The UV-vis spectra of Epolight 3072 dissolved in chloroform at different concentrations and B) the resulting standard for the absorbance at 1060 nm relative to the concentration of the dye.**

## A.2 Nanoparticle Size and Material Properties PFC

**Table 2 Size and Composition of the Nanodroplets**

Core Material	Dye	Shell Material	Z-average size	Polydispersity index (PDI)
Perfluoropentane	Epolight 3072	Lipid	308.97	0.211
Perfluorohexane	Epolight 3072	Lipid	293.6	0.185
Perfluoroheptane	Epolight 3072	Lipid	265.13	0.248
Perfluorohexane	Epolight 3072	BSA	314.1	0.186
Perfluorohexane	Epolight 3072	Zonyl	285.8	0.167

**Table 3 Critical Temperature of Cores Used in Nanodroplets**

Perfluorocarbon	Chemical Formula	Critical Temperature (K)	Boiling Point (K)
Perfluoropentane	C <sub>5</sub> F <sub>12</sub>	421.9 <sup>a</sup>	302.15
Perfluorohexane	C <sub>6</sub> F <sub>14</sub>	448.77 <sup>b</sup>	329.15
Perfluoroheptane	C <sub>7</sub> F <sub>16</sub>	475 <sup>c</sup>	353.15

<sup>a</sup>From<sup>103</sup>; <sup>b</sup> From <sup>104</sup>; <sup>c</sup> From <sup>105</sup>

### A.3 Preconditioning Comparison

PFHnDs encapsulating two different dyes (IR1048 and Epolight 3072) were compared by lasing each formulation for 1000 pulses (**Error! Reference source not found.**).

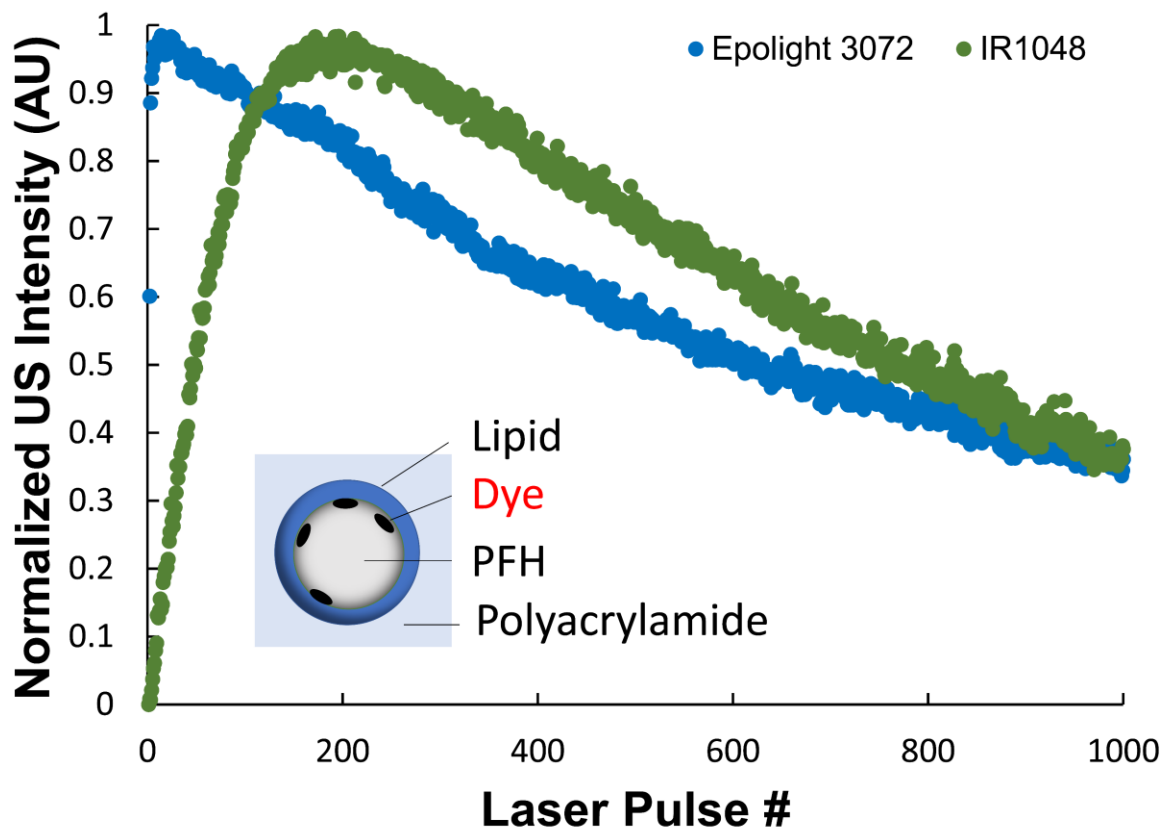
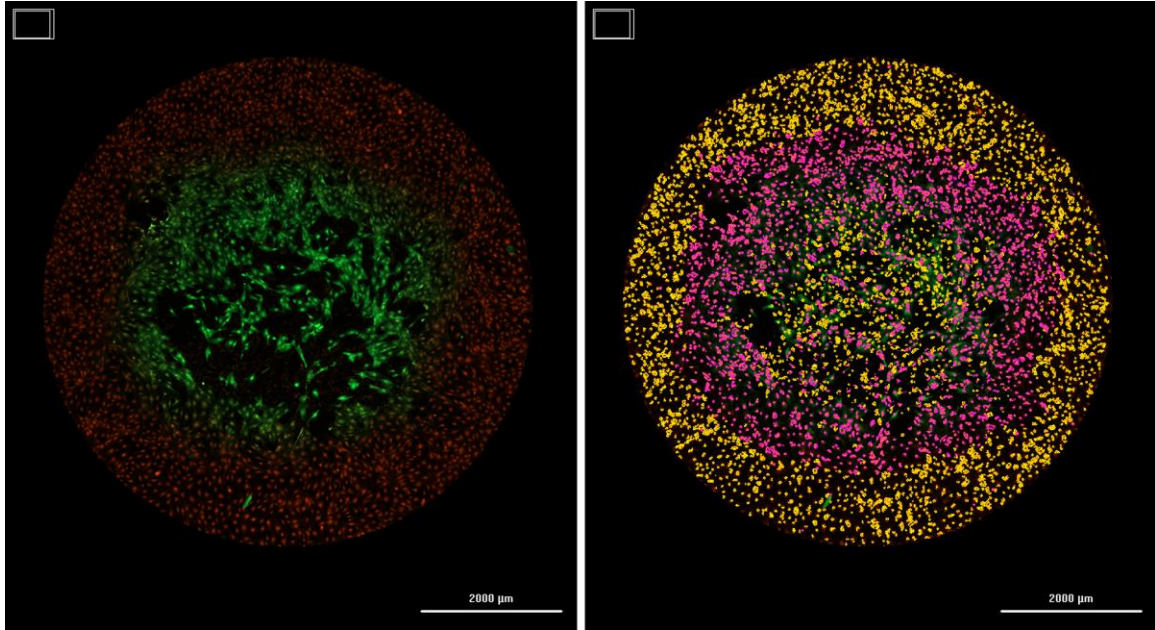


Figure 30 – The preconditioning behavior of PFHnDs based upon the different dye. The droplets were embedded in a polyacrylamide and lased for multiple pulses at 75 mJ/cm<sup>2</sup>.

**APPENDIX B. SUPPLEMENTARY INFORMATION FOR  
CHAPTER 4: SONOPORATION**

This appendix encapsulates supplemental information for Chapter 4.



**Figure 31 – An example of the data process is shown. The ROI is defined by the size of the laser beam (diameter: 7 mm). Live cells are defined by having calcein red-orange fluorescence intensity greater than 1.5x the background and sonoporated cells are defined by having fluorescence intensity that is 1.5x the background. The image on the right shows the classification of all cells identified by Hoechst 33342 in yellow. The subpopulation of live sonoporated cells is shown in pink.**

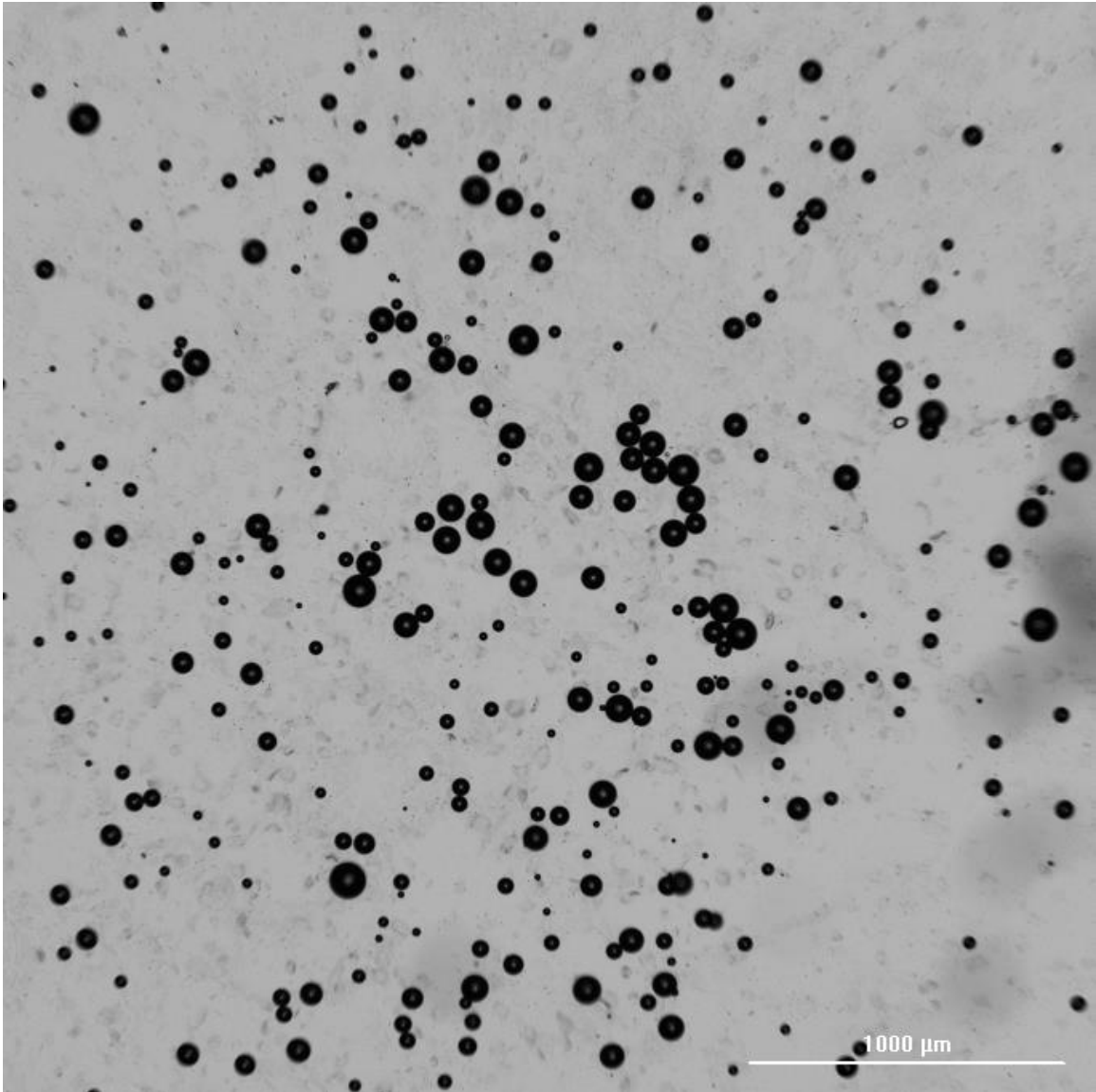
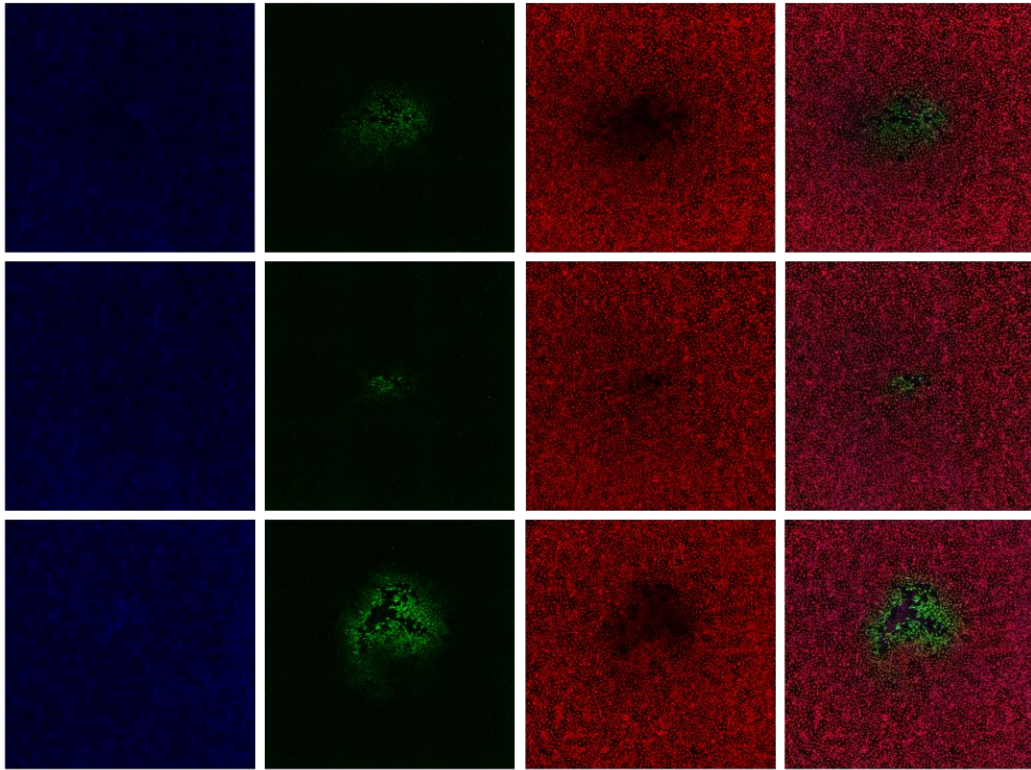


**Figure 32 – Brightfield image showing the accumulation of microbubbles after repeated lasing for 600 pulses.**

### **A.1 Stitched Images Comparing PFHnDs Formulated with Different Dyes**

Epolight 3072



IR1048

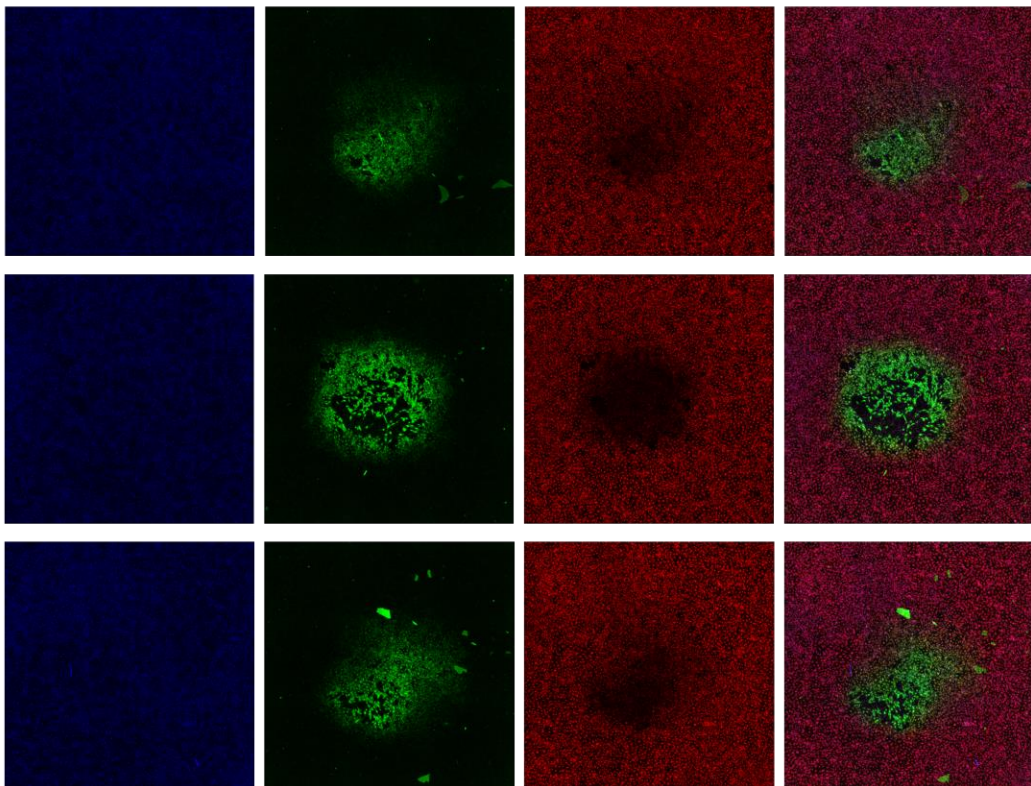


**Figure 33 – All samples analyzed to compare the different dyes (Epolight 3072 and IR1048) used in this study. Conditions are as follows: PFH concentration:  $3 \times 10^{10}$  particles/mL, laser fluence:  $60 \text{ mJ/cm}^2$ , 100 pulses.**

### **A.2 Stitched Images of Fluorescent Dextran Bead Delivery**

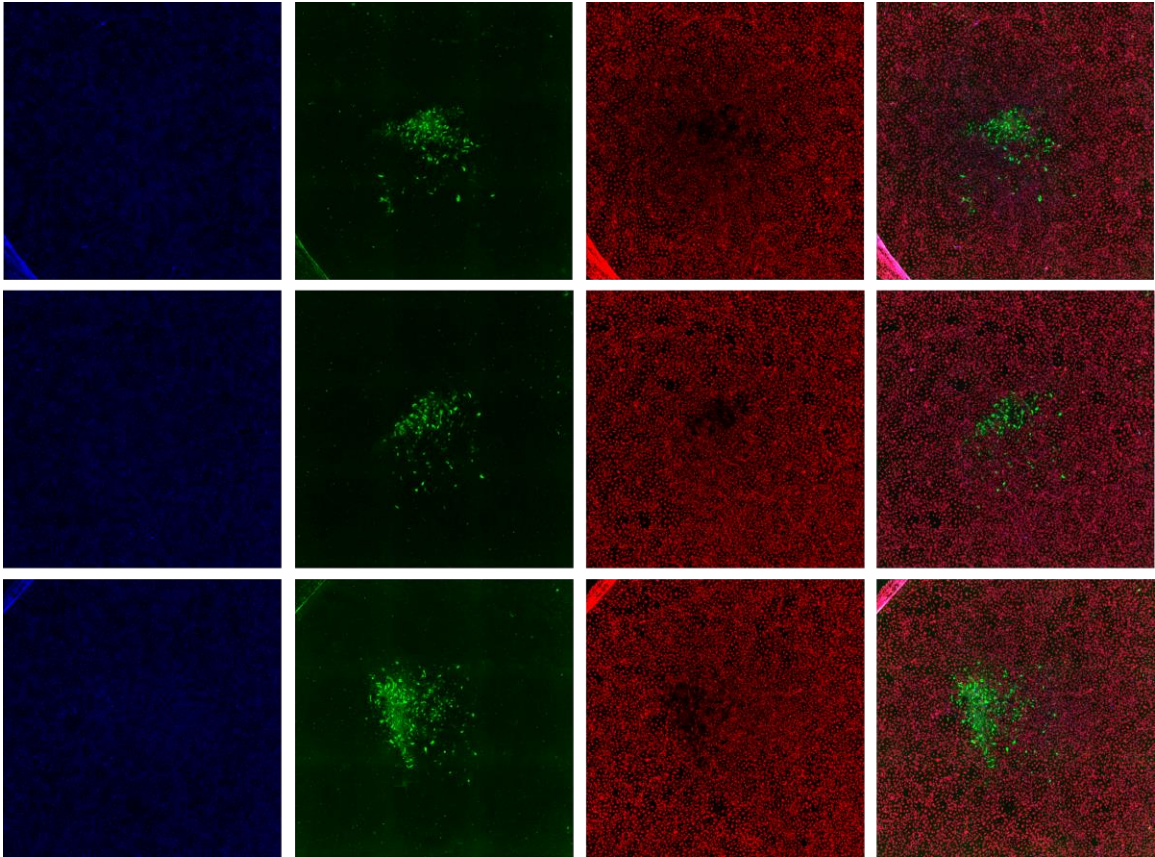


**Figure 34 – All HADMSC cells incubated with FITC-tagged dextran beads (3-5kDa). From left to right: Hoechst, Calcein, Calcein Red-Orange am, merge. Laser settings are as follows:  $60 \text{ mJ/cm}^2$ ; 300 pulses.**

## APPENDIX C. SUPPLEMENTARY INFORMATION FOR CHAPTER 5: DOUBLE EMULSION CHARACTERIZATION

This appendix encapsulates supplemental information for Chapter 5.

### A.1 Concentration Standards

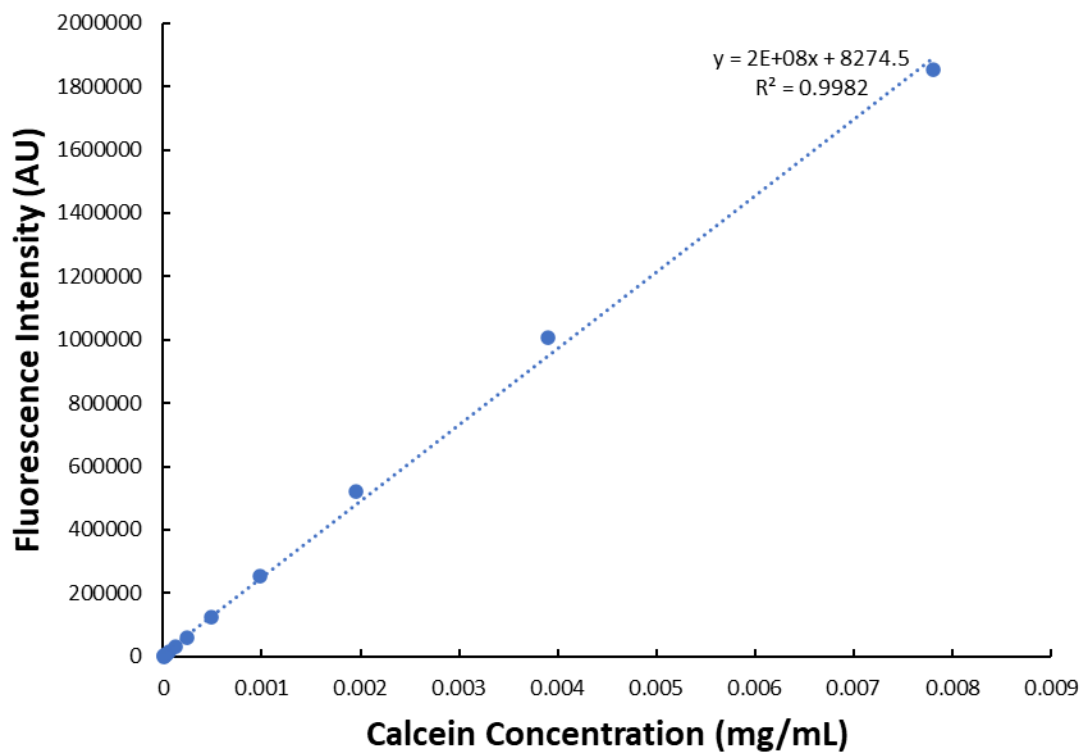


**Figure 35 – Calcein standard utilized to convert fluorescence intensity to concentration of calcein.**

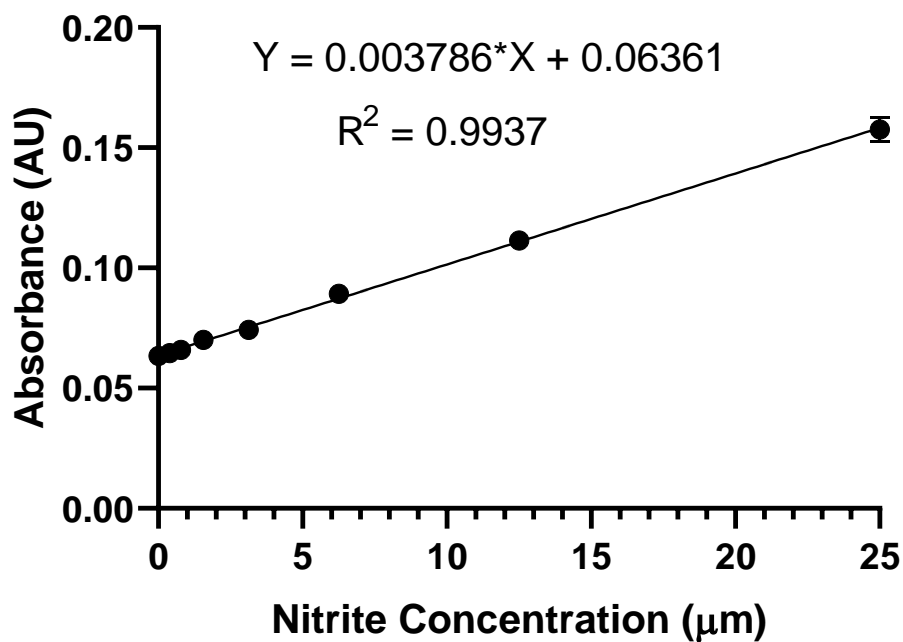


**Figure 36 – The nitrite standard that was used to determine the amount of nitrite that was generated during the griess assay.**

## **A.2 FSL dePFHnD Characterization**

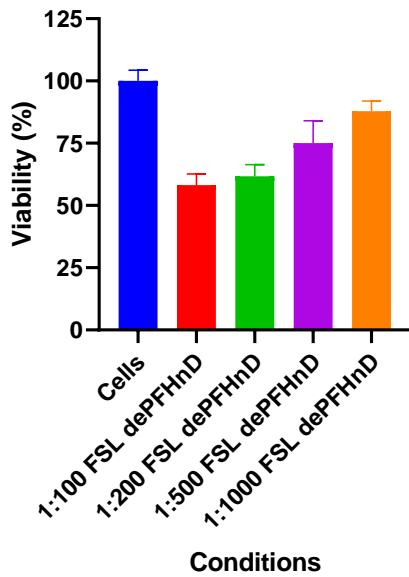


Figure 37 – The viability of RAW 264.7 cells incubated with different concentrations of dePFHnDs formulated with FSL. Each bar represents the mean of n=6 replicates with the error bars representing standard deviation.

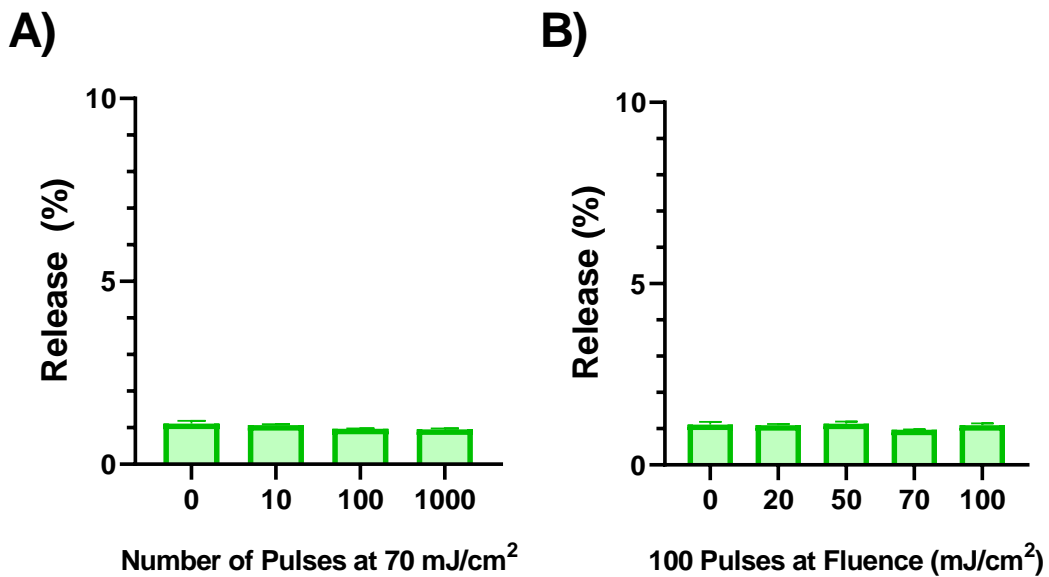
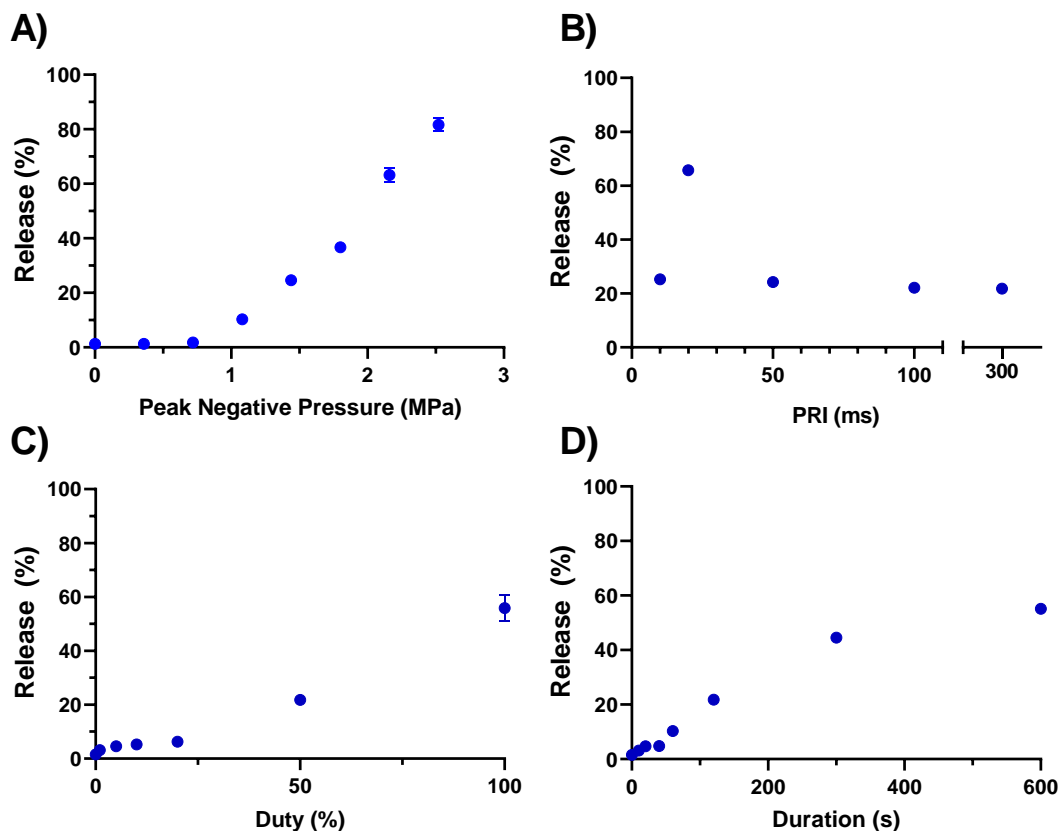


Figure 38 – The release efficiency of dePFHnDs formulated with FSL after A) repeated lasing at 70 mJ/cm<sup>2</sup> and B) after lasing at various fluences.



**Figure 39 – The release efficiency of FSL dePFHnDs as a function of A) peak negative pressure (PNP), B) pulse repetition interval (PRI), C) duty cycle, and D) duration at different PNPs. All experiments were conducted under the following conditions, except for the condition being tested: PNP: 1.44 MPa, duty cycle: 50%, PRI: 300 ms, and duration 120 s. Each point represents the mean while the error bars indicate the standard deviation of  $n = 3$  replicates.**

### A.3 Confocal Validation of the Double Emulsion

In order to, validate the encapsulation of both hydrophobic and hydrophilic molecules, calcein was encapsulated within the inner emulsion and cyanine3 (Cy3) was embedded within the F-68 shell. This would allow for visualization of the two different dyes. dePFHnDs loaded with calcein and cy3 exhibited a z-averaged size of 392.1 nm (Figure 40 A). To allow for uptake by cells and immobilization of the particles, they were

incubated with PEI, polyethylenimine, which is a cationic polymer that is often used for nonviral nucleic acid delivery.<sup>106</sup> This led to an increase in size to 502.9 nm (Figure 40 A) and increased the zeta potential from -39.93 to 41.5 (Figure 40 B). As the surface of the FSL dePFHnDs are negatively charged, the addition of positively charged PEI, resulting in an increase in charge and size.

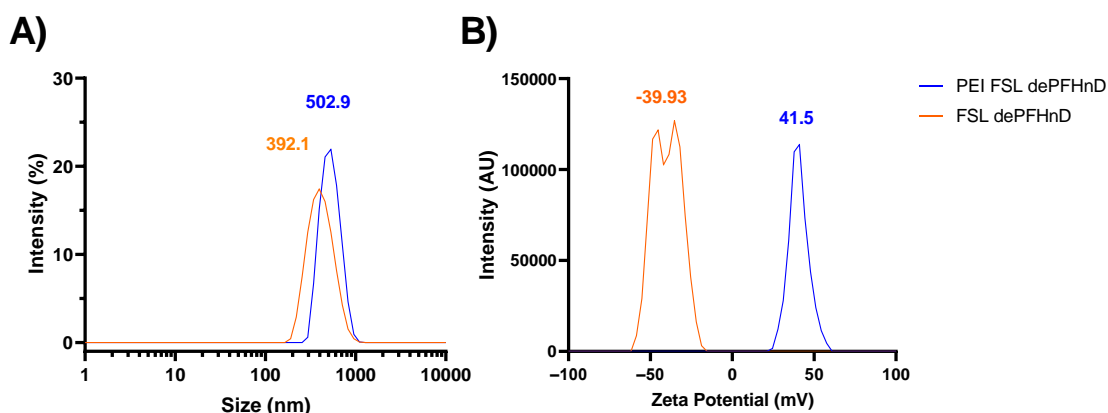


**Figure 40 – A) The averaged DLS size measurement (n = 3) of the FSL dePFHnD with Cy3 without and with a PEI coating. The z-average size of the dePFHnD was found to be 392.1. After coating with PEI, the size increased modestly to 502.9. B) Representative zeta potential measurements of the FSL dePFHnD with Cy3 with and without a PEI coating. The average zeta potential over three measurements for the uncoated FSL dePFHnD was -39.93 and 41.5 for the coated FSL dePFHnD.**

These cationic dePFHnD were incubated with HeLa cells for 4 hours to allow for endocytosis. The HeLa cells were stained with CellTracker blue CMHC dye to allow for visualization of the cell body and the cells were imaged via confocal microscopy. The dePFHnDs were uptaken within the endosome within the cells and there was good co-localization of cy3 and calcein fluorescence (Figure 41). However, as the resolution of confocal microscopy is not enough to distinguish between the different layers of the dePFHnD, co-localization of signal suggests that the particles are capable of encapsulating

both dyes. This result does suggest that these particles could be engineered to selectively enter within the endosome of certain cell types and be utilized to deliver a cocktail of drugs.

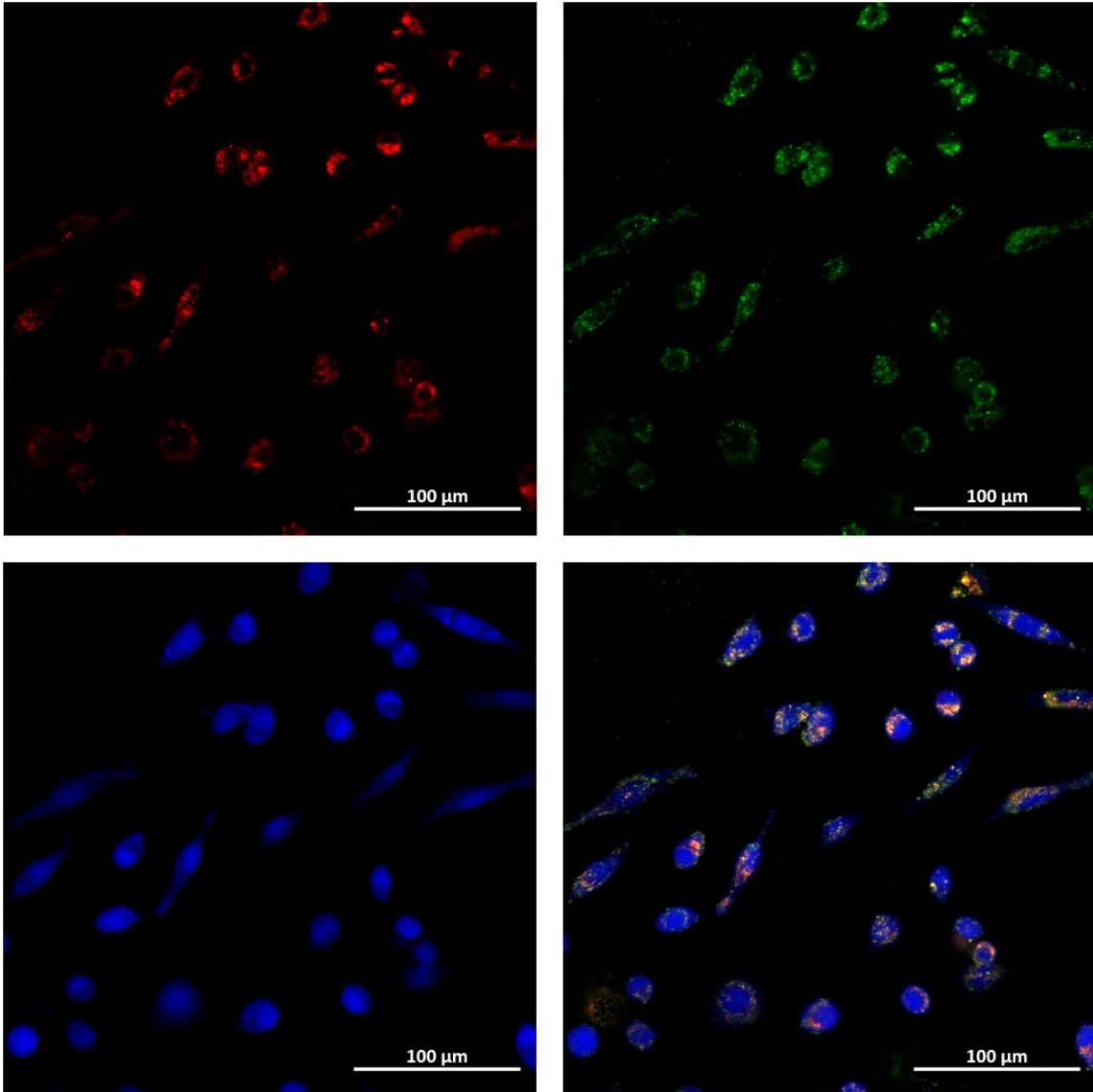


**Figure 41 – Confocal images of PEI coated FSL dePFHnDs loaded with calcein and cy3 that were incubated with HeLa cells, which are stained with Celltracker blue. The images show the hydrophobic cy3 (top left), hydrophilic calcein (top right), celltracker blue (bottom left), and a merged image (bottom right). The scale bars are 100 μm.**

## REFERENCES

- (1) Bushberg, J. T.; Boone, J. M.; Seibert, J. A.; Jr., E. M. L. *The Essential Physics of Medical Imaging*, 3rd ed.; Lippincott Williams & Wilkins, 2011.
- (2) Beard, P. Biomedical Photoacoustic Imaging. *Interface Focus*. **2011**, *1* (4), 602–631. <https://doi.org/10.1098/rsfs.2011.0028>.
- (3) de la Zerda, A. Photoacoustic Imaging: Development of Imaging Systems and Molecular Agents. In *Engineering in Translational Medicine*; Cai, W., Ed.; Springer London: London, 2014; pp 799–833. [https://doi.org/10.1007/978-1-4471-4372-7\\_29](https://doi.org/10.1007/978-1-4471-4372-7_29).
- (4) Smith, A. M.; Mancini, M. C.; Nie, S. Second Window for in Vivo Imaging. *Nature Nanotech* **2009**, *4* (11), 710–711. <https://doi.org/10.1038/nnano.2009.326>.
- (5) Luke, G. P.; Emelianov, S. Y. Label-Free Detection of Lymph Node Metastases with US- Guided Functional Photoacoustic Imaging. **2015**, *000* (0).
- (6) Luke, G. P.; Yeager, D.; Emelianov, S. Y. Biomedical Applications of Photoacoustic Imaging with Exogenous Contrast Agents. *Ann Biomed Eng* **2012**, *40* (2), 422–437. <https://doi.org/10.1007/s10439-011-0449-4>.
- (7) Albrecht, T.; Blomley, M. J. K.; Burns, P. N.; Wilson, S.; Harvey, C. J.; Leen, E.; Claudon, M.; Calliada, F.; Correas, J.-M.; LaFortune, M.; Campani, R.; Hoffmann, C. W.; Cosgrove, D. O.; LeFevre, F. Improved Detection of Hepatic Metastases with Pulse-Inversion US during the Liver-Specific Phase of SHU 508A: Multicenter Study. *Radiology* **2003**, *227* (2), 361–370. <https://doi.org/10.1148/radiol.2272011833>.
- (8) Leen, E.; Ceccotti, P.; Moug, S. J.; Glen, P.; MacQuarrie, J.; Angerson, W. J.; Albrecht, T.; Hohmann, J.; Oldenburg, A.; Ritz, J. P.; Horgan, P. G. Potential Value of Contrast-Enhanced Intraoperative Ultrasonography During Partial Hepatectomy for Metastases: An Essential Investigation Before Resection? *Annals of Surgery* **2006**, *243* (2), 236–240. <https://doi.org/10.1097/01.sla.0000197708.77063.07>.
- (9) Blomley, M.; Albrecht, T.; Cosgrove, D.; Jayaram, V.; Butler-Barnes, J.; Eckersley, R.; Lampeter, E. F.; McCann, S. R.; Kolb, H. Stimulated Acoustic Emission in Liver Parenchyma with Levovist.
- (10) Lee, H.; Kim, H.; Han, H.; Lee, M.; Lee, S.; Yoo, H.; Chang, J. H.; Kim, H. Microbubbles Used for Contrast Enhanced Ultrasound and Theragnosis: A Review of Principles to Applications. *Biomed. Eng. Lett.* **2017**, *7* (2), 59–69. <https://doi.org/10.1007/s13534-017-0016-5>.

- (11) Martin, K. H.; Dayton, P. A. Current Status and Prospects for Microbubbles in Ultrasound Theranostics: Current Status and Prospects for Microbubbles. *WIREs Nanomed Nanobiotechnol* **2013**, *5* (4), 329–345. <https://doi.org/10.1002/wnan.1219>.
- (12) Karamanou, M.; Papaioannou, T.; Stefanadis, C.; Androutsos, G. Genesis of Ultrasonic Microbubbles: A Quick Historical Overview. *CPD* **2012**, *18* (15), 2115–2117. <https://doi.org/10.2174/138161212800099937>.
- (13) WIBLE, J. J.; WOJDYLA, J.; BUGAJ, J.; BRANDENBURGER, G. Effects of Inhaled Gases on the Ultrasound Contrast Produced by Microspheres Containing Air or Perfluoropropane in Anesthetized Dogs. *Investigative Radiology* **1998**, *33* (12).
- (14) Ferrara, K.; Pollard, R.; Borden, M. Ultrasound Microbubble Contrast Agents: Fundamentals and Application to Gene and Drug Delivery. *Annu. Rev. Biomed. Eng.* **2007**, *9* (1), 415–447. <https://doi.org/10.1146/annurev.bioeng.8.061505.095852>.
- (15) Van Wamel, A.; Kooiman, K.; Hartevelde, M.; Emmer, M.; Ten Cate, F. J.; Versluis, M.; De Jong, N. Vibrating Microbubbles Poking Individual Cells: Drug Transfer into Cells via Sonoporation. *Journal of Controlled Release* **2006**, *112* (2), 149–155. <https://doi.org/10.1016/j.jconrel.2006.02.007>.
- (16) Rich, J.; Tian, Z.; Huang, T. J. Sonoporation: Past, Present, and Future. *Adv Materials Technologies* **2022**, *7* (1), 2100885. <https://doi.org/10.1002/admt.202100885>.
- (17) Song, K.-H.; Harvey, B. K.; Borden, M. A. State-of-the-Art of Microbubble-Assisted Blood-Brain Barrier Disruption. *Theranostics* **2018**, *8* (16), 4393–4408. <https://doi.org/10.7150/thno.26869>.
- (18) Sheeran, P. S.; Luo, S. H.; Mullin, L. B.; Matsunaga, T. O.; Dayton, P. A. Design of Ultrasonically-Activatable Nanoparticles Using Low Boiling Point Perfluorocarbons. *Biomaterials* **2012**, *33* (11), 3262–3269. <https://doi.org/10.1016/j.biomaterials.2012.01.021>.
- (19) Lee, S.; Kim, D. H.; Needham, D. Equilibrium and Dynamic Interfacial Tension Measurements at Microscopic Interfaces Using a Micropipet Technique. 2. Dynamics of Phospholipid Monolayer Formation and Equilibrium Tensions at the Water–Air Interface. *Langmuir* **2001**, *17* (18), 5544–5550. <https://doi.org/10.1021/la0103261>.
- (20) Mountford, P. A.; Borden, M. A. On the Thermodynamics and Kinetics of Superheated Fluorocarbon Phase-Change Agents. *Advances in Colloid and Interface Science* **2016**, *237*, 15–27. <https://doi.org/10.1016/j.cis.2016.08.007>.
- (21) Chen, Q.; Yu, J.; Kim, K. Review: Optically-Triggered Phase-Transition Droplets for Photoacoustic Imaging. *Biomed. Eng. Lett.* **2018**, *8* (2), 223–229. <https://doi.org/10.1007/s13534-018-0069-0>.
- (22) Asami, R.; Kawabata, K. Repeatable Vaporization of Optically Vaporizable Perfluorocarbon Droplets for Photoacoustic Contrast Enhanced Imaging. In *2012*

- IEEE International Ultrasonics Symposium*; IEEE: Dresden, Germany, 2012; pp 1200–1203. <https://doi.org/10.1109/ULTSYM.2012.0299>.
- (23) Luke, G. P.; Hannah, A. S.; Emelianov, S. Y. Super-Resolution Ultrasound Imaging in Vivo with Transient Laser-Activated Nanodroplets. *Nano Letters* **2016**, *16* (4), 2556–2559. <https://doi.org/10.1021/acs.nanolett.6b00108>.
- (24) Hannah, A. S.; Luke, G. P.; Emelianov, S. Y. Blinking Phase-Change Nanocapsules Enable Background-Free Ultrasound Imaging. *Theranostics* **2016**, *6* (11), 1866–1876. <https://doi.org/10.7150/thno.14961>.
- (25) Santiesteban, D. Y.; Hallam, K. A.; Yarmoska, S. K.; Emelianov, S. Y. Color-Coded Perfluorocarbon Nanodroplets for Multiplexed Ultrasound and Photoacoustic Imaging. *Nano Research* **2019**, *12* (4), 741–747. <https://doi.org/10.1007/s12274-019-2279-x>.
- (26) Zhu, Y. I.; Yoon, H.; Zhao, A. X.; Emelianov, S. Y. Leveraging the Imaging Transmit Pulse to Manipulate Phase-Change Nanodroplets for Contrast-Enhanced Ultrasound. *IEEE Trans. Ultrason., Ferroelect., Freq. Contr.* **2019**, *66* (4), 692–700. <https://doi.org/10.1109/TUFFC.2019.2895248>.
- (27) Spatarelu, C.-P.; Van Namen, A.; Luke, G. P. Optically Activatable Double-Drug-Loaded Perfluorocarbon Nanodroplets for On-Demand Image-Guided Drug Delivery. *ACS Appl. Nano Mater.* **2021**, *4* (8), 8026–8038. <https://doi.org/10.1021/acsnm.1c01303>.
- (28) Zhao, A. X.; Zhu, Y. I.; Chung, E.; Lee, J.; Morais, S.; Yoon, H.; Emelianov, S. Factors Influencing the Repeated Transient Optical Droplet Vaporization Threshold and Lifetimes of Phase Change, Perfluorocarbon Nanodroplets. *Nanomaterials* **2023**, *13* (15), 2238. <https://doi.org/10.3390/nano13152238>.
- (29) Kripfgans, O. D.; Fowlkes, J. B.; Miller, D. L.; Eldevik, O. P.; Carson, P. L. Acoustic Droplet Vaporization for Therapeutic and Diagnostic Applications. *Ultrasound in Medicine & Biology* **2000**, *26* (7), 1177–1189. [https://doi.org/10.1016/S0301-5629\(00\)00262-3](https://doi.org/10.1016/S0301-5629(00)00262-3).
- (30) Wilson, K.; Homan, K.; Emelianov, S. Biomedical Photoacoustics beyond Thermal Expansion Using Triggered Nanodroplet Vaporization for Contrast-Enhanced Imaging. *Nat Commun* **2012**, *3* (1), 618. <https://doi.org/10.1038/ncomms1627>.
- (31) Dove, J. D.; Mountford, P. A.; Murray, T. W.; Borden, M. A. Engineering Optically Triggered Droplets for Photoacoustic Imaging and Therapy. *Biomedical Optics Express* **2014**, *5* (12), 4417. <https://doi.org/10.1364/BOE.5.004417>.
- (32) Strohm, E.; Rui, M.; Gorelikov, I.; Matsuura, N.; Kolios, M. Vaporization of Perfluorocarbon Droplets Using Optical Irradiation. *Biomedical Optics Express* **2011**, *2* (6), 1432. <https://doi.org/10.1364/BOE.2.001432>.

- (33) Rapoport, N. Phase-Shift, Stimuli-Responsive Perfluorocarbon Nanodroplets for Drug Delivery to Cancer: Phase-Shift Perfluorocarbon Nanoemulsions. *WIREs Nanomed Nanobiotechnol* **2012**, *4* (5), 492–510. <https://doi.org/10.1002/wnan.1176>.
- (34) Hallam, K. A.; Donnelly, E. M.; Karpouk, A. B.; Hartman, R. K.; Emelianov, S. Y. Laser-Activated Perfluorocarbon Nanodroplets: A New Tool for Blood Brain Barrier Opening. *Biomedical Optics Express* **2018**, *9* (9), 4527. <https://doi.org/10.1364/BOE.9.004527>.
- (35) Chen, C. C.; Sheeran, P. S.; Wu, S.-Y.; Olumolade, O. O.; Dayton, P. A.; Konofagou, E. E. Targeted Drug Delivery with Focused Ultrasound-Induced Blood-Brain Barrier Opening Using Acoustically-Activated Nanodroplets. *Journal of Controlled Release* **2013**, *172* (3), 795–804. <https://doi.org/10.1016/j.jconrel.2013.09.025>.
- (36) Wu, S.-Y.; Fix, S. M.; Arena, C. B.; Chen, C. C.; Zheng, W.; Olumolade, O. O.; Papadopoulou, V.; Novell, A.; Dayton, P. A.; Konofagou, E. E. Focused Ultrasound-Facilitated Brain Drug Delivery Using Optimized Nanodroplets: Vaporization Efficiency Dictates Large Molecular Delivery. *Phys. Med. Biol.* **2018**, *63* (3), 035002. <https://doi.org/10.1088/1361-6560/aaa30d>.
- (37) Liu, W.-W.; Liu, S.-W.; Liou, Y.-R.; Wu, Y.-H.; Yang, Y.-C.; Wang, C.-R. C.; Li, P.-C. Nanodroplet-Vaporization-Assisted Sonoporation for Highly Effective Delivery of Photothermal Treatment. *Sci Rep* **2016**, *6* (1), 24753. <https://doi.org/10.1038/srep24753>.
- (38) Aliabouzar, M.; Kripfgans, O. D.; Brian Fowlkes, J.; Fabiilli, M. L. Bubble Nucleation and Dynamics in Acoustic Droplet Vaporization: A Review of Concepts, Applications, and New Directions. *Zeitschrift für Medizinische Physik* **2023**, S0939388923000041. <https://doi.org/10.1016/j.zemedi.2023.01.004>.
- (39) Wu, Q.; Mannaris, C.; May, J. P.; Bau, L.; Polydorou, A.; Ferri, S.; Carugo, D.; Evans, N. D.; Stride, E. Investigation of the Acoustic Vaporization Threshold of Lipid-Coated Perfluorobutane Nanodroplets Using Both High-Speed Optical Imaging and Acoustic Methods. *Ultrasound in Medicine & Biology* **2021**, *47* (7), 1826–1843. <https://doi.org/10.1016/j.ultrasmedbio.2021.02.019>.
- (40) Fabiilli, M. L.; Haworth, K. J.; Fakhri, N. H.; Kripfgans, O. D.; Carson, P. L.; Fowlkes, J. B. The Role of Inertial Cavitation in Acoustic Droplet Vaporization. *IEEE Trans. Ultrason., Ferroelect., Freq. Contr.* **2009**, *56* (5), 1006–1017. <https://doi.org/10.1109/TUFFC.2009.1132>.
- (41) Porter, T.; Zhang, P. Temperature and Size-dependence of the Vaporization Threshold of Phase-shift Emulsions. *The Journal of the Acoustical Society of America* **2008**, *123* (5), 2997–2997. <https://doi.org/10.1121/1.2932552>.
- (42) Yu, J.; Chen, X.; Villanueva, F. S.; Kim, K. Vaporization and Recondensation Dynamics of Indocyanine Green-Loaded Perfluoropentane Droplets Irradiated by a

- Short Pulse Laser. *Applied Physics Letters* **2016**, *109* (24), 243701. <https://doi.org/10.1063/1.4972184>.
- (43) Lajoinie, G.; Gelderblom, E.; Chlon, C.; Böhmer, M.; Steenbergen, W.; de Jong, N.; Manohar, S.; Versluis, M. Ultrafast Vapourization Dynamics of Laser-Activated Polymeric Microcapsules. *Nat Commun* **2014**, *5* (1), 3671. <https://doi.org/10.1038/ncomms4671>.
- (44) Si, T.; Li, G.; Wu, Q.; Zhu, Z.; Luo, X.; Xu, R. X. Optical Droplet Vaporization of Nanoparticle-Loaded Stimuli-Responsive Microbubbles. *Appl. Phys. Lett.* **2016**, *108* (11), 111109. <https://doi.org/10.1063/1.4944539>.
- (45) Yarmoska, S. K.; Yoon, H.; Emelianov, S. Y. Lipid Shell Composition Plays a Critical Role in the Stable Size Reduction of Perfluorocarbon Nanodroplets. *Ultrasound in Medicine & Biology* **2019**, *45* (6), 1489–1499. <https://doi.org/10.1016/j.ultrasmedbio.2019.02.009>.
- (46) Hannah, A.; Luke, G.; Wilson, K.; Homan, K.; Emelianov, S. Indocyanine Green-Loaded Photoacoustic Nanodroplets: Dual Contrast Nanoconstructs for Enhanced Photoacoustic and Ultrasound Imaging. *ACS Nano* **2014**, *8* (1), 250–259. <https://doi.org/10.1021/nn403527r>.
- (47) Yoon, H.; Hallam, K. A.; Yoon, C.; Emelianov, S. Y. Super-Resolution Imaging With Ultrafast Ultrasound Imaging of Optically Triggered Perfluorohexane Nanodroplets. *IEEE Transactions on Ultrasonics, Ferroelectrics, and Frequency Control* **2018**, *65* (12), 2277–2285. <https://doi.org/10.1109/TUFFC.2018.2829740>.
- (48) Boudou, T.; Ohayon, J.; Picart, C.; Pettigrew, R. I.; Tracqui, P. Nonlinear Elastic Properties of Polyacrylamide Gels: Implications for Quantification of Cellular Forces. *Biorheology* **2009**, *46* (3), 191–205. <https://doi.org/10.3233/BIR-2009-0540>.
- (49) Zhang, X.; Greenleaf, J. F. Estimation of Tissue's Elasticity with Surface Wave Speed. *J. Acoust. Soc. Am.* **2007**, *122* (5), 2522. <https://doi.org/10.1121/1.2785045>.
- (50) Loupas, T.; Powers, J. T.; Gill, R. W. An Axial Velocity Estimator for Ultrasound Blood Flow Imaging, Based on a Full Evaluation of the Doppler Equation by Means of a Two-Dimensional Autocorrelation Approach. *IEEE Trans. Ultrason., Ferroelect., Freq. Contr.* **1995**, *42* (4), 672–688. <https://doi.org/10.1109/58.393110>.
- (51) Namen, A. V.; Jandhyala, S.; Jordan, T.; Luke, G. P. Repeated Acoustic Vaporization of Perfluorohexane Nanodroplets for Contrast-Enhanced Ultrasound Imaging. *IEEE Trans. Ultrason., Ferroelect., Freq. Contr.* **2021**, *68* (12), 3497–3506. <https://doi.org/10.1109/TUFFC.2021.3093828>.
- (52) Li, D. S.; Yoon, S. J.; Pelivanov, I.; Frenz, M.; O'Donnell, M.; Pozzo, L. D. Polypyrrole-Coated Perfluorocarbon Nanoemulsions as a Sono-Photoacoustic Contrast Agent. *Nano Letters* **2017**, *17* (10), 6184–6194. <https://doi.org/10.1021/acs.nanolett.7b02845>.

- (53) Astafyeva, K.; Somaglino, L.; Desgranges, S.; Berti, R.; Patinote, C.; Langevin, D.; Lazeyras, F.; Salomir, R.; Polidori, A.; Contino-Pépin, C.; Urbach, W.; Taulier, N. Perfluorocarbon Nanodroplets Stabilized by Fluorinated Surfactants: Characterization and Potentiality as Theranostic Agents. *J. Mater. Chem. B* **2015**, *3* (14), 2892–2907. <https://doi.org/10.1039/C4TB01578A>.
- (54) Fernandes, D. A.; Fernandes, D. D.; Li, Y.; Wang, Y.; Zhang, Z.; Rousseau, D.; Gradinaru, C. C.; Kolios, M. C. Synthesis of Stable Multifunctional Perfluorocarbon Nanoemulsions for Cancer Therapy and Imaging. *Langmuir* **2016**, *32* (42), 10870–10880. <https://doi.org/10.1021/acs.langmuir.6b01867>.
- (55) Rapoport, N.; Christensen, D. A.; Kennedy, A. M.; Nam, K.-H. Cavitation Properties of Block Copolymer Stabilized Phase-Shift Nanoemulsions Used as Drug Carriers. *Ultrasound in Medicine & Biology* **2010**, *36* (3), 419–429. <https://doi.org/10.1016/j.ultrasmedbio.2009.11.009>.
- (56) Reznik, N.; Seo, M.; Williams, R.; Bolewska-Pedyczak, E.; Lee, M.; Matsuura, N.; Garipey, J.; Foster, F. S.; Burns, P. N. Optical Studies of Vaporization and Stability of Fluorescently Labelled Perfluorocarbon Droplets. *Phys. Med. Biol.* **2012**, *57* (21), 7205–7217. <https://doi.org/10.1088/0031-9155/57/21/7205>.
- (57) Silwal, A.; Upadhyay, A.; Shakya, G.; Inzunza-Ibarra, M.; Murray, T.; Ding, X.; Borden, M. A. Photoacoustic Vaporization of Endoskeletal Droplets Loaded with Zinc Naphthalocyanine. *Langmuir* **2023**, *39* (1), 168–176. <https://doi.org/10.1021/acs.langmuir.2c02320>.
- (58) Chattaraj, R.; Goldscheitter, G. M.; Yildirim, A.; Goodwin, A. P. Phase Behavior of Mixed Lipid Monolayers on Perfluorocarbon Nanoemulsions and Its Effect on Acoustic Contrast. *RSC Advances* **2016**, *6* (112), 111318–111325. <https://doi.org/10.1039/C6RA20328K>.
- (59) Zhang, Z.; Taylor, M.; Kaval, N.; Park, Y. C. Phase-Transition Temperature of Gold-Nanorod-Coated Nanodroplets to Microbubbles by Pulsed Laser. *J. Phys. Chem. A* **2019**, *123* (23), 4844–4852. <https://doi.org/10.1021/acs.jpca.9b02566>.
- (60) Quay, S. Phase Shift Colloids As Ultrasound Contrast Agents. 5707606, January 13, 1984. <https://patents.google.com/patent/US5707606A/en> (accessed 2022-05-16).
- (61) Kandadai, M. A.; Mohan, P.; Lin, G.; Butterfield, A.; Skliar, M.; Magda, J. J. Comparison of Surfactants Used to Prepare Aqueous Perfluoropentane Emulsions for Pharmaceutical Applications. *Langmuir* **2010**, *26* (7), 4655–4660. <https://doi.org/10.1021/la100307r>.
- (62) Sheeran, P. S.; Luois, S.; Dayton, P. A.; Matsunaga, T. O. Formulation and Acoustic Studies of a New Phase-Shift Agent for Diagnostic and Therapeutic Ultrasound. *Langmuir* **2011**, *27* (17), 10412–10420. <https://doi.org/10.1021/la2013705>.

- (63) Dunlap, R. D.; Murphy, C. J.; Bedford, R. G. Some Physical Properties of Perfluoro-n-Hexane. *J. Am. Chem. Soc.* **1958**, *80* (1), 83–85. <https://doi.org/10.1021/ja01534a023>.
- (64) Mountford, P. A.; Thomas, A. N.; Borden, M. A. Thermal Activation of Superheated Lipid-Coated Perfluorocarbon Drops. *Langmuir* **2015**, *31* (16), 4627–4634. <https://doi.org/10.1021/acs.langmuir.5b00399>.
- (65) Huang, Y.; Vezeridis, A. M.; Wang, J.; Wang, Z.; Thompson, M.; Mattrey, R. F.; Gianneschi, N. C. Polymer-Stabilized Perfluorobutane Nanodroplets for Ultrasound Imaging Agents. *J. Am. Chem. Soc.* **2017**, *139* (1), 15–18. <https://doi.org/10.1021/jacs.6b08800>.
- (66) Grinstaff, M. W.; Suslick, K. S. Air-Filled Proteinaceous Microbubbles: Synthesis of an Echo-Contrast Agent. *Proc. Natl. Acad. Sci. U.S.A.* **1991**, *88* (17), 7708–7710. <https://doi.org/10.1073/pnas.88.17.7708>.
- (67) Pollice, R.; Chen, P. Origin of the Immiscibility of Alkanes and Perfluoroalkanes. *J. Am. Chem. Soc.* **2019**, *141* (8), 3489–3506. <https://doi.org/10.1021/jacs.8b10745>.
- (68) Dayton, P. A.; Morgan, K. E.; Klibanov, A. L.; Brandenburger, G. H.; Ferrara, K. W. Optical and Acoustical Observations of the Effects of Ultrasound on Contrast Agents. *IEEE Trans. Ultrason., Ferroelect., Freq. Contr.* **1999**, *46* (1), 220–232. <https://doi.org/10.1109/58.741536>.
- (69) Helfield, B.; Black, J. J.; Qin, B.; Pacella, J.; Chen, X.; Villanueva, F. S. Fluid Viscosity Affects the Fragmentation and Inertial Cavitation Threshold of Lipid-Encapsulated Microbubbles. *Ultrasound in Medicine & Biology* **2016**, *42* (3), 782–794. <https://doi.org/10.1016/j.ultrasmedbio.2015.10.023>.
- (70) Reznik, N.; Shpak, O.; Gelderblom, E. C.; Williams, R.; De Jong, N.; Versluis, M.; Burns, P. N. The Efficiency and Stability of Bubble Formation by Acoustic Vaporization of Submicron Perfluorocarbon Droplets. *Ultrasonics* **2013**, *53* (7), 1368–1376. <https://doi.org/10.1016/j.ultras.2013.04.005>.
- (71) Butcher, D. T.; Alliston, T.; Weaver, V. M. A Tense Situation: Forcing Tumour Progression. *Nat Rev Cancer* **2009**, *9* (2), 108–122. <https://doi.org/10.1038/nrc2544>.
- (72) Jandhyala, S.; Van Namen, A.; Spatarelu, C.-P.; Luke, G. P. EGFR-Targeted Perfluorohexane Nanodroplets for Molecular Ultrasound Imaging. *Nanomaterials* **2022**, *12* (13), 2251. <https://doi.org/10.3390/nano12132251>.
- (73) Chudal, L.; de Gracia Lux, C.; Lux, J.; Mattrey, R. Acoustic Vaporization of Internalized Superheated Perfluorocarbon Nanodroplets for Imaging and Macrophage Function Modulation. *The Journal of the Acoustical Society of America* **2021**, *150* (4\_Supplement), A53–A53. <https://doi.org/10.1121/10.0007601>.

- (74) Chudal, L.; de Gracia Lux, C.; Lux, J.; Mattrey, R. In Vivo Ultrasound Imaging of Macrophages Using Acoustic Vaporization of Internalized Superheated Nanodroplets. *The Journal of the Acoustical Society of America* **2022**, *152* (4), A79–A79. <https://doi.org/10.1121/10.0015608>.
- (75) Xu, Z.; Liu, H.; Tian, H.; Yan, F. Real-Time Imaging Tracking of Engineered Macrophages as Ultrasound-Triggered Cell Bombs for Cancer Treatment. *Adv. Funct. Mater.* **2020**, *30* (14), 1910304. <https://doi.org/10.1002/adfm.201910304>.
- (76) Pradhan, S.; Keller, K. A.; Sperduto, J. L.; Slater, J. H. Fundamentals of Laser-Based Hydrogel Degradation and Applications in Cell and Tissue Engineering. *Adv. Healthcare Mater.* **2017**, *6* (24), 1700681. <https://doi.org/10.1002/adhm.201700681>.
- (77) Aliabouzar, M.; Kumar, K. N.; Sarkar, K. Effects of Droplet Size and Perfluorocarbon Boiling Point on the Frequency Dependence of Acoustic Vaporization Threshold. *The Journal of the Acoustical Society of America* **2019**, *145* (2), 1105–1116. <https://doi.org/10.1121/1.5091781>.
- (78) Wei, C.; Xia, J.; Lombardo, M.; Perez, C.; Arnal, B.; Larson-Smith, K.; Pelivanov, I.; Matula, T.; Pozzo, L.; O'Donnell, M. Laser-Induced Cavitation in Nanoemulsion with Gold Nanospheres for Blood Clot Disruption: In Vitro Results. *Opt. Lett.* **2014**, *39* (9), 2599. <https://doi.org/10.1364/OL.39.002599>.
- (79) Liu, W.; Ko, H.; Li, P. Sonoporation Based on Repeated Vaporization of Gold Nanodroplets. *Medical Physics* **2022**, *49* (4), 2761–2773. <https://doi.org/10.1002/mp.15544>.
- (80) Liu, W.-W.; Huang, S.-H.; Li, P.-C. Synchronized Optical and Acoustic Droplet Vaporization for Effective Sonoporation. *Pharmaceutics* **2019**, *11* (6), 279. <https://doi.org/10.3390/pharmaceutics11060279>.
- (81) Zhang, J.-Z.; K. Sagggar, J.; Zhou, Z.-L.; Hu, B. Different Effects of Sonoporation on Cell Morphology and Viability. *Bosn J of Basic Med Sci* **2012**, *12* (2), 64. <https://doi.org/10.17305/bjbms.2012.2497>.
- (82) Chakravarty, P.; Qian, W.; El-Sayed, M. A.; Prausnitz, M. R. Delivery of Molecules into Cells Using Carbon Nanoparticles Activated by Femtosecond Laser Pulses. *Nature Nanotech* **2010**, *5* (8), 607–611. <https://doi.org/10.1038/nnano.2010.126>.
- (83) Kumar, S.; Chong, C.; Voorhees, T.; Thadhani, N. N.; Prausnitz, M. R. Relationship between Bio-Effects and Energy Transduction during Nanoparticle-Mediated Photoporation. *Journal of Applied Physics* **2020**, *128* (17), 173101. <https://doi.org/10.1063/5.0021834>.
- (84) Adan, M. N.; Fabiilli, M. L.; Wilson, C. G.; Kripfgans, O. D. Acoustic Droplet Vaporization-Induced Cellular Sonoporation. In *2012 IEEE International Ultrasonics Symposium*; IEEE: Dresden, Germany, 2012; pp 448–450. <https://doi.org/10.1109/ULTSYM.2012.0111>.

- (85) Xu, J.; Chen, Y.; Deng, L.; Liu, J.; Cao, Y.; Li, P.; Ran, H.; Zheng, Y.; Wang, Z. Microwave-Activated Nanodroplet Vaporization for Highly Efficient Tumor Ablation with Real-Time Monitoring Performance. *Biomaterials* **2016**, *106*, 264–275. <https://doi.org/10.1016/j.biomaterials.2016.08.034>.
- (86) Wilhelm, S.; Tavares, A. J.; Dai, Q.; Ohta, S.; Audet, J.; Dvorak, H. F.; Chan, W. C. W. Analysis of Nanoparticle Delivery to Tumours. *Nat Rev Mater* **2016**, *1* (5), 16014. <https://doi.org/10.1038/natrevmats.2016.14>.
- (87) Mura, S.; Nicolas, J.; Couvreur, P. Stimuli-Responsive Nanocarriers for Drug Delivery. *Nature Mater* **2013**, *12* (11), 991–1003. <https://doi.org/10.1038/nmat3776>.
- (88) Kaneda, M. M.; Caruthers, S.; Lanza, G. M.; Wickline, S. A. Perfluorocarbon Nanoemulsions for Quantitative Molecular Imaging and Targeted Therapeutics. *Ann Biomed Eng* **2009**, *37* (10), 1922–1933. <https://doi.org/10.1007/s10439-009-9643-z>.
- (89) Fabiilli, M. L.; Haworth, K. J.; Sebastian, I. E.; Kripfgans, O. D.; Carson, P. L.; Fowlkes, J. B. Delivery of Chlorambucil Using an Acoustically-Triggered Perfluoropentane Emulsion. *Ultrasound in Medicine & Biology* **2010**, *36* (8), 1364–1375. <https://doi.org/10.1016/j.ultrasmedbio.2010.04.019>.
- (90) Javadi, M.; Pitt, W. G.; Belnap, D. M.; Tsosie, N. H.; Hartley, J. M. Encapsulating Nanoemulsions Inside eLiposomes for Ultrasonic Drug Delivery. *Langmuir* **2012**, *28* (41), 14720–14729. <https://doi.org/10.1021/la303464v>.
- (91) Javadi, M.; Pitt, W. G.; Tracy, C. M.; Barrow, J. R.; Willardson, B. M.; Hartley, J. M.; Tsosie, N. H. Ultrasonic Gene and Drug Delivery Using eLiposomes. *Journal of Controlled Release* **2013**, *167* (1), 92–100. <https://doi.org/10.1016/j.jconrel.2013.01.009>.
- (92) Fabiilli, M. L.; Lee, J. A.; Kripfgans, O. D.; Carson, P. L.; Fowlkes, J. B. Delivery of Water-Soluble Drugs Using Acoustically Triggered Perfluorocarbon Double Emulsions. *Pharm Res* **2010**, *27* (12), 2753–2765. <https://doi.org/10.1007/s11095-010-0277-5>.
- (93) Duncanson, W. J.; Arriaga, L. R.; Ung, W. L.; Kopechek, J. A.; Porter, T. M.; Weitz, D. A. Microfluidic Fabrication of Perfluorohexane-Shelled Double Emulsions for Controlled Loading and Acoustic-Triggered Release of Hydrophilic Agents. *Langmuir* **2014**, *30* (46), 13765–13770. <https://doi.org/10.1021/la502473w>.
- (94) Chen, Y.-S.; Zhao, Y.; Beinart, C.; Zlitni, A.; Hsu, E.-C.; Chen, D.-H.; Achterberg, F.; Wang, H.; Stoyanova, T.; Dionne, J.; Gambhir, S. S. Ultra-High-Frequency Radio-Frequency Acoustic Molecular Imaging with Saline Nanodroplets in Living Subjects. *Nat. Nanotechnol.* **2021**, *16* (6), 717–724. <https://doi.org/10.1038/s41565-021-00869-5>.

- (95) G. Moloughney, J.; Weisleder, N. Poloxamer 188 (P188) as a Membrane Resealing Reagent in Biomedical Applications. *BIOT* **2012**, *6* (3), 200–211. <https://doi.org/10.2174/1872208311206030200>.
- (96) Day, R. A.; Estabrook, D. A.; Wu, C.; Chapman, J. O.; Togle, A. J.; Sletten, E. M. Systematic Study of Perfluorocarbon Nanoemulsions Stabilized by Polymer Amphiphiles. *ACS Appl. Mater. Interfaces* **2020**, *12* (35), 38887–38898. <https://doi.org/10.1021/acsami.0c07206>.
- (97) Heitmeier, M. R.; Scarim, A. L.; Corbett, J. A. Double-Stranded RNA-Induced Inducible Nitric-Oxide Synthase Expression and Interleukin-1 Release by Murine Macrophages Requires NF- $\kappa$ B Activation. *Journal of Biological Chemistry* **1998**, *273* (24), 15301–15307. <https://doi.org/10.1074/jbc.273.24.15301>.
- (98) Deininger, P. L. Random Subcloning of Sonicated DNA: Application to Shotgun DNA Sequence Analysis. *Analytical Biochemistry* **1983**, *129* (1), 216–223. [https://doi.org/10.1016/0003-2697\(83\)90072-6](https://doi.org/10.1016/0003-2697(83)90072-6).
- (99) Santiesteban, D. Y.; Hallam, K. A.; Yarmoska, S. K.; Emelianov, S. Y. Color-Coded Perfluorocarbon Nanodroplets for Multiplexed Ultrasound and Photoacoustic Imaging. *Nano Res.* **2019**, *12* (4), 741–747. <https://doi.org/10.1007/s12274-019-2279-x>.
- (100) Sheeran, P. S.; Matsuura, N.; Borden, M. A.; Williams, R.; Matsunaga, T. O.; Burns, P. N.; Dayton, P. A. Methods of Generating Submicrometer Phase-Shift Perfluorocarbon Droplets for Applications in Medical Ultrasonography. *IEEE Trans. Ultrason., Ferroelect., Freq. Contr.* **2017**, *64* (1), 252–263. <https://doi.org/10.1109/TUFFC.2016.2619685>.
- (101) Aliabouzar, M.; Lu, X.; Kripfgans, O. D.; Fowlkes, J. B.; Fabiilli, M. L. Acoustic Droplet Vaporization in Acoustically Responsive Scaffolds: Effects of Frequency of Excitation, Volume Fraction and Threshold Determination Method. *Ultrasound in Medicine & Biology* **2019**, *45* (12), 3246–3260. <https://doi.org/10.1016/j.ultrasmedbio.2019.08.018>.
- (102) Melich, R.; Bussat, P.; Morici, L.; Vivien, A.; Gaud, E.; Bettinger, T.; Cherkaoui, S. Microfluidic Preparation of Various Perfluorocarbon Nanodroplets: Characterization and Determination of Acoustic Droplet Vaporization (ADV) Threshold. *International Journal of Pharmaceutics* **2020**, *587*, 119651. <https://doi.org/10.1016/j.ijpharm.2020.119651>.
- (103) Ermakov, G. V.; Skripov, V. P. Saturation Line, Critical Parameters, and Attainable Superheating of the Perfluoroparaffins. *Russ. J. Phys. Chem. (Engl. Transl.)* **1967**, *41*, 39–43.
- (104) Mousa, A. H. N. Study of Vapor Pressure and Critical Properties of Perfluoro-n-Hexane. *J. Chem. Eng. Data* **1978**, *23* (2), 133–134.

- (105) Steele, W. V.; Chirico, R. D.; Knipmeyer, S. E.; Nguyen, A. Vapor Pressure, Heat Capacity, and Density along the Saturation Line, Measurements for Dimethyl Isophthalate, Dimethyl Carbonate, 1,3,5-Triethylbenzene, Pentafluorophenol, 4- *Tert*-Butylcatechol,  $\alpha$ -Methylstyrene, and *N*, *N*'-Bis(2-Hydroxyethyl)Ethylenediamine. *Journal of Chemical & Engineering Data* **1997**, *42* (6), 1008–1020. <https://doi.org/10.1021/je970102d>.
- (106) Taranejoo, S.; Liu, J.; Verma, P.; Hourigan, K. A Review of the Developments of Characteristics of PEI Derivatives for Gene Delivery Applications. *J. Appl. Polym. Sci.* **2015**, *132* (25), n/a-n/a. <https://doi.org/10.1002/app.42096>.